DRY DEPOSITION OF OZONE IN THE LOWER FRASER VALLEY, BRITISH COLUMBIA: MEASUREMENTS AND COMPARISON WITH A MODEL

By

MARKUS KELLERHALS

B.Sc., The University of British Columbia, 1988
Dip. Met., The University of British Columbia, 1993

A THESIS SUBMITTED IN PARTIAL FULFILLMENT OF
THE REQUIREMENTS FOR THE DEGREE OF
MASTER OF SCIENCE

in

THE FACULTY OF GRADUATE STUDIES

(Department of Geography)

We accept this thesis as conforming
to the required standard

THE UNIVERSITY OF BRITISH COLUMBIA

March 1996

In presenting this thesis in partial fulfilment of the requirements for an advanced degree at the University of British Columbia, I agree that the Library shall make it freely available for reference and study. I further agree that permission for extensive copying of this thesis for scholarly purposes may be granted by the head of my department or by his or her representatives. It is understood that copying or publication of this thesis for financial gain shall not be allowed without my written permission.

Department of Geography

The University of British Columbia
Vancouver, Canada

Date Mar 21, 1996

ABSTRACT

Surface deposition is an important sink for tropospheric ozone. The rate of ozone deposition may be measured by measuring the downward flux of ozone in the atmospheric surface-layer.

This thesis presents eddy correlation measurements of ozone fluxes, taken on eight days in August, 1994, at a grassland site located in the Lower Fraser Valley of British Columbia. Surface resistances to ozone deposition were calculated from the flux measurements. Much of the variability in measured surface resistances was found to be attributable to variations in ambient light levels and in the degree of moisture stress at the site. Measurements of surface resistance from this site agreed quite well with other measurements of ozone deposition to grassland surfaces.

Measured surface resistances were compared to surface resistances calculated using the Wesely (1989) parameterization (W89) for surface resistance. W89 underestimated surface resistance, particularly in the mid afternoon and early evening. This was attributed to the model's neglect of the effects of water stress on stomatal resistance, as well as to a low value for resistance to ground surface deposition in the model.

The eddy correlation fluxes were compared to ozone fluxes derived using an assumption of cospectral similarity between ozone and heat flux and to ozone fluxes measured using the variance method and the gradient method. The cospectral similarity method worked well and allowed a considerable relaxation of the sampling speed requirements of the eddy correlation method. The variance method produced biased flux measurements due to high frequency noise from the ozone sensor. Flux measurements using the gradient method had a great deal of scatter, due to inaccuracies in the measurement of gradients.

TABLE OF CONTENTS

LIST OF TABLES

LIST OF FIGURES

ACKNOWLEDGMENTS

I would like to thank all those who contributed to the success of this project. Foremost among these is my supervisor Dr. Douw Steyn who provided support, useful suggestions and constructive criticism throughout the project. His support and enthusiasm were a major boost towards the timely completion of this project and helped to make my time in the department an enjoyable and rewarding one

Thanks are due to Dr. Andy Black for loan of the measurement tower as well as helpful advice on instrument configuration. Terry Gillespie also provided helpful advice on the field measurements.

The field research was conducted on the Pitt Meadows airport grounds. I am grateful to airport manager Rick Newton (Transport Canada) for permission to use the area for my research.

I was supported financially through the course of the project by a scholarship from the Atmospheric Environment Service, a research assistantship provided by Dr. Steyn and teaching assistantships provided by the Department of Geography. The project was funded by grants to Dr. Douw Steyn from the Natural Sciences and Engineering Research Council of Canada and the Atmospheric Environment Service of Environment Canada.

Finally, thanks to my friends and fellow graduate students for helping to make my stay in the Department an enjoyable one.

1. INTRODUCTION

1.1 Background

Ozone (O_3) is an allotropic form of oxygen composed of three oxygen atoms. Ozone occurs naturally in the stratosphere, where it is formed from the photolysis of molecular oxygen by solar ultraviolet radiation. In the troposphere, ozone also occurs naturally, though in much smaller concentrations, as a result of in situ photochemical production, as well as down mixing from the stratosphere.

Although ozone is a naturally occurring constituent of the atmosphere, it is considered a pollutant when it occurs in sufficiently high concentrations. Ozone, when found in high concentrations, has deleterious effects on human health (Lippman, 1989; Bates, 1994), as well as on the growth of many types of plants, including a number of economically important species (Heck et al., 1982; Adams et al., 1989; Wright, 1988). Effects on human health may begin at ozone concentrations below 80 ppb (Brauer and Brook, 1996; Bates, 1995a; 1995b). Damage to plants and reduced crop yields are seen at concentrations as low as 50 ppb (Heck et al., 1982).

The main photochemical process by which ozone is produced in the troposphere is a series of three reactions involving nitrogen monoxide (NO), nitrogen dioxide (NO_2), atomic oxygen (O), molecular oxygen (O_2) and ozone.

$$NO_2 + h\nu \rightarrow NO + O \tag{1.1}$$

$$O + O_2 + M \rightarrow O_3 + M \tag{1.2}$$

$$NO + O_3 \rightarrow NO_2 + O_2 \tag{1.3}$$

M represents a third atom or molecule which does not take part in the reaction, but is required in order for momentum to be conserved. The photolysis of nitrogen dioxide requires near ultraviolet light with wavelength between 295 and 420 nm (represented by hν in Equation 1.1). The steady state condition which results from the above three reactions is governed by the photostationary equation (Finlayson-Pitts and Pitts, 1993):

$$[O_3] = K\frac{[NO_2]}{[NO]} \tag{1.4}$$

where K is the light dependent rate constant. The steady state ozone concentration from this equation is about 30 ppb (parts per billion by volume), for unpolluted atmospheric levels of NO and NO_2, during bright sunlight. This agrees reasonably well with measured ozone levels at clean air sites. Maximum hourly ozone concentrations at clean, remote monitoring stations are typically 30-60 ppb (McCurdy, 1994; Finlayson-Pitts and Pitts, 1993).

Photochemical production of ozone is enhanced by anthropogenic emissions of ozone precursors. The most important precursors are oxides of nitrogen, collectively known as NO_x, and a huge group of chemicals referred to as volatile organic hydrocarbons (VOCs). NO_x participates directly in the reactions producing ozone (Equation 1.1 - 1.3). The importance of VOCs is that they oxidise NO to NO_2 without consuming ozone.

NO_x represents the sum of NO and NO_2. Most NO_x is emitted, in the form of NO, by combustion processes - for example thermal power generation and automobile engines. The ratio of NO_2 to NO will generally increase over the course of a day, as NO is oxidised to NO_2.

VOCs derive from both anthropogenic and biogenic sources. Examples of anthropogenic VOCs are the alkenes, the alkanes and formaldehyde. Important anthropogenic sources include

combustion, petroleum refining and distribution, and industrial solvents. The principal biogenic source is emission of compounds such as isoprene and terpenes from vegetation.

Emissions of these precursors from urban areas result in ozone levels that regularly exceed the threshold for harmful effects on humans. Hourly average concentrations exceeding the World Health Organisation standard of 77-102 ppb regularly occur around a number of urban areas in the US, Canada and Europe (McCurdy, 1994; Environment Canada, 1994; National Research Council (NRC), 1992). Cities such as Los Angeles and Mexico City occasionally experience hourly levels higher than 400 ppb (McCurdy, 1994). Elevated ozone levels are not restricted to the urban source areas, but may be found for long distances downwind, due to long range transport of ozone and ozone precursors. In fact there is significant evidence that background levels of tropospheric ozone have increased throughout most of the Northern Hemisphere, since the earliest measurements were taken around the turn of the century (Crutzen, 1987).

High ozone levels are observed to occur when conditions favourable for photochemical production (high light levels and high temperatures) occur together with meteorological conditions that limit mixing of the atmosphere and subsequent dispersion of pollutants.

In temperate mid latitude areas, atmospheric conditions that most often lead to ozone pollution episodes are slow moving, high pressure systems during the summer months. Atmospheric subsidence during these high pressure systems tends to suppress boundary layer growth, resulting in smaller mixing heights (Vukovich and Fishman, 1986; Comrie, 1990; Steyn et al., 1990). Clear skies prevalent under these conditions generally result in high daytime temperatures, which in turn act to enhance the photochemical production processes.

Regulatory efforts by various government agencies to control the problem of photochemical ozone pollution have focused primarily on the control of VOC emissions (NRC, 1992). Two decades of this strategy have brought only incremental reductions in ozone levels. The failure of this strategy has been blamed on an underestimate of anthropogenic VOC emissions and the failure to take biogenic emissions into account. It now appears that successful ozone abatement strategies must include NO_x emission controls in addition to, or instead of VOC controls (NRC, 1992).

To make quantitative predictions of the reduction in ozone levels that would be brought about by a given reduction in precursor emissions, it is essential to have a quantitative understanding of meteorological and chemical processes that result in formation, transport and destruction of ozone within the atmosphere and at the surface. Because of the large number of processes and variables involved, mathematical models of the physical and chemical processes prove essential to the study of the problem (NRC, 1992). Field and laboratory studies are also necessary, both to provide sets of data for model validation, as well as to improve our understanding of the basic processes involved.

1.2 Ozone in the Lower Fraser Valley, British Columbia

The Lower Fraser Valley (LFV) is the coastal plain formed by the delta of the Fraser River where it flows into the Strait of Georgia. A map of the region is shown in Figure 1.1. It is bounded on the north by the Coast Mountains and on the southeast by the Cascade Mountains. To the west and southwest, it is bounded by the Strait of Georgia, a large body of water lying between Vancouver Island and the mainland of British Columbia (BC). The Fraser River itself

Figure 1.1: Map of the Lower Fraser Valley showing the field site at Pitt Meadows Airport as well as the nearby Harris Road site.

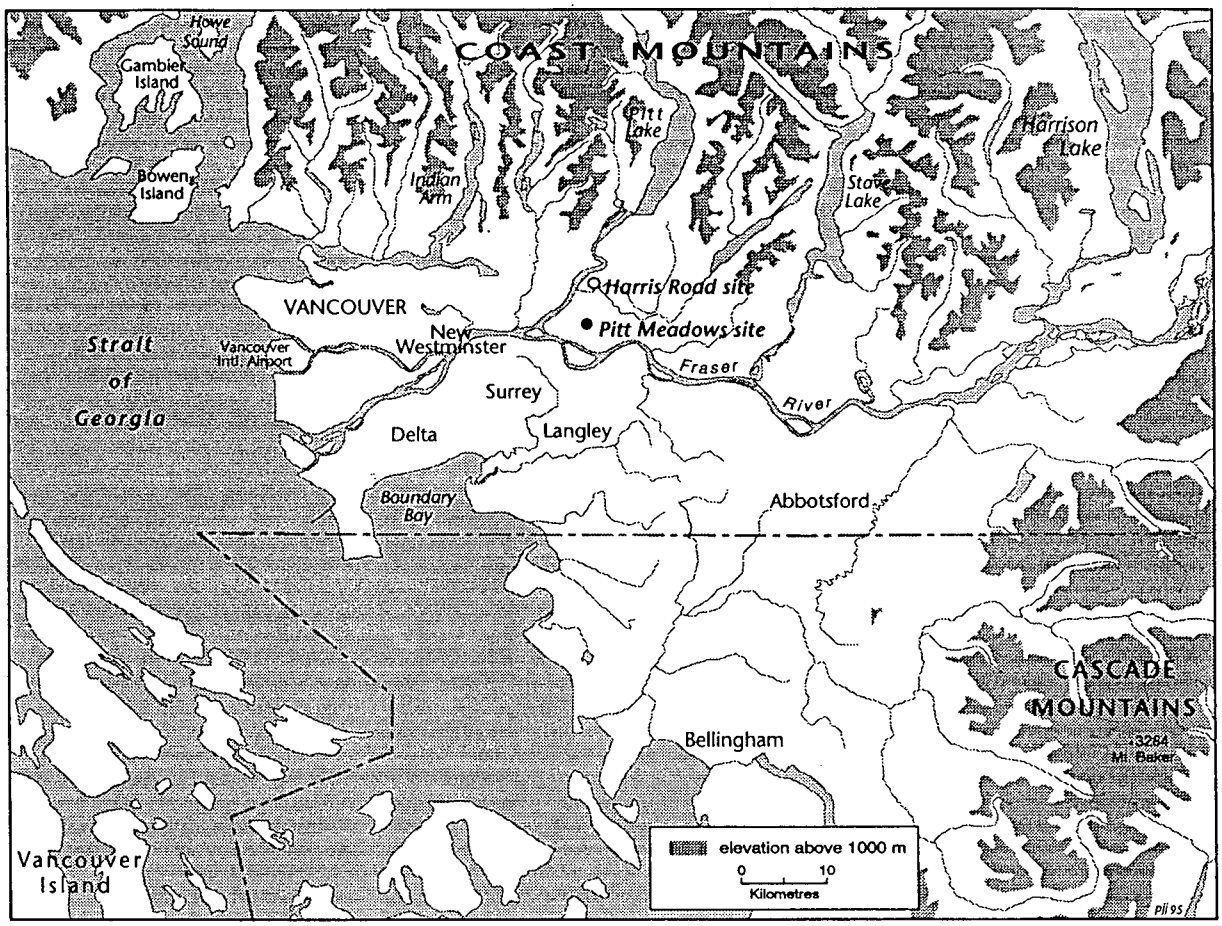

Figure 1.2: Schematic diagram of mean daytime boundary layer structure.

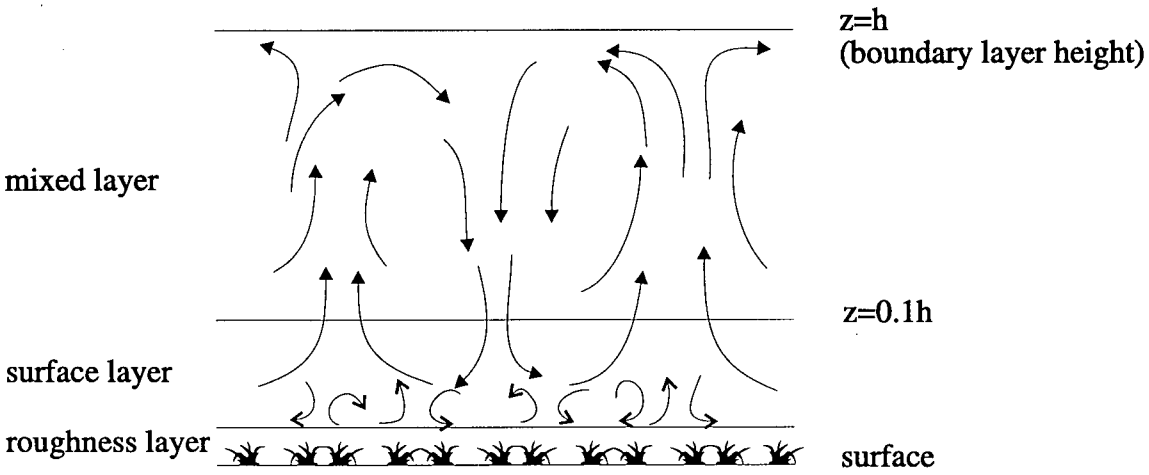

cuts through the middle of the region, flowing west to the Strait of Georgia. The LFV is split by the international boundary, with the greater portion of the region lying to the north of the boundary in BC.

The valley floor of the LFV is quite flat and low-lying. Elevations within this area range from sea level to a few hundred metres. The valley walls rise quite steeply to elevations of 1000 to 2000 metres.

The metropolitan area of Greater Vancouver is located within the LFV. The most heavily urbanized portions of the LFV lie in the northwest portion of the region, north of the Fraser River. Suburban areas extend to the south and east. Further to the east and south, areas of urban development are increasingly mixed with farmland, which is the predominant landuse type throughout much of the region. Mountain slopes bounding the region are covered with a dense growth of predominantly coniferous second growth forest.

The LFV is home to roughly 1.7 million people, about two thirds of the population of BC. It is currently the fourth most rapidly growing metropolitan area in North America (GVRD, 1994). The area is also home to a wide variety of different industries.

Emissions of precursor pollutants in the LFV regularly produces episodes of photochemical smog, with high levels of ozone. The National Ambient Air Quality Objective for ozone is 82 ppb as an hourly average. This level was exceeded at one or more monitoring stations in the LFV on 8.5% of July-September days in the period from 1984-1992 (Pryor et al., 1995).

A great deal of research on air quality issues related to ozone has been done in the LFV. A major goal of this research is to model the build-up of ozone in the region. Once the models

are calibrated properly, they can then be used to model the outcome of changing precursor emissions. Currently the dynamical portion of the modelling is done by the CSU RAMS model (described by Pielke et al., 1992). Meteorological fields output from the RAMS model are used as input for the Urban Airshed Model (UAM-V) (described in Systems Applications International, 1995) which models the diffusion, advection, chemical transformation, and surface deposition processes for a large number of chemical species, and outputs the resulting concentrations. Modelling efforts are currently underway (Steyn et al., 1996).

In 1993 an intensive field program, Pacific 93, was carried out in the LFV. Ozone and many other species were measured on ground, and by aircraft (Steyn et al., 1996). Vertical profiles of ozone, nitrogen dioxide, humidity, temperature and wind speed were measured at several locations. Two lidars were used to investigate wind fields and aerosol distribution.

One rationale for the field program was to "capture" an episode of photochemical ozone pollution that could then be used for validation of the models. Perhaps more importantly, the measurements are being used to refine our understanding of the processes leading to ozone formation and transport in the LFV.

1.3 Dry deposition

The processes responsible for the formation, destruction and transport of ozone may be represented by a conservation equation which relates the time rate of change of ozone concentration to the transport, sources and sinks of ozone.

The equation of conservation for a scalar quantity, C, within a turbulent flow is given by Stull (1988).

$$\frac{\partial \overline{C}}{\partial t} + \frac{\overline{U_j}\partial \overline{C}}{\partial x_j} = \nu_c \frac{\partial^2 \overline{C}}{\partial x_j^2} + S_c + \frac{\partial \overline{(u_j' c')}}{\partial x_j} \qquad (1.5)$$

(I) (II) (III) (IV) (V)

Equation 1.5 contains terms representing the following processes: (I) local storage of the scalar, (II) advection of the scalar by the mean wind, (III) molecular diffusion of the scalar, (IV) body sources or sinks of the scalar (for instance chemical production or destruction), and (V) flux divergence of the scalar. Overbars represent time averages; while primed quantities are instantaneous values. U_j are the vector components of wind velocity and x_j are the spatial coordinates.

One possible source of vertical flux divergence is a surface source or sink of the tracer that is not balanced by transport through the top of the boundary layer. This is the case for many trace constituents of the atmosphere, which may be absorbed at the surface, emitted by the surface, or in some cases both.

Ozone is highly reactive with a wide variety of surface types, and is therefore continuously removed at the surface by the process of dry deposition. Dry deposition of a substance may be defined as the removal of that substance from the atmosphere, by absorption or reaction at the surface, without the mediation of precipitation, fog or cloud processes.

The rate of dry deposition of ozone depends on surface propensity to react with or absorb ozone, as well as the degree of turbulent mixing in the atmosphere which determines the rate at which ozone is transported to the surface.

The portion of the atmospheric boundary layer just above the roughness sublayer up to 10% of the height of the boundary layer (Figure 1.2) is referred to as the surface- or constant flux-layer. Within this region, which is considered to be too shallow for there to be significant

sources or sinks of momentum or scalars such as heat or pollutants, the flux of a quantity at any level is equal to the surface flux within our ability to measure it (Wyngaard, 1990). Thus, surface deposition of a pollutant such as ozone can be determined by measuring the downward flux of the pollutant using one of the standard techniques for flux measurement such as eddy correlation or flux-gradient methods.

The flux, F_C, towards the surface under a given set of surface and atmospheric conditions is directly proportional to the concentration at a given height, z. To remove this concentration dependence the deposition velocity, v_d, is defined:

$$v_d = \frac{F_C}{C(z)} \tag{1.6}$$

By analogy with Ohm's law, a resistance, r, to ozone deposition can be defined; where the ozone concentration at height z is analogous to potential, and the downward flux of ozone is analogous to current.

$$r = \frac{C(z)}{F_C} = \frac{1}{v_d} = r_a + r_b + r_{surf} \tag{1.7}$$

This resistance can be subdivided into component resistances. The total resistance can be assigned to an aerodynamic resistance, r_a; a quasi-laminar sublayer resistance, r_b; and a surface resistance, r_{surf}. Aerodynamic resistance is the resistance to ozone transport from measurement height down to the quasi-laminar sublayer. Laminar sublayer resistance is the resistance to transfer through the quasi-laminar sublayer. Surface resistance is the resistance of the surface to the uptake of ozone.

The aerodynamic resistance is given (Baldocchi et al., 1987) by:

$$r_a = \frac{1}{ku_*}\left[\ln\left((z-d)/z_0\right) - \psi_h\right] \tag{1.8}$$

where u_* is the friction velocity; k is von Karman's constant (0.4); z_0 is the roughness length; d is the displacement height; and ψ_h is the integral form of the diabatic stability correction term for heat transfer. It is assumed that the stability correction function for heat transfer is applicable to ozone transfer. Aerodynamic resistance is primarily a function of wind speed and atmospheric stability. It is also affected by surface properties, inasmuch as roughness length and displacement height are affected by the arrangement, density and height of surface roughness elements.

Laminar sublayer resistance is an 'excess' resistance introduced to account for the difference between momentum and heat or mass transfer in the immediate vicinity of the surface. It is given (Baldocchi et al., 1987) by:

$$r_b = \frac{1}{ku_*}\left[\ln(z_0 / z_C\right] \tag{1.9}$$

where z_C is the roughness length for ozone. Since z_C would be extremely difficult to evaluate, this resistance is usually parameterized in terms of the sublayer Stanton number (a non-dimensional heat transfer coefficient), B.

$$kB^{-1} = \ln\left(z_0 / z_C\right) \tag{1.10}$$

Galbally and Roy (1980) suggest the following parameterization for B as an approximation valid for a wide variety of vegetation.

$$B^{-1} = 10.2\, u_*^{-1/3} \qquad (u_* \text{ in } ms^{-1}) \tag{1.11}$$

Thus laminar sublayer resistance is a function of surface roughness and wind speed as well as the molecular diffusivity of ozone, which is subsumed in the constant. Other similar parameterizations have been suggested (e.g. Hicks et al., 1985).

The surface resistance for a simple surface such as bare soil or water is directly related to the chemical propensity of the surface to absorb or react with ozone. For a more complex

surface, such as a vegetated surface there are multiple pathways to deposition. In this case it is more useful to think of the surface resistance as being equivalent to a bulk canopy resistance, r_c, made up of a number of resistances acting in series and parallel. Bulk canopy resistance includes resistances to stomatal uptake, to deposition on leaf and stem surfaces and to deposition on the underlying soil surface. A number of models of surface resistance, that incorporate all of these pathways, have been proposed (Hicks et al., 1985; Baldocchi et al., 1987; Wesely, 1989; Padro et al., 1991, 1994; Massman et al., 1994; among others).

In observational studies of ozone deposition rates, the surface resistance is usually found as a residual from the measured and parameterized quantities.

$$r_{surf} = \frac{1}{v_d} - r_a - r_b \tag{1.12}$$

1.4 Previous studies of dry deposition of ozone

1.4.1 Measurement of ozone fluxes and nocturnal depletion

Early measurements of ozone fluxes were hampered by the lack of ozone sensors that were either sufficiently fast responding for eddy correlation measurements, or stable and accurate enough for gradient measurements.

The first measurements of ozone flux were made by Regener (1957), over grassland in Nebraska. He used the flux-gradient method, and equated the transport coefficients of ozone and momentum, a practice which we now know to be questionable (Droppo, 1985).

Galbally (1971) reported on further ozone flux measurements using the flux gradient method. Most of his measurements were under near-neutral conditions over grassland. Galbally

interpreted his measurements with a greater understanding of surface layer processes than had been available to Regener in 1957. He found that vertical eddy transport of ozone in the surface layer was more similar to heat and water vapour transport than to momentum transport. Galbally also defined a "destruction coefficient" for ozone that is equivalent to the reciprocal of surface resistance as defined here. His measurements, however, were not accurate enough to see any systematic differences in deposition rates over a number of different surfaces.

Garland and Penkett (1976) performed measurements of ozone and peroxy acetyl nitrate (PAN) depletion in a return flow wind tunnel with a grass surface. They concluded, on the basis of their measurements, that deposition to vegetated surfaces was sufficient to explain the observed nocturnal depletion of ozone and PAN. Unfortunately, they did not consider effects of deposition onto the other surfaces of the tunnel.

Garland and Derwent (1979) compared night-time profile measurements of ozone with a computer simulation of a depositing gas in the nocturnal boundary layer. Their work confirmed that deposition, rather than gas phase reactions, was the primary cause for nocturnal depletion of ozone, at least in unpolluted areas. Their modelling suggested that nocturnal depletion of ozone would be confined to a shallow (order of 30 m) layer, above which a residual layer would remain, effectively isolated from interaction with the ground by the development of the nocturnal temperature inversion.

Work by Colbeck and Harrison (1985) confirmed the existence of a shallow ozone depleted layer. They measured night-time profiles of ozone and temperature from surface to 100 m with a tethered balloon, during a period of fine weather and high ozone levels. Their results clearly show the development of an ozone-depleted temperature inversion layer.

McKendry et al. (1996a) also analyzed balloon profiles of ozone concentration. They showed the importance of the residual ozone layer in contributing to the rapid rise in surface ozone concentrations often observed in the morning.

The first eddy correlation measurements of ozone deposition were taken over maize canopies (Wesely et al., 1978). Their measurements showed that stomatal resistance was the most important factor controlling overall canopy resistance to ozone deposition. They estimated canopy resistance to water vapour transfer (a measure of effective stomatal resistance) from their measurements. By comparing this to the canopy resistance for ozone, they were able to estimate the relative importance of stomatal uptake versus deposition on leaf surfaces and soil. During the day they found that stomatal uptake accounted for about 80% of ozone deposition. Around dawn and dusk the proportion dropped to roughly 50%.

Wesely et al. (1978) also describe a typical diurnal cycle of bulk canopy resistance. An idealized depiction of their results is shown in Figure 1.3. In the early hours of the morning, resistance is fairly high (200-300 sm^{-1}). This is due to relatively high stomatal resistance because of lower light levels; and relatively high resistance to deposition on the leaf surfaces because they are still covered with dew. During mid-morning and early afternoon resistance is at its lowest (100 sm^{-1}) because the stomata are fully open and the leaf surfaces have dried. As the day progresses, bulk canopy resistance increases because increasing water stress causes the stomata to partially close. Typical mid and late afternoon values of the bulk canopy resistance are in the range 200 to 400 sm^{-1}. Around sunset there is a sharp increase in the bulk canopy resistance caused by stomatal closure associated with falling light levels. The resistance increases

Table 1.1: Measurements by previous investigators of surface resistance to ozone deposition

Surface Type	Study	Surface Resistance ($s \bullet m^{-1}$)
healthy maize (daytime)	Wesely et al., 1978	100-200
senescent maize (daytime)	Wesely et al., 1978	200-400
wheatgrass (daytime)	Delany et al., 1986	130
grassland	Galbally and Roy, 1980	100
grassland	Colbeck and Harrison, 1985	140
lake water	Wesely et al., 1981	9000
fresh water	Galbally and Roy, 1980	3200-4100
bare wet soil	Wesely et al., 1981	1000
bare wet soil	Galbally and Roy, 1980	800-1600
dry soil	Galbally and Roy, 1980	100-400
snow	Wesely et al., 1981	3400
fresh snow	Stocker et al., 1995	2200
aged snow	Stocker et al., 1995	800
pine forest (daytime)	Lenschow et al., 1982	50
pine forest (daytime)	Greenhut, 1983	130
deciduous forest (daytime)	Padro, 1993	80-200
ocean water	Lenschow et al., 1982	1800
ocean water	Galbally and Roy, 1980	2200-3100
tundra (daytime)	Jacob et al., 1992	260

Figure 1.3: Idealized diurnal course of surface resistance over a vegetated surface (adapted from Wesely et al., 1978 and Padro, 1993).

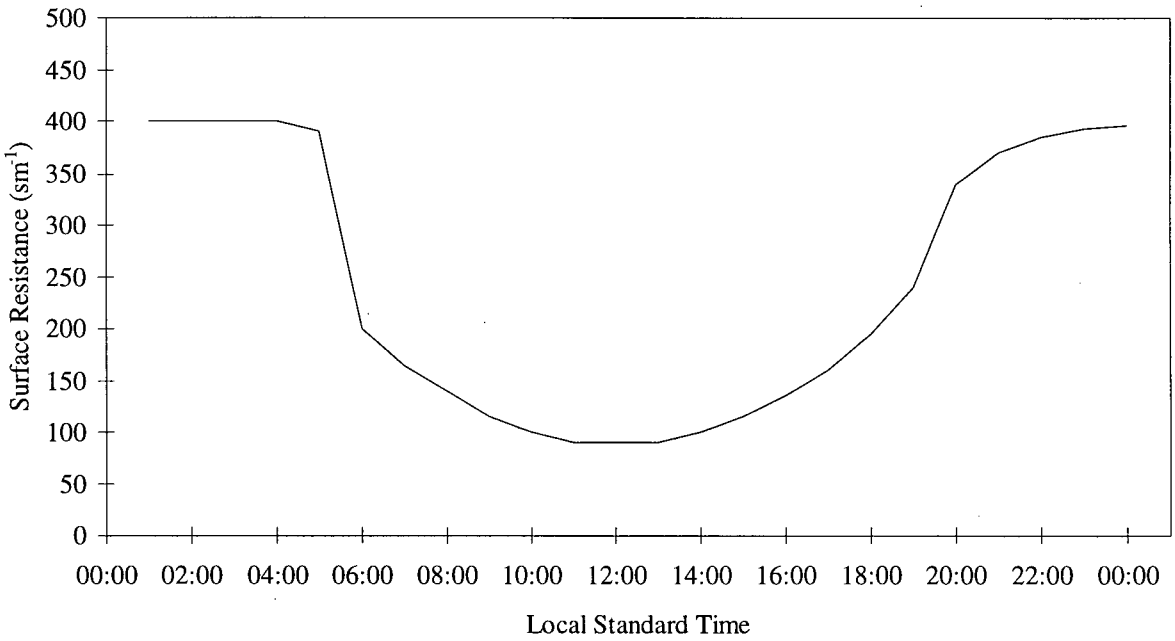

gradually overnight because of increasing dewfall through the night. Sunrise brings a sharp fall in resistance as stomata again open due to increasing light levels.

Wesely et al. (1981) also used eddy correlation techniques to measure ozone fluxes to soil, water and snow. Their results, as well as that of a number of other more recent investigations, are summarized in Table 1.1.

Lenschow et al. (1982) took eddy correlation measurements of ozone fluxes from aircraft, over forest and ocean. Their measurements are included in Table 1.1. Since their pioneering efforts, measurements of ozone fluxes from aircraft have been used in a number of studies (e.g. Godowitch, 1990; Greenhut, 1983; MacPherson, 1993). These studies offer a degree of spatial integration that is not possible using fixed tower based flux measurements. However, aircraft flux measurements do have some disadvantages. Generally measurements can not be taken as close to ground as with tower measurements. It is also more difficult to concentrate on a particular surface type in detail. Since aircraft measurements are taken at greater heights, the assumption that the measured flux is equal to the surface flux may be violated if there is flux divergence or convergence in the intervening layers. Chemical reactions and advective effects due to mesoscale inhomogeneities are both possible sources of flux convergence.

Galbally and Roy (1980) took a large set of surface resistance measurements by measuring the decay in ozone levels within a Mylar chamber erected over a number of natural and artificial surfaces. Some of their results are included in Table 1.1. Their work confirmed the diurnal cycle of surface resistance for vegetated surfaces.

The values of surface resistance compiled in Table 1.1 show that there is reasonable agreement between different sets of measurements over most surfaces. Caution should be used

when comparing different values taken over vegetated canopies since the surface resistance will in general be a function of the vegetation type and vegetation density. It will also be a function of the micrometeorological conditions at time of measurement, inasmuch as they control stomatal resistance. Among natural surfaces, the most densely vegetated surfaces generally have the lowest surface resistances. Bare soil, dead vegetation, snow, and water have successively higher surface resistances.

1.4.2 Dry deposition over heterogeneous terrain

Two studies in Switzerland (Broder et al., 1981; Broder and Gygax, 1985) investigated ozone budgets within a mountain valley. They found that nocturnal downslope winds within the valley greatly enhanced dry deposition of ozone during the night-time hours. The winds continually resupplied ozone-rich air to the valley slopes so dry deposition was active throughout the night. A great deal of ozone, and presumably other pollutants as well, were removed from the entire air column in the valley by this process.

These studies are highly relevant to the situation in the LFV. The LFV has several tributary valleys that have well developed local wind systems. McKendry et al. (1996b) investigated air quality and local circulations in the Pitt Lake tributary valley of the LFV. They found that a great deal of polluted air is advected up this valley during the daytime hours. High concentrations of ozone were observed well up the valley, probably partly due to reduced dry deposition over the lake-covered valley bottom. During the night-time hours a nocturnal jet, of air cleansed by dry deposition along the valley slopes, was observed flowing out of the valley (Banta et al., 1996).

A recent study (Mahrt et al., 1994) measured ozone, heat, moisture, CO_2, and momentum fluxes from low level (30 m) aircraft flights over a sequence of irrigated and dry non-irrigated fields. They found that the observed fluxes were significantly affected by mesoscale motions induced by the surface heterogeneity as well as by mesoscale motions of unknown origin. Their results also showed that correlation among the fluxes of heat, moisture and ozone and CO_2 varied above the different surface types. These results suggest some caution is warranted when making the usual assumptions of similarity of transport among these scalars. However, the applicability of these findings to surface based flux measurements, generally taken closer to the ground, is uncertain. The effect of mesoscale heterogeneity on surface fluxes is an active field of research at present.

1.4.3 Parameterization of dry deposition

Much of the work on dry deposition since the mid 1980s has concentrated on developing parameterizations of the deposition process in terms of underlying variables that are commonly modelled or measured. Baldocchi et al. (1987) discuss requirements for a dry deposition parameterization scheme. Since the stomatal pathway is often the most important for ozone deposition and is also the most sensitive to environmental conditions, it is important to model stomatal resistance as accurately as possible.

Hicks et al. (1985) discuss a method for inferring deposition velocity from routine meteorological measurements for use in a proposed dry deposition monitoring network. Baldocchi et al. (1987) formulated a more detailed model of surface resistance that included the effects of light transmission through the canopy on stomatal resistance. Their model also included

the effects of leaf water potential and humidity on stomatal resistance. While these refinements would be expected to lead to more accurate modelling of dry deposition, the required parameters may not be routinely available from air quality models or measurement programs.

Wesely (1989) presented a simple model of surface resistance designed to be incorporated into numerical air quality models. Wesely's model (W89) has lookup tables for different landuse and seasonal categories. It incorporates the effect of radiation and surface temperature on stomatal resistance. Comparisons of W89 model predictions to measured surface resistances (Padro et al., 1994) have shown reasonable agreement between the two. The W89 model is the dry deposition scheme incorporated into the UAM-V model, used for air quality modelling in the LFV.

1.4.4 Alternate methods of flux measurement

Droppo (1985) compared measurements of ozone fluxes using the flux-gradient and eddy-correlation methods. Assuming similarity of ozone eddy transport to eddy transport of heat, he found very good agreement between the two methods. Nevertheless, the eddy correlation method has been most widely used in recent years. It is preferred by most researchers for several reasons:

- it involves fewer empirical assumptions than the flux-gradient method
- it has less stringent requirements for the absolute accuracy of the sensor
- and it is readily adaptable for aircraft-based measurements.

Wesely (1988) employed the variance method to measure surface exchange of ozone and sulfur dioxide over a field of soybeans. He reported good success with two forms of the method (see Chapter 2 for a description of the method). However he also found that instrumental noise in

the chemical sensors can spuriously increase the variance and lead to significant overestimation of the fluxes using this method. His results, when compared with eddy correlation measurements taken at the same time, showed that transport of water vapour was a better analog for ozone transport than was heat flux. Padro et al. (1992), in a similar experiment conducted over a deciduous forest canopy, also found that high frequency noise from the chemical sensors was a problem. They also found that the flux-variance relations used by Wesely (1988) had to be adjusted with site specific constants to give best agreement with the data.

Another method of flux measurement was suggested by Hicks and McMillen (1988). Their method relies on an assumption of cospectral similarity between pollutant transfer (sulfur dioxide in the case of their study) and heat and water vapour transfer. The major advantage of their method is that it could offer a significant reduction in the sampling speed necessary to measure scalar fluxes. Their method used a ratio of band-pass covariances of heat, water vapour and SO_2 with vertical velocity to infer the flux of SO_2. They compared their measurements to eddy correlation measurements taken simultaneously and found that their method gave acceptable accuracy with (simulated) instrument response times as long as 30 seconds.

1.5 Rationale and objectives of the research

A substantial number of researchers have taken measurements of ozone deposition rates and the corresponding deposition velocities. However to date, no measurements of ozone deposition have been made in the LFV where a major photochemical modelling effort is underway. Where surface types are quite similar between locations we expect that surface resistances obtained in one locale will be directly applicable to other locales. If the surface types

are significantly different between locales, as would be the case if different plant species make up the ground cover, we might expect the deposition rates to be different.

The objectives of this research are severalfold:

- To obtain measurements, using the eddy correlation technique, of surface resistance to ozone deposition over moist grassland, a common surface type in the LFV. These measurements can then be compared to measurements taken elsewhere, as well as to surface resistance values calculated using the W89 surface resistance algorithm. The measurements provide a means to verify a portion of the model which is being used to simulate ozone levels in the LFV. If shortcomings are identified in the W89 model, this knowledge will be useful to those using the UAM to simulate ozone episodes in the LFV.
- To use the measured time series from the eddy correlation measurements to test the simplified method of flux measurement suggested by Hicks and McMillen (1988). This method uses an assumption of cospectral similarity between temperature, water vapour and sulfur dioxide transport to circumvent the rapid sampling speed requirements of the eddy correlation method. An analogous method, based on temperature and ozone transport can be tested using the time series from this measurement program. An investigation of the cospectra of vertical velocity with temperature and ozone can address the underlying assumption of the method.
- To compare the ozone fluxes obtained from the flux-gradient method and the variance method to measurements taken using eddy correlation techniques. The utility of these techniques for ozone deposition measurements can be determined in this manner.

2. TURBULENT FLUX MEASUREMENT AND THE FIELD PROGRAM

2.1 Measurement of turbulent fluxes

Surface exchange of trace gases such as ozone may be measured using a variety of approaches. One approach is to use a micrometeorological technique to measure transport in the atmosphere above the surface. Another approach is to use an enclosure method, where changes in the mean concentration are measured within an enclosure over the surface of interest (e.g. Galbally and Roy, 1980). Only micrometeorological techniques will be discussed here.

The most direct micrometeorological method is to directly measure the vertical component of wind speed and the mass concentration above the surface. Assuming horizontal homogeneity, stationarity and zero mean vertical velocity, the vertical flux is simply the time average of the instantaneous product of the fluctuations of vertical velocity and concentration (Equation 2.1). This method is referred to as the eddy correlation technique.

$$F_C = \overline{w'c'} \tag{2.1}$$

Since turbulent fluctuations are by nature irregular and occur over a wide variety of scales, it is necessary to average the measurements to obtain a stable estimate of the covariance. Lenschow and Kristensen (1985) present the following equation for the averaging time, P, required for a given error, ε_C, in the estimation of a covariance between a scalar and vertical velocity:

$$\varepsilon_C^2 = \frac{4\sigma_w^2 \sigma_c^2}{F_C^2 P} \min(\Gamma_w, \Gamma_C) = \frac{4}{r_{wc}^2 P} \min(\Gamma_w, \Gamma_C) \tag{2.2}$$

where Γ_w and Γ_C are the integral time scales for vertical velocity and scalar concentration, σ_w and σ_c are the standard deviations of vertical velocity and scalar concentration and r_{wc} is the correlation coefficient between vertical velocity and scalar concentration.

The integral time scale can be estimated from Kaimal (1972) and Kaimal and Finnigan (1994). Under near neutral conditions the integral time scale for vertical velocity is given by:

$$\Gamma_w \approx 0.5\frac{z}{u} \tag{2.3}$$

Given a measurement height of 4 m, and a mean wind speed of 2 ms^{-1}, the expected error for a 1/2 hour sampling period is about 20% (given an assumption of $r_{wc} = 0.4$). Halving this error requires an averaging period four times as long. Generally averaging over periods longer than 1 hour is not recommended since the stationarity assumption will almost certainly be violated by diurnal or other changes in the mean values and/or the variances of the measured quantities (Dabberdt et al., 1993).

To include the effects of the smallest eddies important in transporting the flux, instruments with rapid response time (on the order of 0.1 s) are required to measure vertical velocity and concentration. The high frequency cut-off of such instruments will be well into the inertial subrange where spectral energy is rapidly decreasing (Kaimal and Finnigan, 1994). A digital sampling rate corresponding to one sample per integral time scale of the turbulence is most efficient since successive samples will be independent. The integral time scale for vertical velocity is given by Equation 2.3. For temperature and other scalars the integral time scale is roughly 10 times greater (Kaimal and Finnigan, 1994), during unstable or near neutral conditions.

Usually, a digital sampling rate at least commensurate with the frequency response of the instruments (i.e. about 10 Hz) is chosen. This sampling rate is very conservative for the flux

calculations (far fewer samples are needed). However, for defining the turbulent spectra and cospectra, this sampling rate is necessary both to define the spectrum over a large bandwidth and to avoid aliasing (Wyngaard, 1990).

Although eddy correlation is the most fundamental method of flux measurement, it is not always feasible or practical. For many chemical species of interest, sufficiently rapid-response sensors do not exist. The flux-gradient or profile method is an alternate form of flux measurement that does not require rapid response instruments. In the surface-layer, a first order turbulent closure assumption that relates the flux of a species to its vertical gradient is often made (Kaimal and Finnigan, 1994):

$$\overline{w'c'} = K_C \frac{dc}{dz} \tag{2.4}$$

K_C, the coefficient which relates the flux to the gradient, is known as the eddy diffusivity.

The eddy diffusivity is a function of stability and surface shear. Monin-Obukhov similarity theory, combined with experiment can be used to determine the functional form for K_C. The appropriate similarity functions are given by Dyer (1974).

$$K_C = \frac{k u_* z}{\phi_C} \tag{2.5}$$

and assuming that the similarity functions for heat and ozone are identical ($\phi_c = \phi_h$)

$$\phi_C = \begin{cases} (1+16|z/L|)^{-\frac{1}{2}} & -2 \le z/L \le 0 \\ (1+5(z/L)) & 0 \le z/L \le 1 \end{cases} \tag{2.6}$$

These similarity functions depend only on the Obukhov parameter (also referred to as the stability parameter); $\zeta = z/L$. L is the Obukhov length, given by the following equation:

$$L = \frac{-\rho c_p T u_*^3}{kgH} \tag{2.7}$$

The Obukhov length can be calculated directly if measurements of the friction velocity and the heat flux, H, are taken. Otherwise it may be estimated iteratively from profiles of temperature and wind speed in the surface layer (Berkowicz and Prahm, 1982).

The gradient method has several disadvantages. Since the gradients are usually quite small compared to the average concentrations, very accurate measurements of the mean concentration at two or more levels are required. Typically, errors of 1% in the mean concentrations might lead to errors of 10% to 100% in the gradient (Wyngaard, 1990). Furthermore, similarity relations used to relate the fluxes to the gradients are themselves only accurate to 20% (Wyngaard, 1990). Finally, one must assume similarity between the transport of heat and other scalars, since the similarity relations are only well known for heat and momentum transfer. The assumption of similarity of transport is reasonable over simple surfaces, but has been called into question over vegetated canopies (Monteith and Unsworth, 1990).

Yet another method for measuring turbulent fluxes is the variance method. This method relates the flux of a substance to turbulent variations in its concentration. One advantage of this method is that statistically significant estimates of a variance requires a shorter sampling period than for a covariance (Businger, 1986). There are several forms of the variance method. The simplest form uses the standard deviation ratio to calculate the flux of interest, F_C:

$$|F_C| = |F_S| \frac{\sigma_c}{\sigma_S} \tag{2.8}$$

F_S and σ_S represent the flux and standard deviation of another more easily measured scalar such as temperature or water vapour. This approach is similar to a Bowen ratio approach, with standard

deviations substituting for concentration differences. Like the Bowen ratio approach, the underlying assumption is that turbulence transports the two quantities in a similar manner. A disadvantage is that it requires the measurement of at least one other flux.

Another approach is suggested by the following equation (Wesely, 1988):

$$F_C = r_{wc}\sigma_w\sigma_c \tag{2.9}$$

r_{wc} can be replaced (Wesely, 1988) by r_{wT}, the correlation of vertical velocity and temperature. r_{wT} is a quite well known function of atmospheric stability.

A third approach is to use similarity relations for σ_c/c_*, (where c_* is equal to F_C/u_*) as a function of z/L. The flux is then given by the following equation.

$$\left|F_C\right| = \frac{\sigma_c\, u_*}{f(z/L)} \tag{2.10}$$

Wesely (1988) suggests the following similarity relations for f(z/L).

$$f(z/L) = \begin{cases} 1.85 & \text{for } z/L > -0.31 \\ 1.25\,(-z/L)^{-1/3} & \text{for } z/L < -0.31 \end{cases} \tag{2.11}$$

One disadvantage of the variance method is that any variance contributed by instrumental noise, rather than atmospheric fluctuations, will increase the variance and thus bias the flux estimates. This is particularly a problem with many trace gas sensors which are inherently noisy. Another problem with this method is that only the magnitude, and not the direction of the flux is measured. However, this is not a major problem for a gas like ozone, measured near the surface, where the flux will always be downward.

The cospectral method that will be discussed in Chapter 5 is analogous to the first form of the variance method. Rather than using a ratio of standard deviations it uses a ratio of band-pass covariances with vertical velocity. This solves both problems associated with the variance

method. The instrumental noise is by definition uncorrelated with the flux transport and therefore does not bias covariance estimates, although it does increase the expected error (Lenschow and Kristensen, 1985). The direction of the flux is preserved in the signs of the covariances.

2.2 Field program

During August, 1994, field measurements of ozone flux to grassland were taken from a tower erected at the Pitt Meadows Airport, which is located in the LFV region east of Vancouver, BC. The flux measurements were taken using both the eddy correlation and gradient methods. Measurements were taken on August 10-14, 27, 30 and 31. The periods during which data were collected are summarized in Table 2.1.

2.3 Field site

Pitt Meadows Airport is located southwest of the suburban community of Pitt Meadows, and to the east of the main urban areas of greater Vancouver (Figure 1.1). The airport abuts the Fraser River on its south boundary. North and west of the airport are small farms, mostly growing blueberries, hay, pasture and a variety of nursery species. A number of homes are scattered through this area, along with several clumps of trees. Immediately east of the airport are some residential developments.

The tower used for the field measurements was erected at the northeast corner of the Pitt Meadows Airport (Figure 2.1), on a portion of the airport grounds not currently being used by the airport. The tower site (Figure 2.2, Figure 2.3) is in an area of unmaintained pastureland.

Table 2.1: Dates and times of ozone flux measurements, as well as ranges of temperature, wind speed and wind direction at Pitt Meadows Airport.

Date	Times (PDT)	Temperature Range (°C)	Wind Speed Range ($m \bullet s^{-1}$)	Wind Direction Range (°)
10/08/1994	1625-1730	27	3.6-4.0	260-270
11/08/1994	1520-1920	25-28	2.6-3.7	240-280
12/08/1994	1640-1840	24-26	3.0-3.5	175-200
13/08/1994	1235-1830	25-27	2.7-3.7	180-255
14/08/1994	1120-1700	23-25	1.8-4.1	170-210
27/08/1994	1300-2005	23-31	1.8-4.2	180-320
30/08/1994	1150-2020	19-25	1.2-3.2	155-290
31/08/1994	1150-1550	22-24	1.6-3.7	225-280

Figure 2.1: Map of Pitt Meadows airport and surrounding area, showing the field site at the northeast corner of the airport grounds.

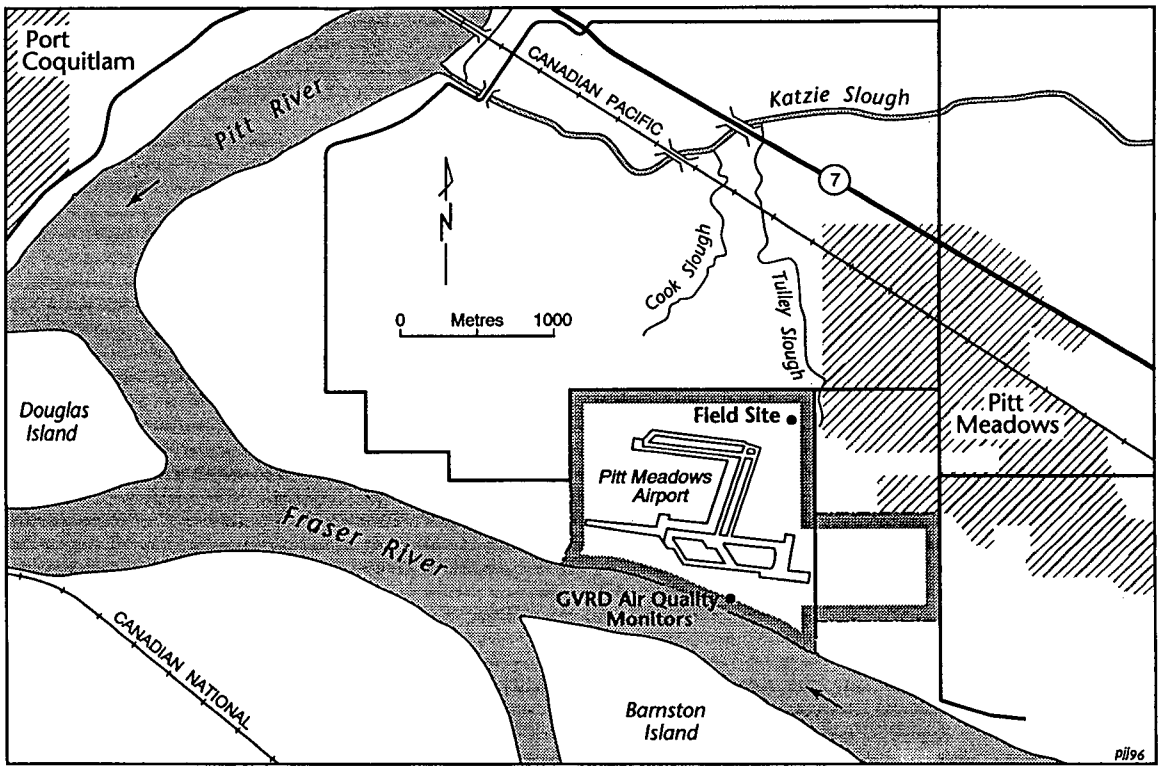

Figure 2.2: Schematic map of tower site showing roads to the north and east and houses to the east. Wind directions of south through west gave acceptable fetch over pasture.

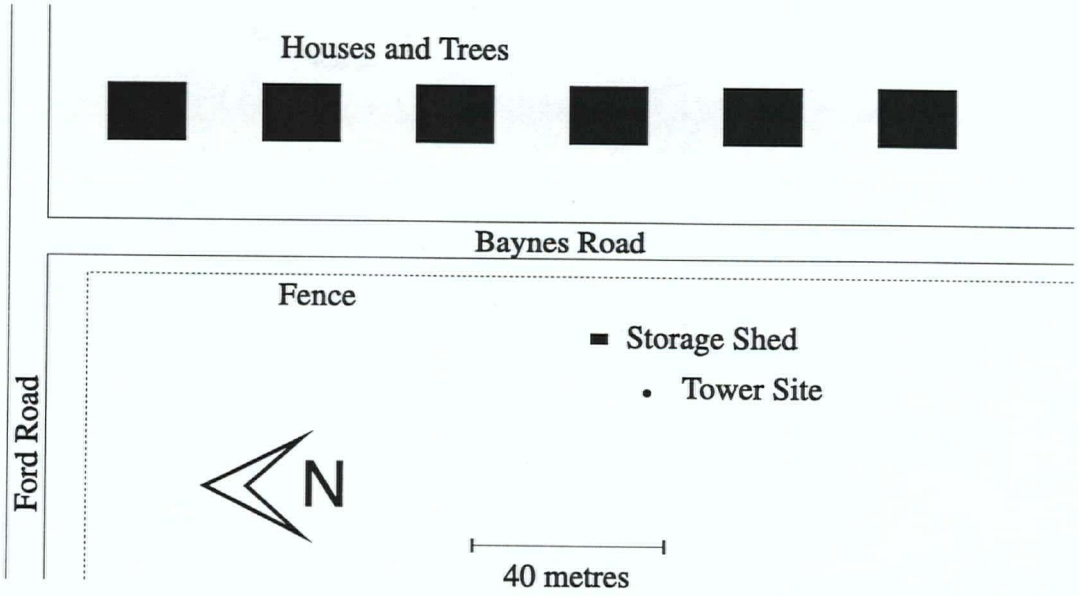

Figure 2.3: Photograph of tower site looking southwest. The Teflon tubes leading to the ozone monitor (lower left) are visible. Trees in background are 1.2 kilometres away.

There is excellent fetch of similar surface type in the southwest quadrant, and poor fetch in the other three quadrants.

The vegetation in the area is primarily a mix of grasses and rushes growing to a height of about 1.5 metres. Much of the pasture area (Figure 2.3) was still lush and green during the measurement period, but there were patches of senescent, brownish vegetation, presumably due to moisture stress during dry weather in July.

A chain-link fence, running north/south along the east edge of the airport grounds, is located 25 m east of the tower site. Just east of this fence is a two lane road leading to the airport. 35 m east of the fence is a row of houses and small trees, rising an estimated 10 m high. A similar fence, running east/west along the north edge of the airport grounds, is located 120 m north of the tower site. Immediately north of the fence is a rural road leading to a number of farms. To the north of this road are some scattered trees and farm dwellings, amid primarily pastureland.

South of the tower site, tall grassland gives way to grass cropped to 20 cm height at 300 m distance. Approximately 600 m due south of the tower is a group of warehouse style buildings, roughly 13 m high. To the southwest (Figure 2.3), there is a taxiway and runway at 400 m. Southwest of this, pastureland continues for over 1 km in this direction. West of the tower site, the pasture is continuous for 300 m. Beyond this point there is mixed pasture and tree nurseries.

Finally a small storage shed, 2 m high, 3 m long and 2 m wide was located 13 m northeast of the tower (Figure 2.2).

The site was known to have fairly high summertime ozone levels, due to its location down wind of the precursor source region of Vancouver (Steyn et al., 1990). The site is 1.3 km NNE

of the Greater Vancouver Regional District's (GVRD) Pitt Meadows air quality monitoring station (Figure 2.1) which often records elevated ozone values during the summer months (Steyn et al., 1990).

The site likely has some local sources of NO_x, mainly from residential areas to the east, and roads to the north and east. There is also a small source from the relatively infrequent landing and takeoff of airplanes. Another local source of NO_x is from agricultural burning in the area. This was observed for only one period during the study. South and west of the tower, there are no nearby, significant sources of NO_x.

A value of the roughness length, z_0, was derived from mean wind and turbulence measurements taken at the site. To calculate the roughness length, mean wind and friction velocity, measured under neutral and near neutral conditions, were used with the logarithmic wind profile to solve for z_0. The calculated roughness length was 0.137 m ± 0.03 m. This agrees quite well with the simple empirical formula; $z_0 = h/10$ (Oke, 1987), where h is the height of the roughness elements. Using this formula, the predicted roughness length for this surface is 0.15 m. The displacement height, d, for the surface, estimated as 70% of the height of the roughness elements (Jacob et al., 1992), was 1.0 m.

The soil in the measurement area is quite moist, due to the generally flat and low-lying nature of the area. No soil moisture measurements were taken during the experiment in 1994. However, we may use the record of rainfall during the month (Table 2.2) as a partial surrogate for soil moisture.

2.4 Instrument configuration

The instruments used for the study were mounted on a 6 m high, guyed, steel-latticework tower. The tower was of triangular cross-section, 25 cm on a side. The tower had a shadow factor estimated from photographs of 20%. A 5 cm diameter pole was used to extend the tower to a total height of 8.6 m. A schematic diagram of the instrument arrangement on the tower is shown in Figure 2.4 and a photograph of the tower is shown in Figure 2.3.

Instruments for the turbulence measurements were mounted on a boom extending 2 m southwest from the tower. This separation was considered sufficient to keep the instruments outside the main zone of tower affected turbulence and upstream flow distortion (Kaimal and Finnigan, 1994). The turbulence measurements were taken at a height of 4.85 m above ground, or 3.85 m above the displacement height.

Choice of measurement height is determined by several factors. Measurements close to the ground require faster response instruments because the dominant scale of surface layer turbulence is roughly proportional to height (Kaimal, 1986). A measurement height at least three times canopy height is necessary in order to be above the roughness sublayer (Kaimal and Finnigan, 1994), into the region where surface layer scaling relationships apply. Measurement at greater heights increases the effective footprint of the measurements and thus reduces the effect of small, local inhomogeneities on the measurement. However, measurement height is limited by the available fetch. Higher measurement heights require larger areas of homogenous surface upwind of sensor location. The chosen height of 4.85 m above the ground surface (3.85 m above displacement height) was a compromise between these various factors.

Given a height of 3.85 m above the displacement plane, fetch to height ratios for the sonic anemometer and ozone sonde were 300:1 for southwest winds. The corresponding ratio for

Figure 2.4: Schematic diagram of the instrument configuration on the tower showing the height above ground of the instruments. (1) cup anemometer and wind vane; (2) upper thermistor and thermocouple; (3) upper intake to ozone monitor; (4) ozone sonde and anemometer; (5) lower intake to ozone monitor; (6) lower thermistor and thermocouple.

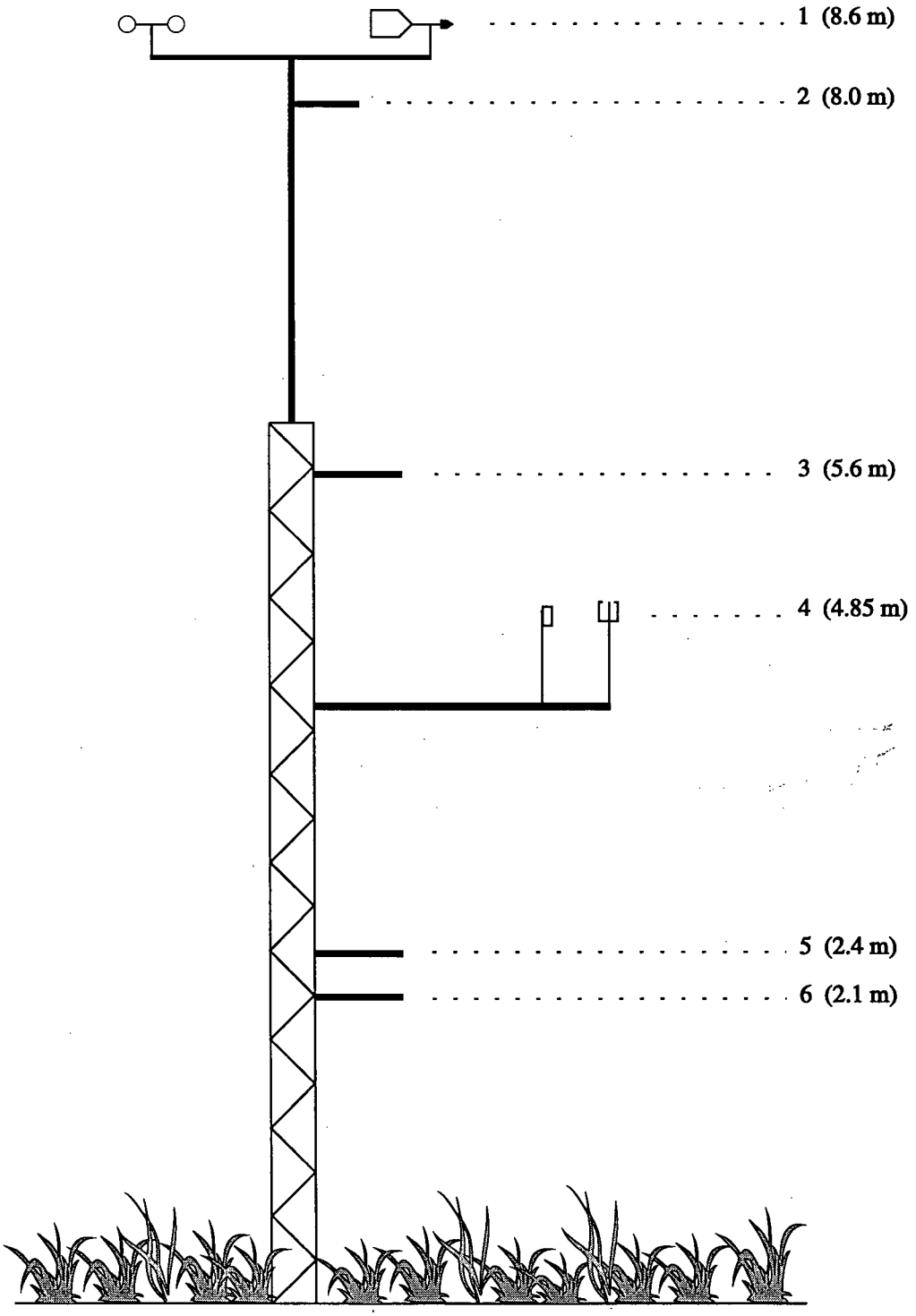

south and west winds is 100:1. The upper gradient intake had somewhat lower fetch to height ratios.

Intakes for the gradient measurements were located 0.6 m southwest of the tower supported by small booms. The lower intake was located at 2.4 m height and the upper intake at 5.6 m. These heights were chosen so that the lower intake would be several roughness lengths above the displacement height (Kaimal and Finnigan, 1994) and the upper intake would have adequate fetch. The gradient sampling lines led down the tower to the ozone monitor which was located on a small wooden pedestal 3 m northeast of the tower

Temperature was measured at two heights, 8.0 and 2.1 m. The temperature sensors were located within naturally aspirated, white radiation shields, mounted on small booms extending 0.6 m southwest of the tower.

The mean wind speed and direction were measured at the top of the tower extension at 8.6 m height.

2.5 Instrumentation

Rapid response measurements of wind speeds were taken with a 3-axis, ultrasonic anemometer (Gill Instruments, Needham, Maine, USA), (Figure 2.5). This instrument measures wind speed along three non-orthogonal axes by recording the time difference between sound pulses travelling in opposite directions along the axes between transducer pairs. The internal software of the instrument calculates the vector transformation to convert the measurements to the usual u-v-w axes. The Gill sonic anemometer also measures the speed of sound at each

Figure 2.5: Photograph of the 3-D sonic anemometer and the OSB-2 ozone sonde mounted on the boom extending southwest from the tower.

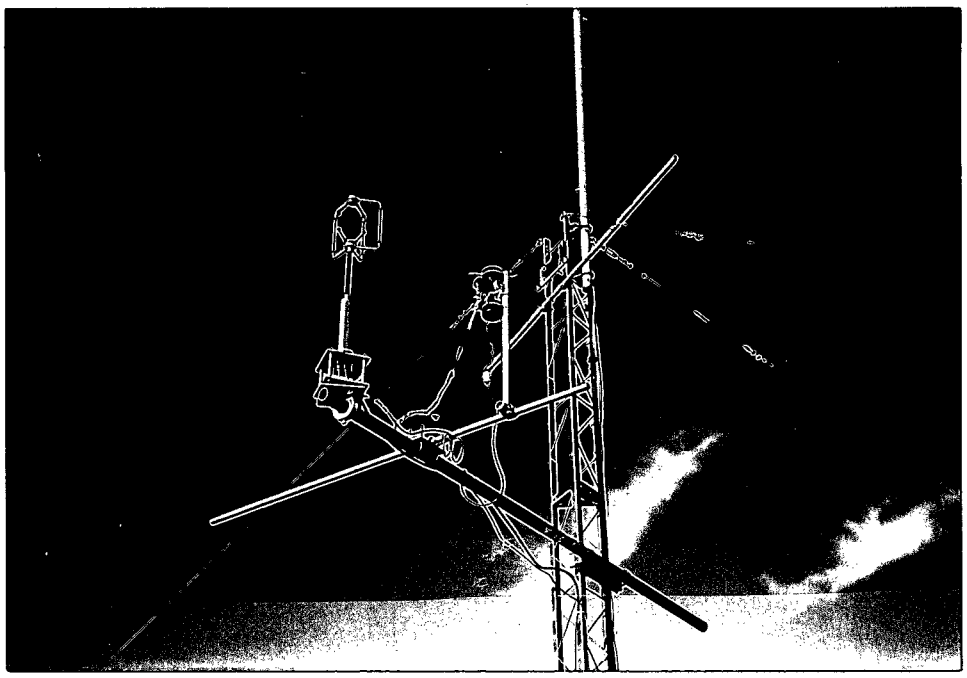

measurement period. This value can be converted to a temperature reading since speed of sound is a function of temperature.

The accuracy of the windspeed measurements is given as ±3% for instantaneous measurements and ±1.5% for 10 second averages.

Rapid response measurements of ozone concentration were made using a chemiluminescent ozone sensor of the type described by Gusten et al. (1992). The ozone sensor (model OSB-2, Gesellschaft fur angewandte Systemtechnik (GFAS), Immenstaad, Germany) used in this experiment was originally designed for stratospheric ozone measurements. The sensor detects ozone on the basis of a chemiluminescent reaction between ozone and an organic dye, Coumarin-47. Air is drawn into the instrument and passes over a disk coated with the dye. The

disk is heated to a constant temperature of 30°C to avoid changes in sensitivity due to temperature changes.

Light from the chemiluminescent reaction is detected by a photomultiplier tube mounted opposite the disk. The output circuitry of the instrument transforms current from the photomultiplier tube into a voltage proportional to the ozone mixing ratio. Light traps, at the inlet and outlet of the instrument, prevent ambient light from entering the instrument and overloading the photomultiplier tube.

The OSB-2 is suitable for eddy correlation measurements, having a 90% response time of less than 0.1 s according to Gusten et al., 1992. However, the cospectra presented in Chapter 4.3 show that there was significant attenuation of sensor response at frequencies above 1 Hz. A correction was applied to the measured ozone fluxes to account for the loss of vertical velocity - ozone covariance at these high frequencies. The correction procedure and the magnitude of the corrections are presented in Appendix A.

The OSB-2 sensor required pre-ozonization and calibration before each period of measurement. In addition, continuous calibration of the sensor with a more stable ozone monitor was found to be necessary since the ozone sensor gradually lost sensitivity over the course of a day of measurements. Details about the OSB-2 and its calibration procedure, as well as estimated errors are presented in Appendix B.

The ozone sensor was mounted on the boom adjacent to the sonic anemometer (Figure 2.5), separated by 50 cm. This was considered to be a compromise between the requirement for proximity to ensure that the same turbulent fluctuations were measured by the two sensors (Lee and Black, 1994), and the requirement for adequate separation to ensure that the flow field

measured by the sonic anemometer was not distorted by the ozone sensor. Flow distortion from the ozone sensor could have come from two sources. First, there was radial flow towards the intake, due to air being drawn in by the sensor. This was calculated to be negligible at 50 cm separation. Second, there was possible distortion of the turbulent field by flow around the ozone sensor. The ozone sensor may be approximated as a 15 cm diameter cylinder. The sonic anemometer was separated by over 3 of these diameters in an upwind or crosswind direction. This is considered adequate (Kaimal, 1986) to avoid major flow distortion.

The vertical gradient of ozone was measured using a single ozone monitor, sampling sequentially at two levels. The ozone monitor (model ML9811, Monitor Labs, East Englewood, Colorado), measures ozone by the absorption of an ultraviolet beam passed through a sample of air. It is a highly stable and accurate instrument. The monitor has a 90% response time of approximately one minute. It was calibrated at the beginning of the field season against the GVRD standard UV absorption monitor. The GVRD standard is the same instrument that is used to calibrate ozone monitors in the local air-quality monitoring network maintained by the GVRD. The two instruments agreed to within better than 1 ppb for ozone concentrations between 0 and 600 ppb.

Switching between levels for the gradient sampling was done by a 3-way solenoid valve, controlled by a datalogger (model CR-10, Campbell Scientific, Logan, Utah). The concentration was measured for 10 minutes at each level. The valves, sampling lines, and fittings were all Teflon to minimize absorption of ozone upstream of the monitor. The same length of tube was used for each intake, in order that the measured concentrations at each level would be equally affected by any absorption onto the sampling surfaces. Air was drawn continuously at 5 l/min

from both levels so that air was never stagnating in the sampling lines. The amount of error in the gradient measurement, introduced by this method of sampling, is discussed in Appendix B.

Temperature gradients, for use in flux-gradient calculations, were measured using two copper-Constantan thermocouples. Since the thermocouples were only referenced to datalogger temperature they cannot be trusted for the absolute temperature but should give the temperature difference very accurately (±0.05°C). Temperatures at both levels were also measured using thermistors (model CR101, Campbell Scientific,Logan, Utah). Both thermistors were calibrated against mercury in glass reference thermometers at the beginning of the field season. They were found to agree within better than 0.1°C.

Wind speed and direction were measured using a cup anemometer (model 014A, Met-One, Grants Pass, Oregon) and a wind vane anemometer (model 024A, Met-One, Grants Pass, Oregon). Wind direction measurements were primarily taken to ascertain the fetch for each sampling period. Wind speed measurements were required for the flux-gradient calculations. Error in the windspeed measurements is given as the greater of 0.1 ms^{-1} or 1.5%.

Atmospheric pressure and humidity were not measured at the field site. Values of dry and wet bulb temperature from Pitt Meadows weather station were used to calculate humidity at the field site. Atmospheric pressure at the field site was assumed to be identical to pressure at the weather station.

2.6 Meteorological conditions during the study

Because of the topographical situation of the region, namely its proximity to the sea and mountains, much of the area is subject to a diurnal cycle of surface winds, caused by the combined

Figure 2.6: Wind roses for the Pitt Meadows site from wind measurements on August 10-14, 27 and 30-31. (a) shows the diurnal measurements (0800-2000 PDT); and (b) shows the nocturnal measurements (2000-0800).

(a)

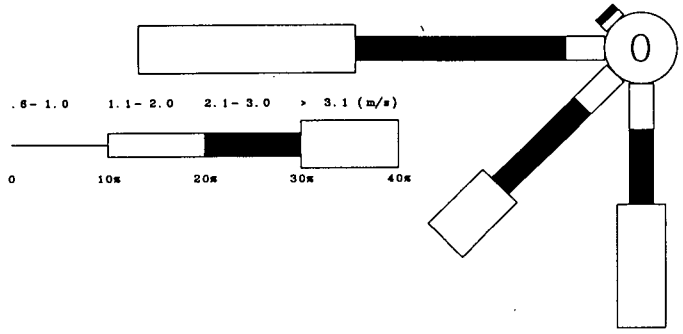

(b)

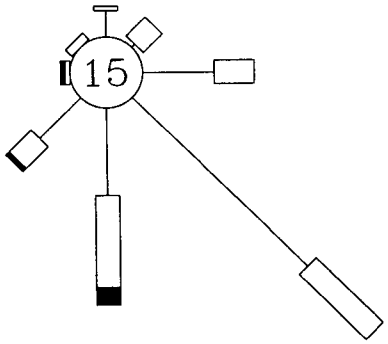

At this site observations of wind, during periods of clear weather showed a typical pattern of daytime winds from the southwest quadrant and night-time winds from a mix of directions, often including an easterly component (Figure 2.6). This general pattern has been observed at other sites in the area (Steyn and Faulkner, 1986; McKendry et al., 1996a). The flow in this particular part of the valley may be complicated by flows entering, or emerging from the nearby Pitt River valley, a major tributary valley that leads north from the main part of the LFV. Particularly well developed up-valley/down-valley circulation has been observed in this valley (McKendry et al., 1996a).

developed up-valley/down-valley circulations have been observed in this valley (McKendry et al., 1996a).

The diurnal cycle of wind speed at the site is fairly typical for a rural site during anticyclonic conditions. During the day, moderate wind speeds (2 - 5 ms^{-1}) were generally observed. During evening hours, wind speed dropped off sharply due to the combined effects of reduced mesoscale forcing and the development of a strong temperature inversion which isolated the lowest levels of the atmosphere.

Daily precipitation amounts, during July and August, from the Pitt Meadows automatic weather station are presented in Table 2.2. The month of July, 1994 began with a very heavy rainfall - 42 mm of rain fell on July 1st. Following that, only 3.3 mm of rain fell during the next 36 days. A total of 12.6 mm of rain fell at the site in the period from August 7th to 10th (immediately preceding the period during which measurements were taken). Following that, no rain fell until August 21. Between August 21st and 23rd a further 8 mm of rain fell. The next period of precipitation occurred between August 28th to 30th, when a further 10.2 mm of rain fell. The cumulative rainfall totals for the months of July and August were 42.2 mm and 30.9 mm respectively.

The corresponding average values for this site are 57.6 mm and 69.0 mm for July and August. Thus, in terms of precipitation amounts the summer was slightly drier than usual. The summer was also somewhat unusual in that very little rain fell during a five week period from the beginning of July until the second week in August. The long dry spell may have accounted for the presence of some brownish, senescent vegetation at the generally moist field site.

Table 2.2: Dates and amount of measurable rainfall recorded at the Pitt Meadows autostation during July and August, 1995

Date	Rainfall Amount (mm)	Cumulative Rainfall (mm)
July 1st	42.0	42.0
July 5th	0.2	42.2
July 17th	3.0	45.2
August 3rd	0.1	45.3
August 7th	3.6	48.9
August 8th	8.6	57.5
August 9th	0.2	57.7
August 10th	0.2	57.9
August 21st	7.2	65.1
August 22nd	0.6	65.7
August 23rd	0.2	65.9
August 28th	2.2	68.1
August 29th	7.8	75.9
August 30th	0.2	76.1

Field measurements were taken on hot, mainly sunny days, as this is when significant amounts of ozone are present in this area. The measurement periods during the full diurnal cycle were limited by the nature of the site. Only during the daytime and early evening hours were the winds typically from the southwest quadrant, from whence there was adequate fetch over a uniform surface.

2.7 Data acquisition and processing

Data from the sonic anemometer was continuously logged at 10 Hz onto an IBM compatible laptop computer (PC), using the SONIC software written by Jonathan Henkelmann for that purpose. Data from the ozone sonde was digitized at 10 Hz and also logged on the PC. The 10 Hz sampling rate was chosen as it roughly corresponded to the response time of the ozone sonde. The eddy correlation data were collected in blocks of 20 minutes to 2 hours length.

Ozone and temperature gradient data were collected as 10 minute averages on a CR-10 datalogger and downloaded to the PC at the end of each day of measurement. Mean wind speed and direction, and temperature at two levels were collected continuously at the site. They were logged as half hour averages on a CR-21 datalogger and downloaded to the PC several times during the field program.

A simple FORTRAN routine was used to convert each file of the turbulence data from binary to text format. Files were combined or subdivided to make blocks of close to 1/2 hour length where possible. All subsequent processing of the data was done using the S-Plus statistical and graphics language and the Excel spreadsheet program. Several of the S-Plus routines written and used for the data analysis are included in Appendix C.

Stationarity of the time series was tested using the non-parametric run test described by Bendat and Piersol (1986) and used by Roth (1988). This test is applied to a time series by subdividing it into blocks and calculating the variance of each block. The variance of each block is then compared to the median variance of all blocks. The number of runs of greater or lesser than median variance are counted and compared to the expectation number of runs from a random, stationary process. Time series that deviate too far from the expected number of runs are classified as nonstationary.

The test was applied to the time series of w, T, and 0_3 for each sampling period. Application of the test and results of the test are described in Appendix D. Periods that were found to be non-stationary were not rejected outright but were flagged for caution in during later analysis.

Sampling periods were classified according to the quality of fetch using wind direction measurements from the Met-One wind vane. Sampling periods were classified as having good, acceptable or poor fetch. Three samples were classified as having poor fetch and were rejected on that basis. The fetch classification is briefly discussed in Appendix D

The S-Plus routine ANALYSIS8.SP was used to calculate the means, covariances (fluxes), standard deviations and correlations from Reynolds decompositions of the turbulence data. The program also performed the detrending of the data using a linear least-squares regression. ANALYSIS8.SP also calculated the deposition velocity and the three components of resistance according to equations 1.8-1.12. The routine W89.SP was used to calculate the surface resistance according to the W89 parameterization.

Cospectra were calculated using the S-Plus routine COSPEC3.SP using the methods discussed in Chapter 4. Fluxes were calculated, using the cospectral method and a range of simulated instrument response times, using the COFLUX.SP routine. All these routines are presented in Appendix C.

3. RESULTS AND COMPARISON WITH W89

3.1 Time series of ozone, temperature and vertical velocity

Time series of vertical velocity, temperature and ozone concentration, as well as instantaneous kinematic fluxes of heat and ozone ($w'T'$ and $w'O_3'$) are presented in Figures 3.1 and 3.2. These time series were chosen to represent a range of atmospheric stability conditions. While these time series are not necessarily representative of all blocks during which data were collected, there are sufficient common characteristics to make a brief discussion of these time series useful. The data depicted on the graphs has been averaged in blocks of 10, to give roughly one point per second. This was done so that major features of the time series were not obscured by high frequency variations. The mean has been removed from the w, T and O_3 time series. The time series of ozone and temperature are plotted along with the linear least squares regression lines that were used to detrend them.

Data in Figure 3.1 were collected on August 30th, 1300-1330 (all times are Pacific Daylight Time, PDT), during clear, sunny conditions. The value of the stability parameter (z/L) at measurement height for this period was -0.2 representing strongly unstable conditions. The values for mean wind speed, friction velocity and sensible heat flux were 1.9 ms^{-1}, 0.36 ms^{-1} and 220 Wm^{-2}, respectively.

The temperature trace (Figure 3.1b) clearly shows the importance of large coherent structures with a duration of 2-3 minutes. These structures generally showed a fairly constant, lower than average temperature followed by a fairly sharp rise of 1 - 3°C. The temperature fluctuated rapidly around the higher temperature, before dropping off quickly to another quiescent cool period.

Figure 3.1: 30 minute time series traces of, (a) vertical velocity; (b) temperature; and (c) ozone concentration recorded on August 30th, 1300-1330. The temperature and ozone signals have had their mean removed and are plotted as deviations from the mean. The straight lines are the linear least squares lines that were used to detrend the time series.

(a)

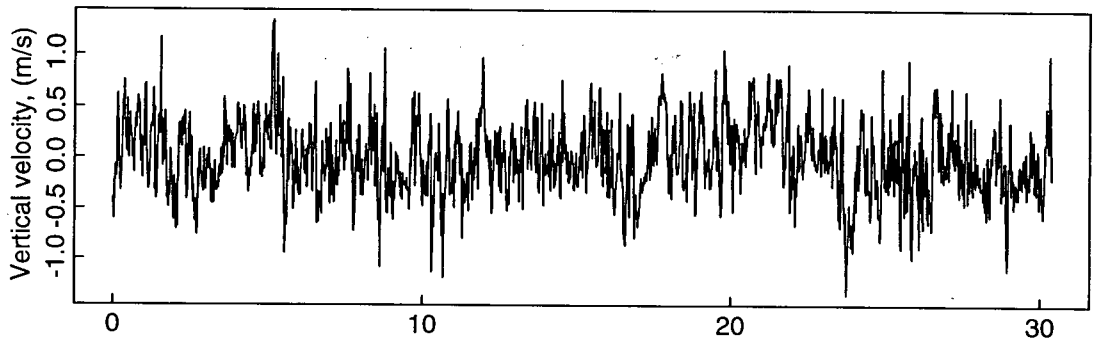

(b)

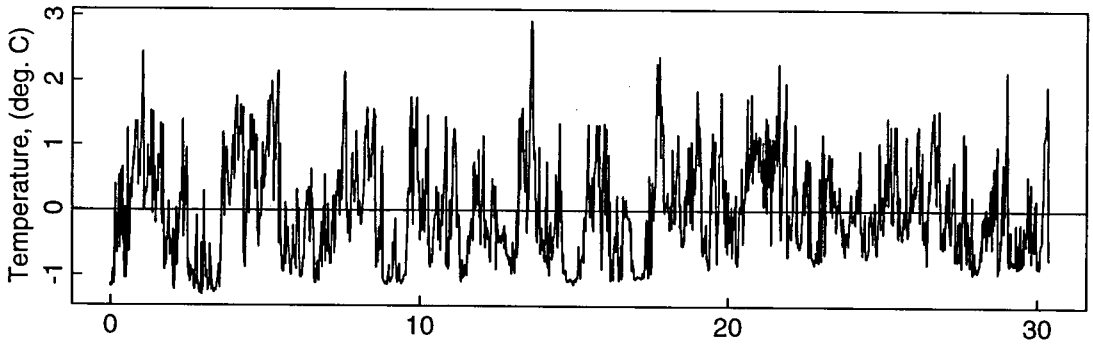

(c)

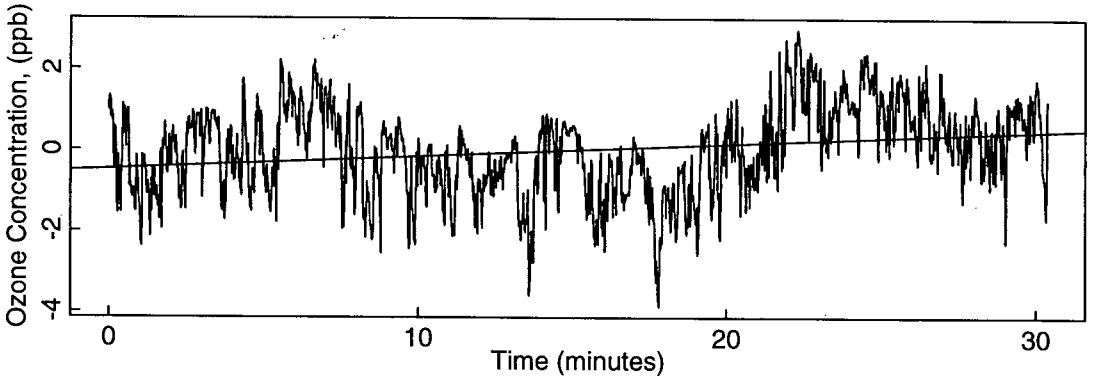

Figure 3.1: 30 minute time series traces of, (d) instantaneous kinematic ozone flux; and (e) instantaneous kinematic heat flux recorded on August 30th, 1300-1330.

(d)

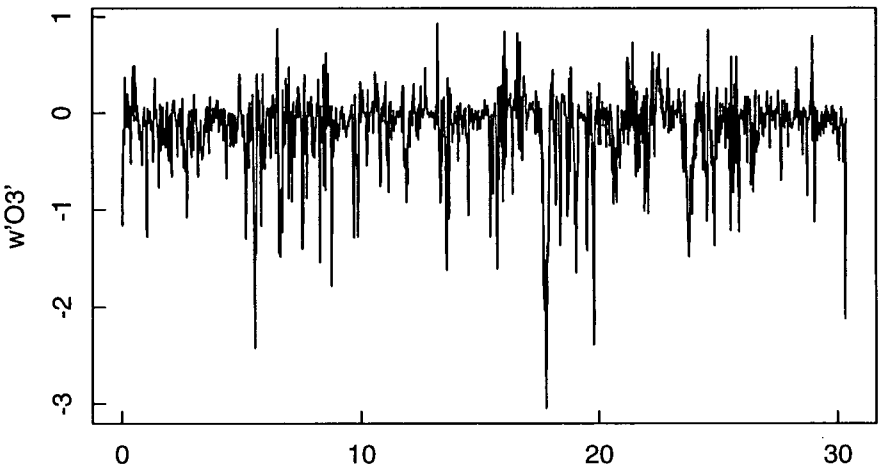

(e)

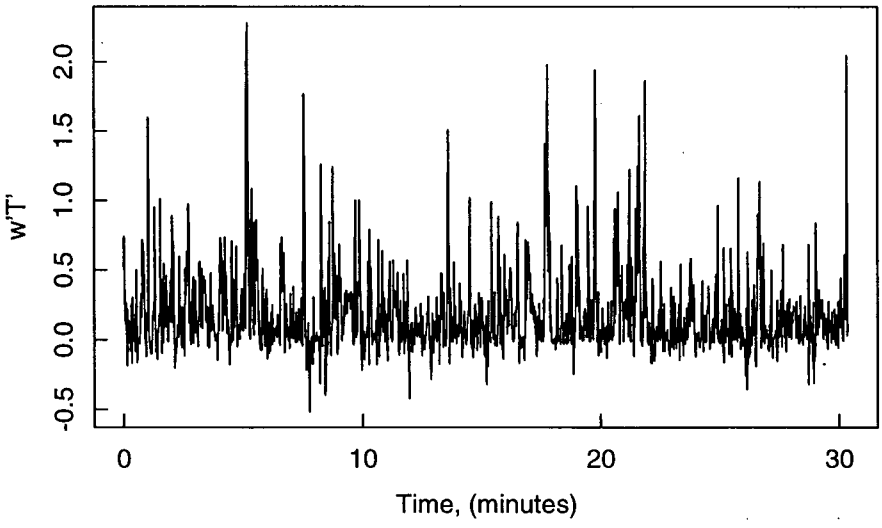

Ozone concentration fluctuations (Figure 3.1c) showed a very high degree of negative correlation with temperature fluctuations. On the figures, individual features of one second to several minutes duration in one series can usually be matched with similar features in the other suggesting that turbulent transport of the two quantities is done by the same eddies. This visible correlation is confirmed by the calculated value of r_{cT}, -0.6. Negative correlation between ozone and temperature variations is expected since ozone was being transported towards the surface, while temperature (heat) was being transported away from the surface.

Ozone concentration also underwent some variations on a time scale of roughly 10 minutes. These variations may not reflect turbulent processes, but rather advection, over the field site, of air with slightly different chemical properties.

Vertical velocity fluctuations (Figure 3.1a) generally showed less apparent structure than the temperature and ozone time series. Rapid, apparently random fluctuations from positive to negative velocities were observed, as would be expected in a turbulent field measured where vertical eddy dimension is constrained by proximity of the surface. Periods of higher than average vertical velocity variance generally corresponded to periods of elevated and rapidly fluctuating temperatures. Periods when the vertical velocity was quiescent often corresponded to periods when temperature was lower than average and not fluctuating strongly. The correlation coefficient for temperature and vertical velocity, r_{wT}, was 0.59. Ozone and vertical velocity were slightly less correlated - probably due to high frequency noise from the ozone sensor and low frequency variations in ozone concentration. r_{wc} was 0.43.

Heuristically, the features observed in the time series trace may be explained by reference to a qualitative model of boundary layer convective turbulence (Stull, 1988). In this model,

convective plumes extending throughout most of the boundary layer depth are separated by sheets of descending cooler air. From measurements taken just above the surface, (i.e. near the bottom of the boundary layer) warm, ozone-depleted updrafts appear less coherent than the cooler, ozone-rich downdrafts. This is expected, since at this level, small individual updrafts are just beginning to coalesce into coherent structures. Cool downdrafts, on the other hand, originate near the top of the boundary layer and therefore have had a greater length of time to mix internally and homogenize.

The simple picture described above is also complicated by the effect of mechanically generated (shear) turbulence. At z/L = -0.5 the contributions of wind shear and buoyancy to turbulent kinetic energy (TKE) production are roughly equal (Stull, 1988). At the measured value of z/L = -0.2, one would expect that over half of the TKE was generated by wind shear.

The instantaneous fluxes of ozone and heat are shown in Figures 3.1d and 3.1e. The intermittent nature of the fluxes, and hence the need for long averaging times to accurately measure the covariances, is well illustrated by these figures. Major flux carrying events were separated by periods with little net transfer.

There is a substantial degree of similarity between traces of ozone- and heat-fluxes. Individual peaks of heat and ozone transport can often be matched on the traces again suggesting a large degree of similarity in the turbulent transport of the two scalars.

Data in Figure 3.2 were recorded on August 11th, 1845-1915, during clear sunny conditions at the beginning of the evening cooling. The value of the stability parameter (z/L) for this period was 0.04, representing slightly stable conditions. The values for mean wind speed, friction velocity and sensible heat flux were 2.2 ms^{-1}, 0.27 ms^{-1} and -16 Wm^{-2}, respectively.

Figure 3.2: 30 minute time series traces of, (a) vertical velocity; (b) temperature; and (c) ozone concentration recorded on August 11th, 1845-1915. The temperature and ozone signals have had their means removed and are plotted as deviations from mean. The straight lines are the linear least squares lines that were used to detrend the time series.

(a)

(b)

(c)

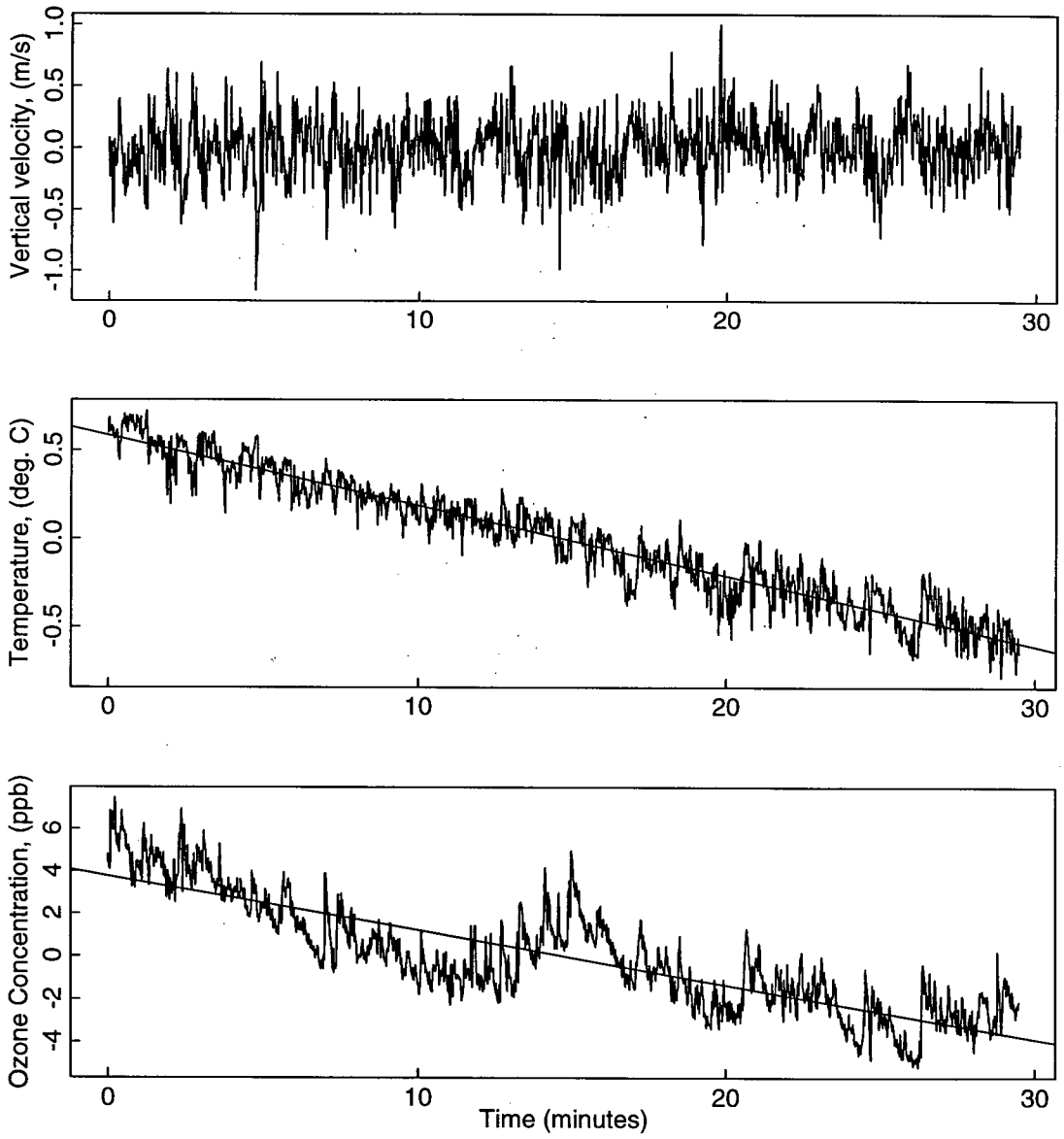

Figure 3.2: 30 minute time series traces of, (d) instantaneous kinematic ozone flux; and (e) instantaneous kinematic heat flux recorded on August 11th, 1845-1915.

(d)

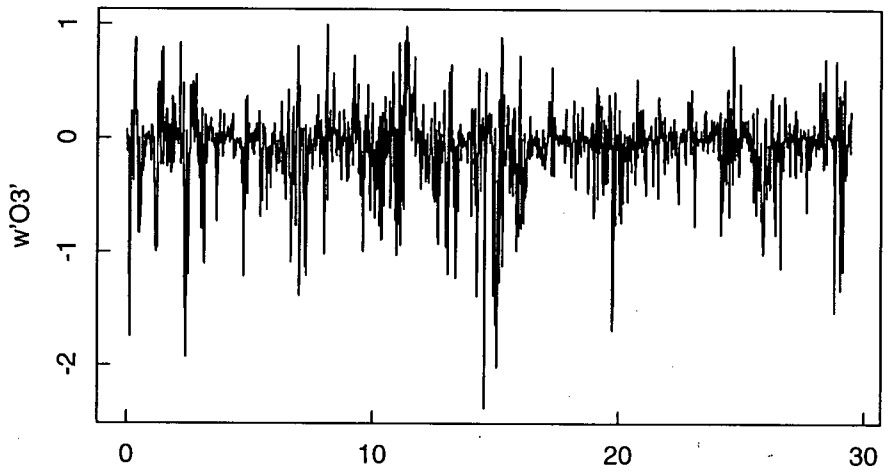

(e)

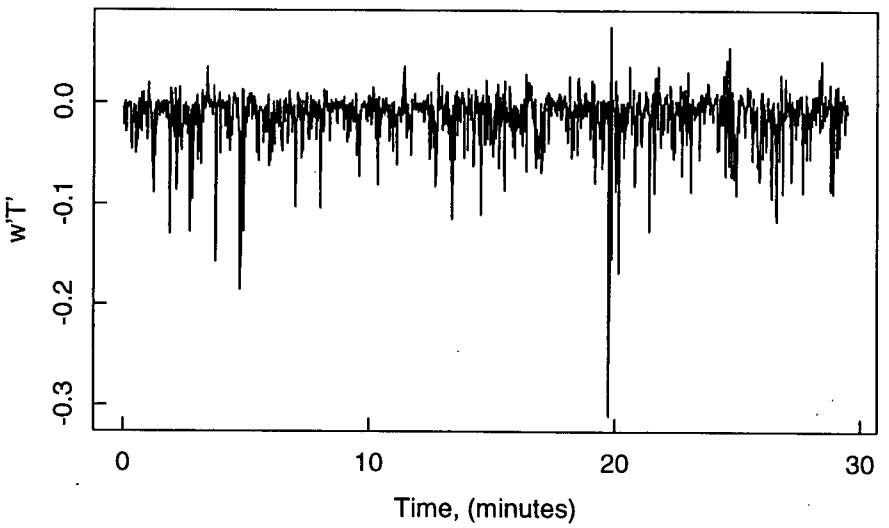

Temperature and ozone (Figures 3.2b and 3.2c) both showed significant nonstationarity of their means. Temperature had begun to decrease because of the reduction of solar heating. Ozone concentrations were decreasing rapidly due partly to reduction in photochemical production, but due mainly to reduced mixing in the boundary layer. As the nocturnal inversion began to form, near-surface ozone levels were depleted by deposition and were not replenished by mixing.

The eddy time scales in this case, as seen in the temperature and ozone traces, were about half as long as in the previous case. Given that the mean winds were similar in the two cases, this implies the dominant eddy scale was substantially smaller. This is expected (Kaimal and Finnigan, 1994) in a situation where the turbulence was primarily driven by shear production rather than buoyancy. The remains of large scale eddies, from previously vigorous mixing, may have been present in "fossil" form in the residual layer. This could possibly account for some of the larger scale fluctuation in ozone concentrations.

There was still a substantial degree of correlation between the ozone and temperature series (independent of the downward trend in both), though not so striking as in the previous case. r_{cT} for the detrended series was 0.4 during this period. Correlation was positive in this case since both quantities were being transported towards the surface.

TKE contained in the vertical velocity (Figure 3.2a) was about half that of the previous case. The respective vertical velocity variances, σ_w^2, were 0.15 m^2s^{-2} for the unstable case and 0.07 m^2s^{-2} for the stable case. The lack of buoyancy production in the stable case was only partly made up for by increased shear production from the slightly higher mean wind.

Instantaneous fluxes (Figures 3.2d and 3.2e) were less strongly correlated than in the previous case, presumably because both fluxes were smaller in magnitude, and less organized in direction. Nonetheless it is still possible to identify many simultaneous peaks of transport in the two series. There were significant instantaneous upward and downward fluxes of ozone although the net flux was downwards. Higher surface resistances at this time of day account for the weaker correlation between vertical velocity and ozone (r_{wc} was -0.25).

3.2 Measured ozone concentrations and ozone fluxes

Ozone fluxes were measured during a total of 72 sampling periods. Data during three of these periods were rejected because of poor fetch direction. The sampling periods were of roughly half hour duration. The duration of each sampling period is listed in Appendix F.

Table 3.1 lists values of ozone concentration, ozone flux, ozone deposition velocity, heat flux, friction velocity, stability parameter, mean wind speed, standard deviation of vertical velocity, temperature, and ozone concentration, and the correlation coefficients between vertical velocity, temperature and ozone for each time period. The times given are the beginning of data collection periods in all cases. Times are given in Pacific Standard Time (PST), which is equal to GMT plus nine hours. The usual convention is followed with respect to sign of the fluxes - negative values represent fluxes toward the surface; positive values represent upward fluxes. Since no systematic differences in fluxes were noted among those measurement periods identified as having non-stationarities in the variance (Appendix D.1), those data were not considered separately or rejected.

Table 3.1: Measured values of ozone concentration, ozone flux, deposition velocity, heat flux, friction velocity, stability parameter, mean wind speed; standard deviations of vertical velocity, temperature and ozone; and correlation coefficients between vertical velocity, temperature and ozone.

Date (Aug. 94)	Time (PDT)	Ozone Conc. (ppb)	Corrected Ozone Flux ($\mu gm^{-2}s^{-1}$)	v_d (cms^{-1})	Heat Flux (Wm^{-2})	u_* (ms^{-1})	(z/L)	Mean Wind Speed (ms^{-1})	σ_w (ms^{-1})	σ_T (°C)	σ_c (ppb)	r_{wT}	r_{wc}	r_{cT}
10	1625	24.3	-0.346	-0.74	117	0.34	-0.127	3.0	0.40	0.47	1.33	0.53	-0.33	-0.58
10	1657	23.4	-0.245	-0.54	70	0.27	-0.143	3.1	0.39	0.36	0.87	0.42	-0.35	-0.77
11	1522	38.0	-0.368	-0.50	91	0.31	-0.123	2.7	0.37	0.57	1.63	0.37	-0.31	-0.50
11	1558	42.6	-0.438	-0.53	91	0.37	-0.075	3.2	0.41	0.47	1.20	0.40	-0.43	-0.77
11	1629	44.0	-0.429	-0.51	63	0.33	-0.076	3.1	0.40	0.40	1.15	0.34	-0.43	-0.74
11	1745	45.2	-0.333	-0.38	6	0.24	-0.017	2.2	0.28	0.18	1.58	0.09	-0.35	-0.49
11	1817	39.9	-0.205	-0.27	-15	0.27	0.033	2.3	0.29	0.12	2.58	-0.36	-0.13	0.12
11	1848	23.2	-0.212	-0.47	-16	0.27	0.036	2.2	0.28	0.13	1.41	-0.38	-0.25	0.40
12	1641	46.2	-0.364	-0.41	105	0.39	-0.075	3.0	0.37	0.46	1.25	0.52	-0.38	-0.70
12	1712	46.1	-0.393	-0.44	91	0.35	-0.092	2.8	0.34	0.41	1.38	0.55	-0.41	-0.68
12	1743	46.4	-0.289	-0.32	42	0.25	-0.120	2.5	0.28	0.28	1.36	0.46	-0.36	-0.69
12	1813	47.0	-0.282	-0.31	35	0.27	-0.072	2.6	0.28	0.21	1.11	0.50	-0.43	-0.75
13	1234	47.2	-0.521	-0.57	220	0.33	-0.256	2.2	0.40	0.76	1.19	0.60	-0.54	-0.78
13	1315	50.0	-0.446	-0.46	184	0.30	-0.299	2.1	0.39	0.78	1.41	0.51	-0.40	-0.73
13	1348	48.2	-0.433	-0.46	188	0.35	-0.183	2.6	0.42	0.81	1.24	0.46	-0.41	-0.84
13	1420	50.4	-0.455	-0.47	183	0.34	-0.194	2.7	0.41	0.79	1.15	0.47	-0.46	-0.84
13	1451	53.2	-0.428	-0.42	179	0.32	-0.233	2.8	0.41	0.75	1.09	0.49	-0.47	-0.80
13	1521	55.7	-0.364	-0.34	134	0.32	-0.179	2.5	0.38	0.72	1.12	0.42	-0.42	-0.82
13	1553	57.2	-0.476	-0.43	132	0.41	-0.080	3.0	0.40	0.61	1.19	0.46	-0.50	-0.79
13	1624	57.9	-0.430	-0.38	100	0.35	-0.102	2.7	0.35	0.54	1.19	0.44	-0.51	-0.78
13	1655	58.7	-0.392	-0.34	87	0.37	-0.071	3.1	0.37	0.45	1.23	0.44	-0.43	-0.78
13	1726	54.2	-0.343	-0.33	61	0.33	-0.071	3.0	0.34	0.37	1.23	0.42	-0.41	-0.69
13	1759	50.2	-0.370	-0.38	49	0.34	-0.051	2.9	0.33	0.27	1.31	0.47	-0.42	-0.64
14	1120	29.1	-0.312	-0.55	197	0.27	-0.426	1.8	0.36	0.74	0.79	0.62	-0.53	-0.75
14	1150	28.2	-0.335	-0.61	236	0.32	-0.296	2.4	0.41	0.82	0.97	0.58	-0.40	-0.61
14	1222	26.1	-0.262	-0.51	210	0.31	-0.291	3.3	0.40	0.77	0.75	0.57	-0.41	-0.60
14	1253	25.7	-0.270	-0.54	243	0.37	-0.205	2.9	0.41	0.80	0.70	0.63	-0.45	-0.71
14	1325	26.1	-0.234	-0.46	216	0.37	-0.181	3.5	0.43	0.78	0.67	0.54	-0.38	-0.65
14	1357	27.2	-0.217	-0.41	155	0.34	-0.170	3.4	0.41	0.59	0.62	0.53	-0.39	-0.62
14	1427	29.8	-0.265	-0.45	173	0.30	-0.275	2.9	0.38	0.66	0.79	0.58	-0.42	-0.57
14	1459	33.3	-0.328	-0.50	194	0.28	-0.374	2.4	0.36	0.69	0.91	0.65	-0.49	-0.67
14	1530	37.3	-0.335	-0.46	77	0.24	-0.244	2.2	0.34	0.39	1.72	0.50	-0.28	-0.34
14	1600	30.8	-0.264	-0.44	34	0.27	-0.072	2.6	0.32	0.29	1.21	0.31	-0.33	-0.59
14	1630	27.3	-0.390	-0.73	40	0.28	-0.081	2.4	0.31	0.30	2.68	0.36	-0.23	0.05
27	1259	35.6	-0.385	-0.56	164	0.28	-0.332	1.8	0.36	0.70	1.12	0.54	-0.47	-0.63

Table 3.1: continued

Date (Aug. 94)	Time (PDT)	Ozone Conc. (ppb)	Corrected Ozone Flux ($\mu gm^{-2}s^{-1}$)	v_d (cms^{-1})	Heat Flux (Wm^{-2})	u_* (ms^{-1})	(z/L)	Mean Wind Speed (ms^{-1})	σ_w (ms^{-1})	σ_T (°C)	σ_c (ppb)	r_{wT}	r_{wc}	r_{cT}
27	1424	39.9	-0.199	-0.26	146	0.18	-1.119	1.6	0.35	0.60	0.88	0.60	-0.33	-0.46
27	1446	40.1	-0.190	-0.25	113	0.27	-0.254	2.2	0.33	0.63	1.55	0.46	-0.19	-0.18
27	1515	42.6	-0.204	-0.25	100	0.22	-0.388	1.4	0.35	0.56	0.68	0.45	-0.45	-0.66
27	1545	44.0	-0.324	-0.38	104	0.27	-0.224	1.8	0.34	0.56	1.04	0.47	-0.46	-0.64
27	1645	48.9	-0.206	-0.22	36	0.26	-0.086	1.4	0.26	0.30	1.15	0.40	-0.35	-0.55
27	1715	43.6	-0.282	-0.34	16	0.35	-0.017	3.1	0.36	0.24	2.12	0.17	-0.18	-0.45
27	1745	28.0	-0.246	-0.45	-14	0.42	0.008	3.5	0.42	0.14	1.15	-0.20	-0.24	-0.26
27	1815	20.4	-0.117	-0.30	-35	0.33	0.042	2.7	0.36	0.21	0.72	-0.41	-0.21	0.56
27	1846	18.3	-0.065	-0.18	-34	0.28	0.062	2.2	0.29	0.23	1.71	-0.42	-0.06	0.26
27	1902	18.4	-0.069	-0.19	-20	0.20	0.107	2.0	0.23	0.25	1.08	-0.28	-0.13	0.51
27	1934	18.3	-0.054	-0.15	-9	0.11	0.320	0.9	0.15	0.31	2.09	-0.18	-0.08	0.15
30	1151	27.1	-0.441	-0.83	217	0.31	-0.301	2.2	0.40	0.83	1.13	0.55	-0.47	-0.76
30	1221	28.5	-0.409	-0.73	198	0.30	-0.295	2.4	0.39	0.80	1.29	0.54	-0.40	-0.54
30	1301	32.1	-0.359	-0.57	219	0.36	-0.204	1.9	0.38	0.81	1.09	0.59	-0.42	-0.60
30	1332	33.3	-0.387	-0.59	242	0.22	-0.911	1.6	0.37	0.84	0.90	0.66	-0.59	-0.80
30	1408	35.1	-0.366	-0.53	172	0.30	-0.254	2.1	0.39	0.70	1.00	0.52	-0.45	-0.77
30	1449	36.0	-0.335	-0.48	136	0.29	-0.227	2.6	0.37	0.61	1.03	0.51	-0.42	-0.73
30	1519	39.6	-0.404	-0.52	147	0.26	-0.335	2.5	0.38	0.59	1.27	0.55	-0.40	-0.67
30	1550	42.5	-0.415	-0.50	129	0.31	-0.183	2.5	0.35	0.57	1.33	0.54	-0.43	-0.70
30	1620	43.3	-0.395	-0.47	114	0.32	-0.148	2.4	0.36	0.49	1.29	0.55	-0.42	-0.76
30	1651	43.8	-0.358	-0.42	79	0.25	-0.210	2.2	0.31	0.40	1.30	0.53	-0.43	-0.84
30	1721	41.5	-0.274	-0.34	53	0.23	-0.181	1.9	0.26	0.31	1.17	0.54	-0.43	-0.70
30	1751	38.7	-0.253	-0.34	24	0.20	-0.132	1.9	0.23	0.20	1.53	0.44	-0.34	-0.69
30	1821	36.3	-0.119	-0.17	0	0.13	0.001	1.2	0.17	0.14	1.31	0.00	-0.25	0.15
30	1853	22.6	-0.042	-0.09	-3	0.09	0.18	0.8	0.09	0.17	1.04	-0.18	-0.19	0.64
31	1150	21.7	-0.262	-0.61	183	0.26	-0.441	1.4	0.34	0.71	1.23	0.63	-0.31	-0.46
31	1220	21.0	-0.363	-0.88	218	0.22	-0.828	1.6	0.38	0.81	1.09	0.60	-0.43	-0.58
31	1250	22.5	-0.354	-0.80	205	0.31	-0.278	2.2	0.38	0.77	0.91	0.58	-0.50	-0.77
31	1320	25.3	-0.334	-0.67	138	0.27	-0.299	2.1	0.36	0.66	1.09	0.49	-0.41	-0.50
31	1350	25.1	-0.353	-0.72	83	0.35	-0.083	2.9	0.38	0.35	0.95	0.52	-0.48	-0.79
31	1351	25.6	-0.274	-0.55	158	0.36	-0.137	2.8	0.41	0.68	2.16	0.48	-0.15	0.02
31	1421	27.9	-0.321	-0.59	207	0.33	-0.245	2.9	0.40	0.78	1.61	0.56	-0.24	-0.37
31	1453	32.5	-0.195	-0.31	131	0.34	-0.141	2.9	0.37	0.62	2.06	0.48	-0.12	-0.26
31	1523	28.1	-0.387	-0.70	109	0.37	-0.094	3.0	0.39	0.45	2.40	0.52	-0.20	-0.21

Mean ozone concentrations observed at the site, during the eight days on which measurements were taken, are shown in Figure 3.3. Ozone concentrations typically rose through the morning and early afternoon hours to a maximum value of around 40 ppb in the mid to late afternoon. Concentrations were often stable at near maximum values for several hours, before dropping off quite rapidly in the evening hours to values below 20 ppb.

The rise in the morning may be attributed to both advection and in situ photochemical production. The rapid falloff in the evening occurred as light levels were decreasing, slowing photochemical production. Reduced mixing in the boundary layer allowed surface deposition, and possibly some chemical consumption from local sources of NO_x, to rapidly deplete ozone in the surface-layer.

Ozone concentrations observed throughout the measurement period showed wide variation around this average pattern. The peak ozone concentration was nearly 60 ppb on August 13. Late in the evening on August 30th, a minimum concentration of 14 ppb was observed. Variations in maximum concentrations from day to day resulted from a wide variety of local and mesoscale influences, such as air temperature, boundary layer height, wind strength, wind direction and the previous day's ozone concentration (Robeson and Steyn, 1990).

The average diurnal course of the ozone flux is shown in Figure 3.4. The average value of the ozone flux through the afternoon was about 0.35 $\mu gm^{-2}s^{-1}$. After 1800 hours ozone flux decreased rapidly to near zero values.

The average course of ozone flux may be broadly explained in the following manner. Through the afternoons ozone concentrations increased - tending to increase the downward flux of ozone. However, at the same time surface resistance was also increasing - acting to reduce the

downward flux. Together, these two factors accounted for the relatively constant ozone flux through the afternoon and early evening.

Around 1800 hours the ozone concentrations were generally decreasing rapidly. The surface resistance, laminar boundary layer resistance and atmospheric resistance were all increasing rapidly. These two factors acting in concert, caused the observed rapid decrease in ozone flux.

The major source of uncertainty in individual flux measurements was statistical uncertainty of the covariance estimate, $\overline{w'O_3'}$, due to the finite length of the sampling period. The expected error in the covariance estimate is given by Equation 2.2. Statistical uncertainty was greatest during periods of weak mean wind, as this increased the integral time scale (basically fewer eddies were advected past the sensors by weaker mean winds); and during periods when the surface resistance was high, as this tended to decrease r_{wc}. Uncorrelated noise from the ozone sensor made a further contribution to the uncertainty (Lenschow and Kristensen, 1985). This contribution was most significant when ozone concentration was low, and the flux weak.

Experimental values of r_{wc} were used in Equation 2.2, thereby including the effect of uncorrelated noise on the error estimate through its effect on reducing the correlation coefficient. An empirical formula (Equation 2.3) was used to estimate the integral time scale.

Statistical uncertainty for the majority of the flux measurements was found to be in the range of 7 - 15%. A few evening measurements had uncertainties approaching 30% due partly to weaker winds, but mainly to the much weaker correlation between ozone concentration and vertical velocity.

Figure 3.3: Mean ozone concentration (from the ML9811 ozone monitor) during eight measurement days. Error bars are the standard error of the mean.

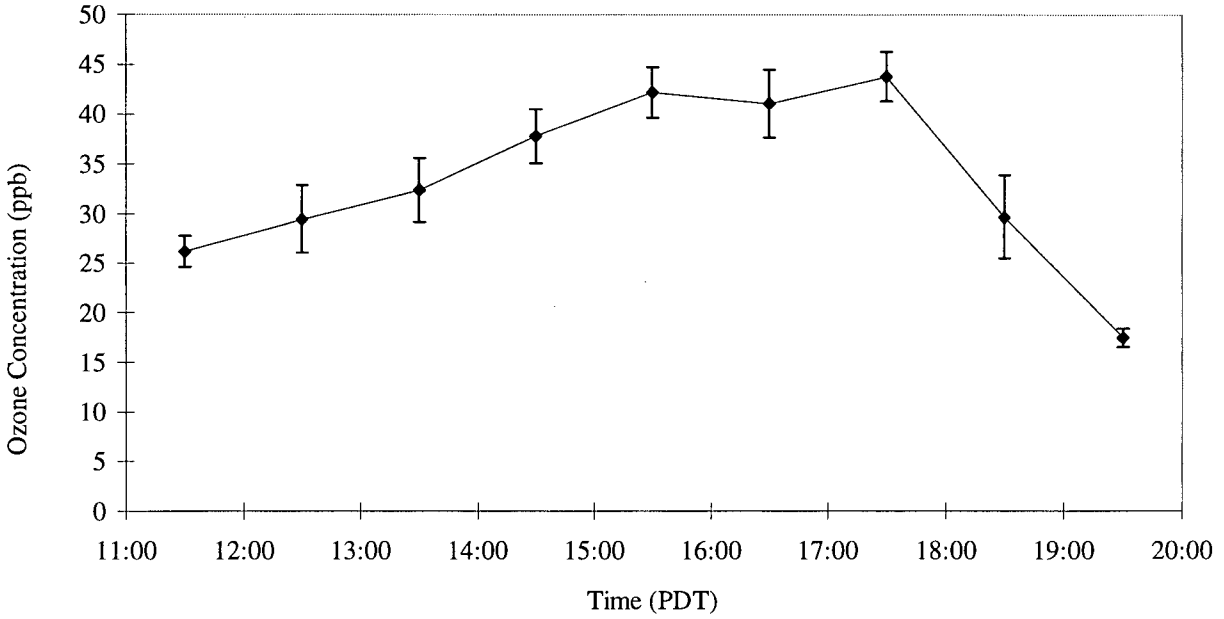

Figure 3.4: Mean diurnal course of downward ozone flux at Pitt Meadows site. Error bars are the standard error of the mean.

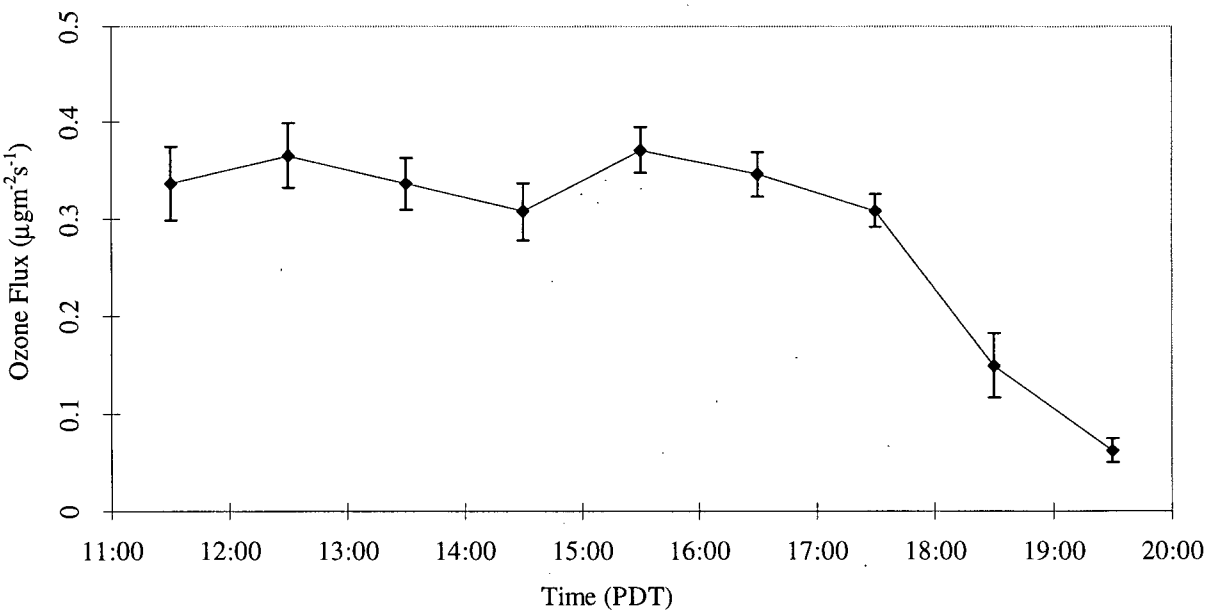

A further source of error in the flux measurements came from uncertainty in the calibration of the ozone sensor (as discussed in Appendix B). It was estimated that this may have added an additional 5% uncertainty, independent of the statistical uncertainty. Additional uncertainty contributed by inaccuracy of the sonic anemometer was negligible. Mean vertical velocity was very close to zero, so errors contributed by anemometer tilt were also likely quite small. Thus, the total uncertainty for the flux measurements was in the range of 10-20%, except for a few cases during the evening hours which had considerably larger errors.

August 13th, the day with the highest ozone concentrations, also had the highest observed values of ozone flux. Ozone fluxes of just over 0.5 $\mu gm^{-2}s^{-1}$, during a period when the mean concentration was 55 ppb, were observed on this day. Surface removal at this rate corresponds to a decrease in ozone of 1.5 ppb/hr, averaged over a 600 m deep boundary layer.

This rate of removal corresponds quite closely (when scaled by the difference in mean concentration between the two days) with the value calculated by McKendry et al. (1996a) for August 5th, 1993, during the Pacific 93 field program. This suggests that the single value of surface resistance, 160 sm^{-1}, that they used, is a valid approximation, at least over grassland surfaces in the LFV. McKendry et al. (1996a) calculated a surface removal rate on August 5th of 2.9 ppb/hr averaged over a 600 m thick layer with an average ozone concentration of 100 ppb. On the same day photochemical ozone production exceeded 17 ppb/hr in the Pitt Lake tributary valley, during the early afternoon (McKendry et al., 1996a). Thus, under suitable conditions, photochemical production is the dominant term in the budget equation (Equation 1.5) for ozone.

During the same episode, McKendry et al. (1996b) reported ozone levels at Harris Road on August 6th increasing at 9.5 ppb/hr in the early hours of the morning and at 3-5 ppb/hr during

the day. Results from their transilient model indicated that a large portion of this might be due to down mixing of elevated layers of ozone rich air.

Integrated surface removal on August 13th between 1230 and 1830 corresponds to a total drawdown of 8.6 ppb over that 6 hour period, assuming a 600 m deep boundary layer.

The assumption of a 600 meter deep boundary layer is not unrealistic in the LFV. Large scale subsidence during anticyclonic conditions tends to suppress the mixed layer depths. Advection of stable air by the sea breeze also suppresses mixing depth (Steyn and Oke, 1982).

3.3 Measured values of surface resistance

Deposition velocities and resistances to ozone deposition were calculated for each half hour period, from the measured fluxes, using Equations 1.8-1.12. Results are presented in Table 3.1 (deposition velocities) and Table 3.2 (resistances).

Figures 3.5 and 3.6 show the measurements of surface resistance in graphical form. The measurements generally showed the lowest resistances in the late morning hours when the earliest measurements were taken. Throughout the day there was a gradual rise in surface resistance. A sharp rise in surface resistance around sunset was observed both days on which measurements were taken during that part of the diurnal cycle.

The diurnal course of surface resistance presented in Figures 3.5 and 3.6 agree in a qualitative sense with the idealized diurnal course of surface resistance, presented in Figure 1.3. Some care, however, is warranted in the interpretation of Figure 3.6. Since the measurement periods were different on each of the eight days, each point on Figure 3.6 represents an average

Table 3.2: Measured total resistance and calculated component resistances for all sampling periods.

Date	Time (PDT)	Total Resistance ($s \bullet m^{-1}$)	Atmospheric Resistance ($s \bullet m^{-1}$)	Laminar Boundary-Layer Resistance ($s \bullet m^{-1}$)	Surface Resistance ($s \bullet m^{-1}$)
10	1625	136	20	21	95
10	1657	185	24	24	137
11	1522	199	22	22	155
11	1558	188	19	20	149
11	1629	198	22	22	154
11	1745	262	33	26	203
11	1817	377	32	24	321
11	1848	212	33	25	154
12	1641	247	19	19	209
12	1712	228	20	21	187
12	1743	313	28	26	259
12	1813	325	27	24	274
13	1234	176	18	21	137
13	1315	218	19	23	176
13	1348	216	18	21	177
13	1420	215	18	21	176
13	1451	241	19	22	200
13	1521	296	20	22	254
13	1553	232	17	18	197
13	1624	261	20	21	220
13	1655	290	20	20	250
13	1726	306	22	21	263
13	1759	264	22	21	221
14	1120	183	19	25	139
14	1150	165	18	22	125
14	1222	195	18	22	155
14	1253	187	17	20	150
14	1325	218	17	20	181
14	1357	245	19	21	205
14	1427	220	19	23	178
14	1459	198	19	24	155
14	1530	218	25	27	166
14	1600	228	27	24	177
14	1630	137	26	24	87
27	1259	179	20	24	135
27	1424	385	19	32	334
27	1446	405	22	25	358
27	1515	401	24	28	349
27	1545	261	22	24	215
27	1645	454	27	25	402
27	1715	297	24	21	252
27	1745	220	20	18	182
27	1815	339	27	22	290
27	1846	546	32	24	490

Table 3.2: continued

Date	Time (PDT)	Total Resistance ($s \bullet m^{-1}$)	Atmospheric Resistance ($s \bullet m^{-1}$)	Laminar Boundary-Layer Resistance ($s \bullet m^{-1}$)	Surface Resistance ($s \bullet m^{-1}$)
27	1902	517	49	30	438
27	1934	663	114	45	504
30	1151	121	18	22	81
30	1221	137	19	23	95
30	1301	175	17	20	138
30	1332	169	17	28	124
30	1408	188	19	23	146
30	1449	210	21	23	166
30	1519	192	21	25	146
30	1550	200	20	22	158
30	1620	214	21	22	171
30	1651	239	24	26	189
30	1721	296	27	27	242
30	1751	298	34	30	234
30	1821	595	65	40	490
30	1853	1057	113	50	894
31	1150	163	19	25	119
31	1220	114	18	28	68
31	1250	125	18	22	85
31	1320	149	21	24	104
31	1350	140	21	21	98
31	1351	183	18	20	145
31	1421	170	18	21	131
31	1453	326	20	21	285
31	1523	142	19	20	103

over a different ensemble of days, and thus over different meteorological conditions. Nonetheless, the general pattern depicted in Figure 3.6 was seen on most individual days as well.

Average daytime (1100 -1800 hours) surface resistance measured at the Pitt Meadows site was 175 sm^{-1}. This is in reasonable agreement with values measured during several previous studies of ozone deposition to grassland. Measurements by Colbeck and Harrison (1985) over grassland, during late summer, found surface resistances to average 150 sm^{-1} during the afternoon. Their minimum resistances were similar to those measured at Pitt Meadows but their

Figure 3.5: Surface resistance to ozone deposition measured on eight days in August 1994.

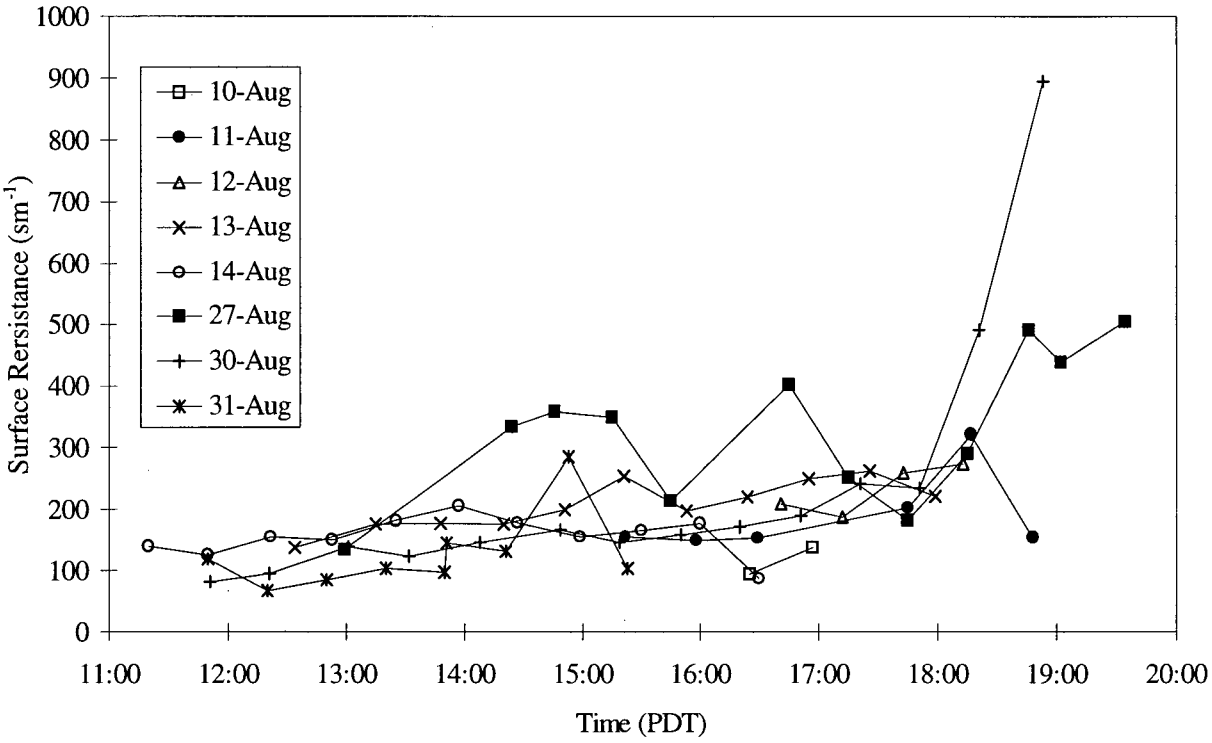

Figure 3.6: Average diurnal course of surface resistance to ozone deposition. Error bars represent the standard error of the mean.

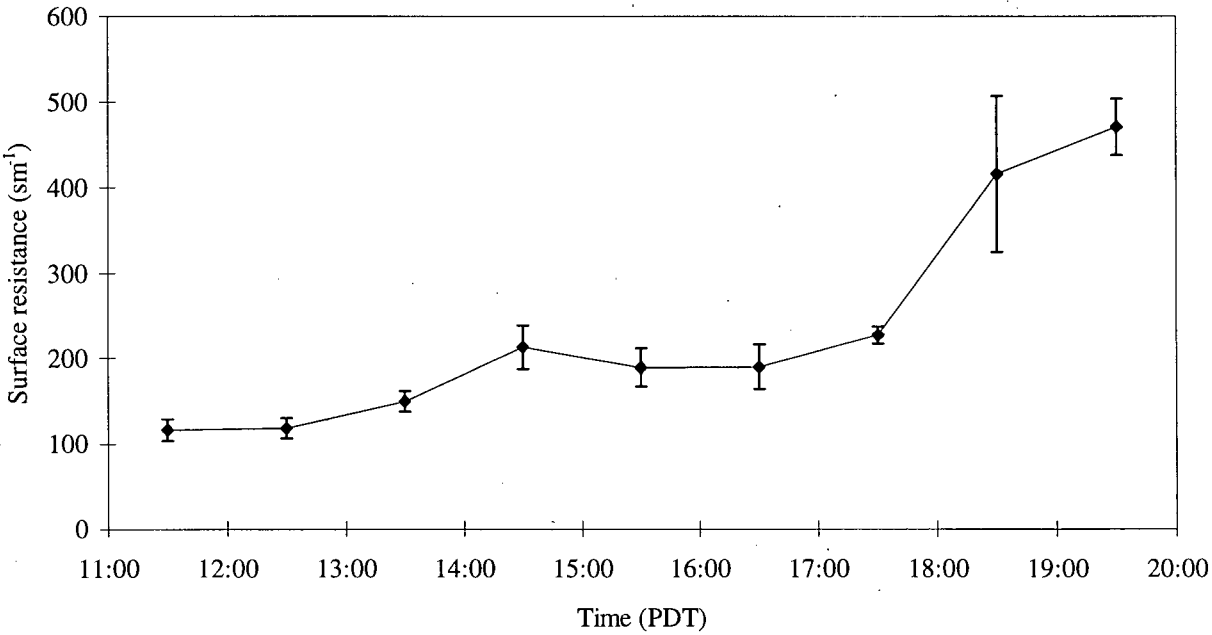

measurements did not show as consistent a rise in surface resistance through the afternoon hours as was observed at Pitt Meadows.

Measurements by Stocker et al. (1993) over a much drier grassland site found substantially higher surface resistances. They measured a median daytime surface resistance of 265 sm^{-1}. They attributed the high minimum values of r_c to water stress. Despite the higher daytime values of r_c the diurnal pattern observed by Stocker et al. was very similar to that seen at Pitt Meadows.

3.3.1 Measurement uncertainty

Uncertainty in individual measurements of surface resistance was estimated to range between 15 and 25%, for the most part. Some evening measurements had significantly higher uncertainty. The main contribution to this error was from statistical uncertainty in the estimate of the covariance, $\overline{w'O_3'}$. Additional contributions to the uncertainty resulted from errors in estimates of r_a and r_b, since these were subtracted from the total resistance to calculate the surface resistance. However, r_a and r_b together contributed at most 40% of the total resistance (Table 3.2). In most cases they contributed only 10 to 25% of the total resistance. Therefore, measured surface resistances are relatively insensitive to errors or biases in the parameterization of r_a and r_b. Measurement of mean ozone concentration was accurate to within 5% over the measurement period and therefore contributed a small amount to the total error.

Uncertainty in the atmospheric resistances was likely fairly substantial. Statistical uncertainty in the heat flux and especially the friction velocity led to errors in the calculated values of L. The formulas that relate z/L to the atmospheric resistance are themselves empirical

approximations accurate only to within 10 or 20% (Wyngaard, 1990). The net effect is an estimated uncertainty in these values of 20%.

Uncertainty in estimates of r_b is difficult to quantify. There is a substantial contribution due to uncertainty in the measured value of u_*. However, the form of the parameterization itself is likely the major source of uncertainty for r_b. The ratio z_0/z_C will vary between different surfaces, and could even change over time for a given canopy, as physiological changes in the canopy affect the level at which the greatest ozone absorption will occur.

3.3.2 Chemical reactions

When the flux of a substance such as ozone is measured in the surface-layer, the measured flux will equal the surface flux, only if there are no significant sources or sinks for the substance between measurement height and the surface. For many substances, the assumption of no sources or sinks in the surface-layer is a very good one. However, in the case of ozone, the reactions with nitrogen oxides (Equations 1.1-1.3) are very rapid, and may therefore act as a source or sink for ozone in the surface-layer.

The importance of gas-phase reactions, compared to turbulent processes, depends on their relative time scales. The time scale for mixing in the surface layer is given by z/ku_* (Lenschow and Delany, 1987). In the present study, u_* was mostly between 0.2 and 0.4 ms^{-1}; measurement height was roughly 4 m. Therefore the mixing time scale was between 25 and 50 s. The time scale for the O_3-NO-NO_2 photochemical triad, determined from their rate constants is typically 100 s in the boundary layer (Neubert et al., 1993) - so chemical reactions may be important.

Both NO and NO_2 can be either emitted at the surface or deposited at the surface, depending on atmospheric concentrations and soil processes (Delany et al., 1986). Emission of NO from the surface consumes ozone in the lowest layers of the atmosphere, and would therefore enhance the measured flux of ozone above the actual deposition flux. Emission of NO_2 would have the opposite effect, causing an underestimate of deposition flux.

Measurements of NO_x fluxes by a number of different investigators have produced a wide range of results (Stocker et al., 1993). The direction and magnitude of NO_x fluxes depends on atmospheric concentrations of NO_x, as well as a wide range of soil variables such as soil moisture, soil nitrogen content and soil type.

Measurements of NO and NO_2 concentration were not taken at the site but were available from the GVRD monitor, situated 1 km from the field site. Through the measurement period, NO concentrations ranged between 1 to 20% of ozone concentrations. NO_2 concentrations were higher, typically 5 - 30% of ozone concentrations. However, during some evening periods NO_2 concentrations were as high or higher than ozone concentrations. The observed concentrations were substantially above background levels, which are typically a few ppb in unpolluted tropospheric air. Given the elevated concentrations of NO_x, some net deposition at the site seems most likely.

At low NO_x concentrations, the deposition of ozone was likely little affected by chemical reactions. Even at fairly substantial NO_x concentrations ($[NO_2] / [O_3] = .5$) the constant flux assumption still holds up to 4 m (Fitzjarrald and Lenschow, 1983), which was the measurement height used in this study. On this basis one can conclude that, with the exception of a few evening

periods, the measured ozone deposition parameters were not greatly affected by chemical reactions with NO_x.

3.3.3 Variability of surface resistance

Within the diurnal trend of surface resistance described above, there is significant variation on most days, as well as significant differences between days. Some portion of the variability is due simply to measurement uncertainty. However, a substantial portion of the variation may be explained with reference to the micrometeorological factors that control surface resistance.

Since uptake in stomata is usually the major pathway for ozone deposition (Wesely et al., 1978), the main factors that control surface resistance are those that affect stomatal resistance. Of the components of bulk canopy resistance, stomatal resistance is the most variable, and most sensitive to micrometeorological variables. Baldocchi et al. (1987) list four main factors that control stomatal resistance. They are: (1) the amount of photosynthetically active radiation (PAR), (2) temperature, (3) leaf water potential, and (4) vapour density deficit of the surrounding air. Carbon dioxide levels within the leaves could also be added to this list (Mansfield et al., 1981).

Stomatal resistance decreases with increasing PAR. At low light levels, the decrease is quite rapid. At higher light levels, saturation is reached, further increases of PAR decrease the stomatal resistance only slightly (Jarvis and Morrison, 1981). The effect of PAR on stomatal resistance is the primary factor causing the diurnal cycle of surface resistance (Figure 1.3). Its effect is shown quite clearly in surface resistance measurements taken during this study (Figures 3.5 and 3.6).

Leaf water potential is a measure of plant water stress. It is largely a function of root zone soil moisture. Moisture in the root zone is depleted each day by evapotranspiration. Some recovery of water content occurs each night, as water from deeper in the soil is drawn into the root zone by capillary action. After several days with no precipitation, moisture recovery is reduced, as drying extends deeper into the soil profile.

Stomatal resistance for a given plant species may be fairly independent of leaf water potential down to a species-specific threshold value. If leaf water potential drops below the threshold, stomatal resistance increases sharply (Baldocchi et al., 1987).

Atmospheric humidity also has a direct effect on stomatal resistance. Stomatal resistance has been observed to increase with increasing vapour density deficit (Jarvis and Morrison, 1981). The sensitivity of different plant species to atmospheric humidity varies widely (Losch and Tenhunen, 1981), with some plants showing very little response.

The effect of soil moisture on stomatal resistance may explain successively higher surface resistances observed from August 10th-13th. August 10th ended a period of wet weather (see Table 2.2 for precipitation measurements), during which soil moisture was somewhat replenished. It is reasonable to assume that over the next few days of clear, warm weather, the soil was increasingly depleted of its water storage. The highest daytime surface resistances were observed on August 27th. This day followed four days of warm, dry weather, during which the soil would have dried significantly. The surface-layer on the 27th also had a significantly larger vapour density deficit than on the other days (Table 3.3). A high level of moisture stress, combined with a large atmospheric moisture deficit is thus a very probable explanation for higher surface resistances on the 27th.

Afternoon increases in surface resistance observed in this study (Figures 3.5 and 3.6), may have resulted partly from the effects of humidity and water stress, as well as from the diurnal cycle of solar radiation. Such increases have been reported in other observational (Wesely et al., 1978; Stocker et al., 1993) and modelling (Baldocchi et al., 1987) studies of dry deposition.

Table 3.3: Range of atmospheric vapour density deficits measured at the Pitt Meadows auto-station for the eight measurement days in August, 1994.

Measurement Date	Vapour Density Deficit ($g \cdot m^{-3}$)
August 10	15
August 11	14-18
August 12	9-13
August 13	11-16
August 14	8-12
August 27	16-21
August 30	8-12
August 31	8-12

In Figure 3.7, surface resistance is plotted against total shortwave radiation measured at the University of B.C. (located 40 km west of the field site). Radiation measurements taken at this location should represent radiation at the field site quite well. On days with scattered clouds, the distal location of the radiation sensor may have contributed some error to radiation measurements. Significant cloud was present only on the 14th and 31st of August.

Total shortwave radiation was used in Figure 3.7, rather than PAR, since no measurements were made of PAR. Typically, PAR and total shortwave are very highly correlated, except under special circumstances such as within a vegetation canopy. Thus it is reasonable to use total shortwave as a proxy for PAR (Pearcy, 1989).

Figure 3.7: Dependence of surface resistance on solar radiation. Squares represent measurements taken mid-afternoon on August 27th. Triangles represent all other days.

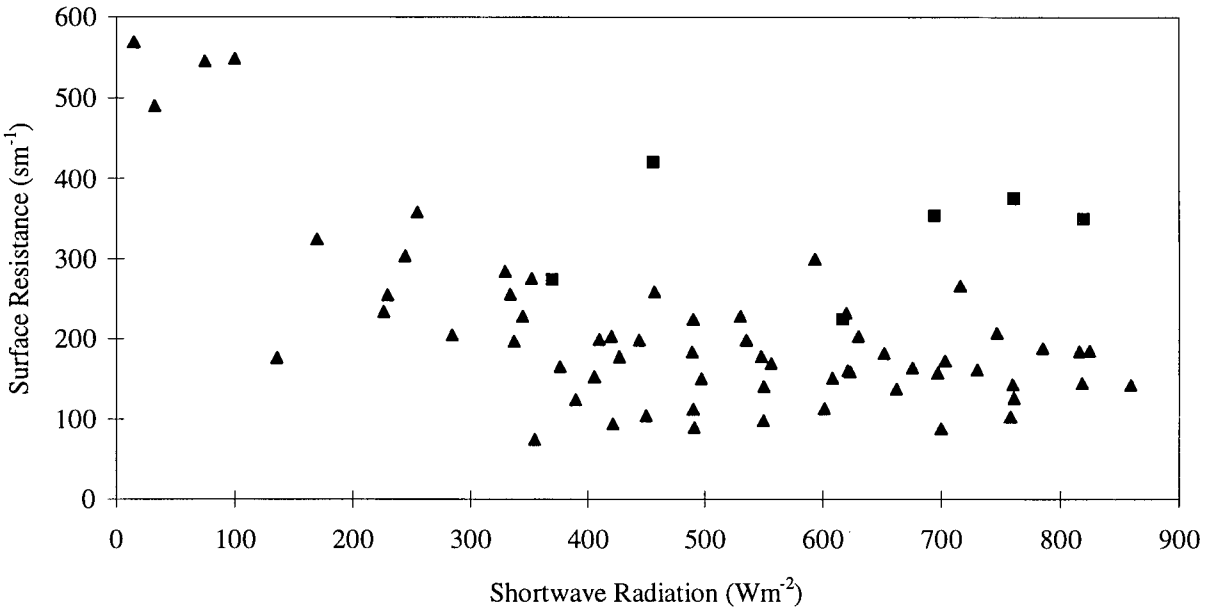

The functional relationship between PAR and stomatal resistance (Baldocchi et al., 1987) is commonly assumed to be rectangular hyperbolic. Measurements shown in Figure 3.7 are consistent with this functional form of dependence on PAR. At shortwave radiation intensities greater than about 400 Wm^{-2}, surface resistance was relatively insensitive to changes in light intensity. At lower light levels, surface resistance increased substantially with decreases in light intensity. The increase in surface resistance was limited, since as stomatal resistance increased, a greater proportion of ozone was deposited to the leaf, stem and soil surfaces.

The measurements in Figure 3.7 were not free of confounding factors. In particular, near-surface air temperature and vapour density deficit also tended to vary with solar radiation, and may, therefore, have exaggerated the apparent dependence. However, temperature varied only

between 19 and 31°C, through the measurements (Table 2.1). Within that range temperature does not greatly affect stomatal resistance (Baldocchi et al., 1987).

Variation of vapour density deficit and leaf water potential, throughout the measurement period, is partially responsible for the wide range in surface resistances observed at any given light level (Figure 3.7). For instance on the 27th, the soil was drier and the vapour density deficit higher than on other days. This led to substantially higher minimum surface resistances on that day, independent of light levels.

3.4 Comparison of measured surface resistances with W89 surface resistances

3.4.1 Description of the W89 surface resistance algorithm

Wesely (1989) proposed a relatively simple algorithm for calculating surface resistance to deposition of pollutants. His deposition module was designed to be used in regional scale air quality models. Since publication, this algorithm has gained fairly wide acceptance. It is included in a number of air quality models, including the UAM-V and the Regional Acid Deposition Model.

W89 calculates surface (or bulk canopy) resistance for eleven different landuse categories and five seasonal categories. Selection of appropriate landuse and seasonal categories to describe a given location, at a given time, adds a measure of subjectivity to the model. Landuse categories are by necessity rather broad. For instance, only three landuse categories represent all agricultural land, range land and combinations thereof. All landuse and seasonal categories are listed in Table 3.4.

Table 3.4: Landuse and seasonal categories in the W89 module.

Landuse Categories		Seasonal Categories
urban land agricultural land range land deciduous forest coniferous forest mixed forest including wetland water, both salt and fresh barren land, mostly desert nonforested wetland mixed agricultural and range land rocky open area with low growing shrubs		midsummer with lush vegetation autumn with unharvested cropland late autumn after frost, no snow winter, snow on ground and subfreezing spring with partially green short annuals

W89 uses the following formulation for bulk canopy resistance, r_c:

$$r_c = \left[\frac{1}{(r_s + r_m)} + \frac{1}{r_{lu}} + \frac{1}{(r_{dc} + r_{cl})} + \frac{1}{(r_{ac} + r_{gs})} \right]^{-1} \tag{3.1}$$

where r_s is bulk stomatal resistance, r_m is mesophyll resistance, r_{lu} is outer vegetation surface resistance in the upper canopy, r_{cl} is lower canopy - outer surface resistance and r_{gs} is ground surface resistance. Within-canopy aerodynamic resistances to transport are r_{ac} and r_{dc}, for ground and lower canopy respectively. Figure 3.8 is a schematic diagram, showing the arrangement of the various component resistances that make up the total resistance.

Stomatal resistance is estimated using the following function:

$$r_s = r_i \{1 + [200(G + 0.1)^{-1}]^2\} \{400[T_S(40 - T_S)]^{-1}\} \left(\frac{D_{H2O}}{D_x} \right) \tag{3.2}$$

where r_i is the minimum stomatal resistance for water vapour, G is solar radiation and T_S is near surface air temperature. This functional form gives a rapid increase of r_s for low light levels and little dependence on light levels above 400 Wm^{-2}. The temperature dependent term causes a rapid

increase of r_s with temperatures outside the range of 10 - 30°C. The final term is the ratio of molecular diffusivities of water vapour and the gas of interest, x. In the case of ozone, this term has a value of 1.6

Mesophyll resistance is assumed to be zero for ozone uptake. Lower canopy aerodynamic resistance is calculated using the following function:

$$r_{dc} = 100[1+1000(G+10)^{-1}](1+1000\theta)^{-1} \qquad (3.3)$$

Solar radiation, determines the amount of buoyant mixing within the canopy. Slope angle, θ, determines the degree of wind penetration into the canopy.

The module uses existing parameterizations (e.g. Equations 1.8 - 1.11 or equivalent) for the atmospheric and sublayer resistances.

Figure 3.8: Schematic diagram of the arrangement of component resistances in the W89 surface resistance parameterization.

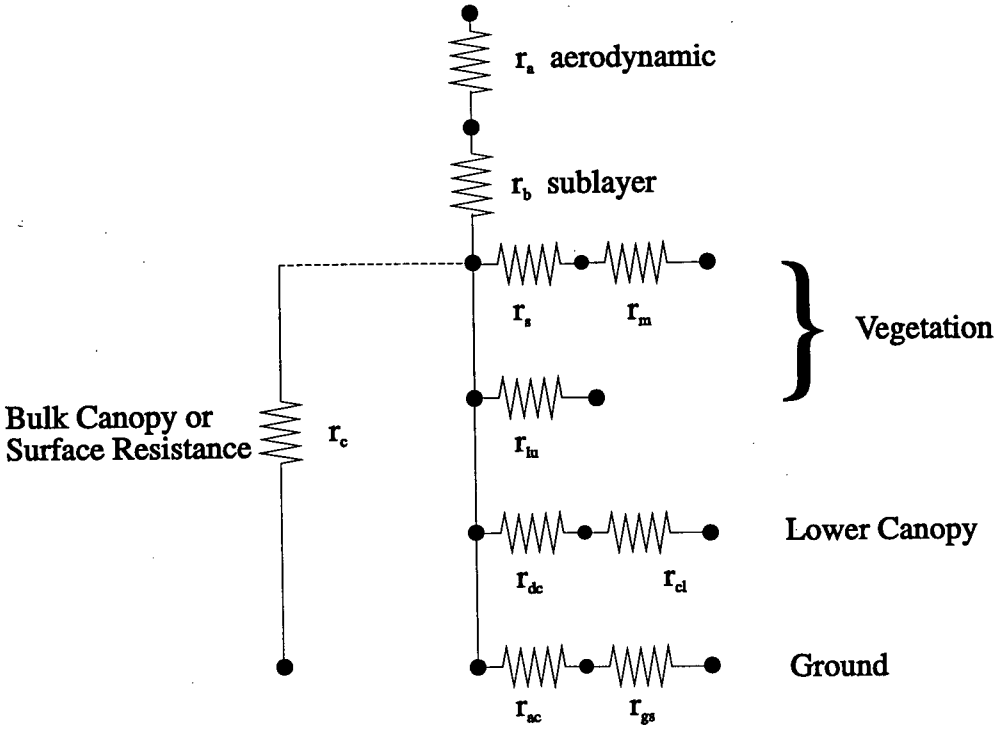

Surface resistance calculations are based on look-up tables for components of bulk canopy resistance for each land use and seasonal category.

The version of W89 incorporated in the UAM includes a crude representation of the effect of water stress on stomatal resistance (SAI, 1995). Three vegetative states are identified: (1) irrigated vegetation or active unirrigated vegetation in unstressed conditions, (2) active unirrigated vegetation in stressed conditions, and (3) inactive vegetation. For the first state, stomatal resistance is calculated as described above. For the second state, the calculated stomatal resistance is multiplied by a constant factor (default value is 10) to simulate reduced stomatal opening. For inactive vegetation, stomatal resistance is arbitrarily set to a high (10^4) value, effectively closing the stomatal pathway to deposition. The effect of water stress is also included implicitly by using higher minimum stomatal resistances for drier landuse types.

The effect of atmospheric vapour density deficit on stomatal resistance is not directly included in W89. However, the increase in surface resistance due to surface wetting by dew or rain is included.

3.4.2 Comparison with W89

Surface resistances were calculated using W89 for each measurement period during the study. Landuse category 3 - range land; and seasonal category 1 - midsummer with lush vegetation, were chosen to represent the study area. Vegetation around the field site was considerably taller than typical for rangeland, however, none of the other categories came as close to describing the site. The appropriate seasonal category was also debatable; since there was a

significant amount of brown, senescent vegetation, the site had some characteristics of seasonal category 2 (autumn, unharvested cropland).

Table 3.5 shows the values recommended by Wesely, (1989) for the various components of the bulk canopy resistance.

Table 3.5: W89 resistance values for range land, land use category during the midsummer, lush vegetation, seasonal category.

Resistance Component	Resistance (s/m)
r_i	120
r_{lu}	2000
r_{ac}	100
r_{gs}	200
r_{cl}	1000

Measured and modelled values of surface resistance for all measurement periods are shown in Figure 3.9. The diurnal course of measured and modelled values is shown in Figure 3.10. It is apparent from these graphs that the W89 parameterization worked relatively poorly at this site, underestimating the surface resistances in most cases. Minimum resistances predicted by W89 are reasonable, however, the model failed to predict the slow rise in surface resistance through the afternoon. The model did predict increased surface resistances in the evening hours. However the predicted increase was much less than the actual increase.

The ratios of modelled to measured resistances are given in Table 3.6. This ratio gives a measure of the discrepancy between the two.

The model seems to suffer from two problems. Relatively constant daytime values from the model in comparison to the observations which show a rise in surface resistance, suggest that

Figure 3.9: Measured values of surface resistance and values predicted using W89. Circles are unmodified W89, triangles are W89 with ground surface resistance increased from 300 sm^{-1} to 700 sm^{-1}. The straight line is 1:1.

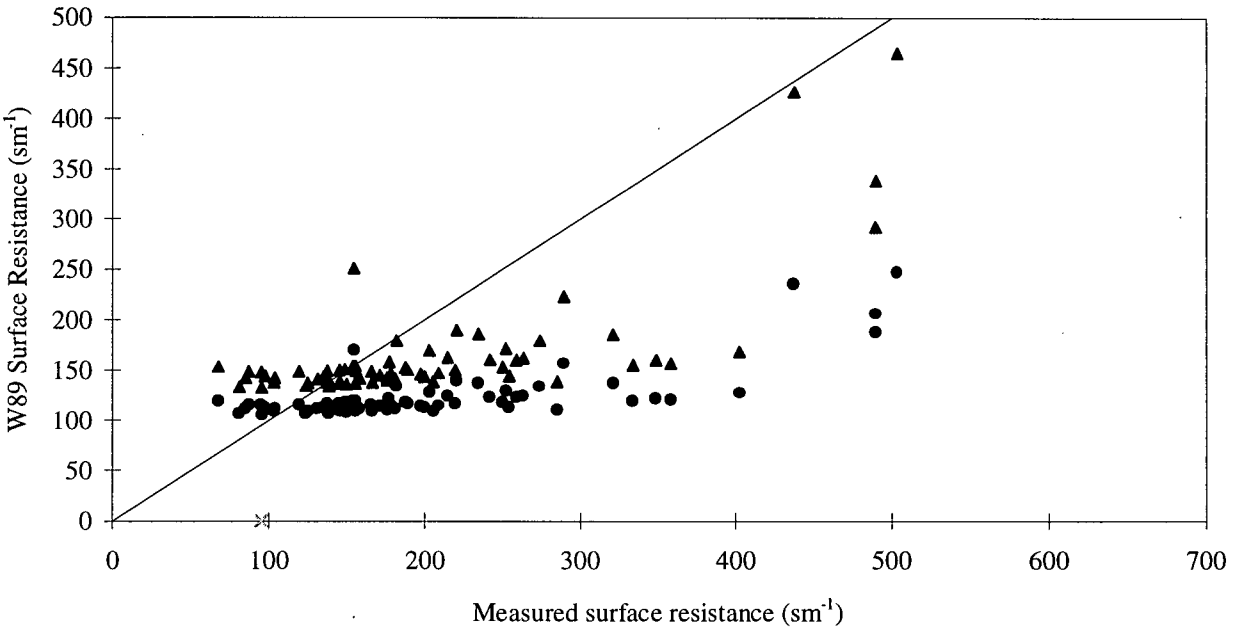

Figure 3.10: Diurnal course of surface resistance - measured and predicted from W89 and W89 with increased resistance to ground deposition.

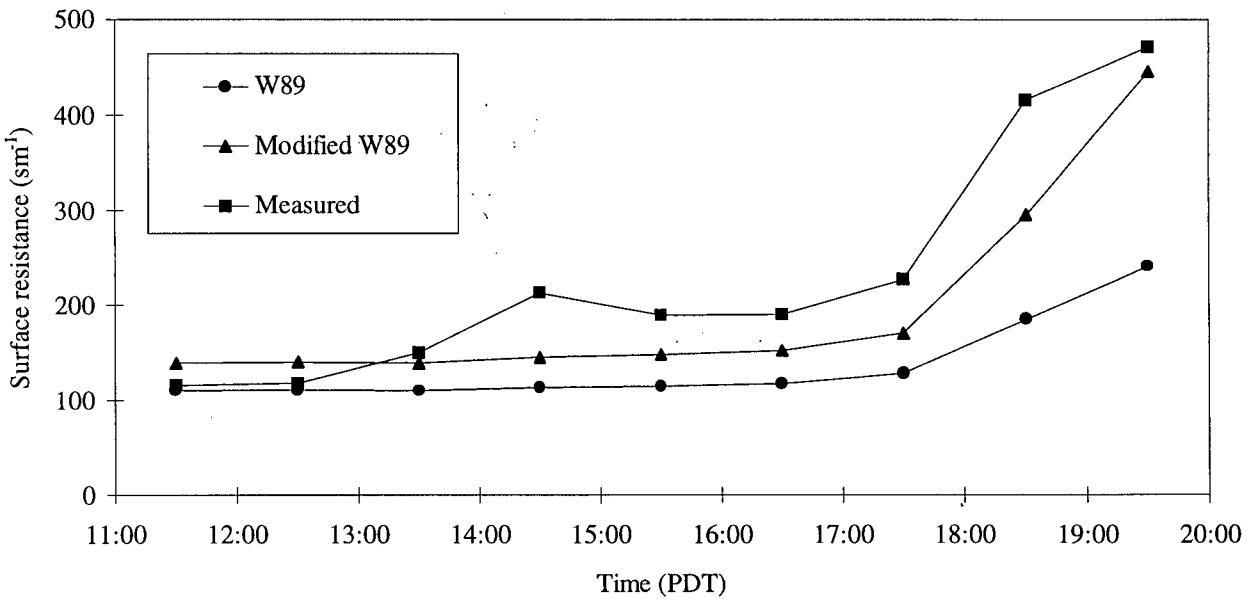

Table 3.6: Ratios of modelled (W89 and modified W89) to observed surface resistances.

Time Period	Average Measured Resistance	Ratio of W89 to Measured Resistance	Ratio of Modified W89 to Measured Resistance
1100-1200	116	0.95	1.20
1200-1300	118	0.94	1.19
1300-1400	150	0.73	0.93
1400-1500	213	0.53	0.68
1500-1600	189	0.61	0.78
1600-1700	190	0.62	0.80
1700-1800	227	0.56	0.75
1800-1900	416	0.44	0.71
1900-2000	471	0.51	0.95

the parameterization is lacking an important factor. This difference between W89 and observations remains even if other landuse and seasonal types are chosen. Since the parameterizations for the effect of light levels and air temperature are standard, well-tested equations, the fault may lie with the model's neglect of humidity and water stress effects on stomatal resistance.

The afternoon rise in surface resistance, observed in the measurements, is consistent with increasing water stress (lower leaf water potential) through the day as root zone water is depleted. Overnight some root-zone water replenishment occurs, so resistances may be low again the following day. This pattern has been observed in other studies (Wesely et al., 1978; Stocker et al., 1993).

The present study did not measure surface resistances over a long enough period, nor over a wide enough range of moisture conditions, to suggest a parameterization for the effects of water stress and humidity on surface resistance that could be added to the W89 module. Since no

measurements were taken of leaf water potential at the site, existing parameterizations for the effects of water stress could not be tested either.

However, Figure 3.10 and Table 3.6 show the magnitude of correction that would be required to bring the modelled values into agreement with the measured values. A very simple empirical approach to incorporating the effects of humidity and water stress would be to use the ratios in Table 3.6 as correction factors for the W89 surface resistance. Crude as this is, it might still provide an improvement over the "on/off switch" for water stress that is currently incorporated in the UAM.

The second major problem with the parameterization is its failure to predict sufficiently high surface resistance in the evening hours. Because of the parallel arrangement of resistances assumed in the model (Figure 3.8), the total surface resistance will always be less than the resistance of whichever pathway offers the least resistance. From Table 3.5, the pathway to deposition on the soil and leaf litter has a resistance of only 300 sm^{-1}. This resistance is the sum of the within canopy aerodynamic resistance (r_{ac} = 100 sm^{-1}) and the surface resistance of soil/leaf litter (r_{gs} = 200 sm^{-1}).

Surface resistances were calculated with W89, using a higher resistance to ground surface deposition ($r_{ac} + r_{gs}$ = 700 sm^{-1}). These values are also shown in Figures 3.9 and 3.10. Higher resistance along the ground deposition pathway considerably improved the estimates of surface resistance in the evening hours. The above modification also improved agreement between model and measurements during daytime hours, although it led to an ovestimate of surface resistance around mid-day. Modelled surface resistances also increased slightly through the afternoon hours, but were still significantly lower than measured values.

Increasing the resistance of the ground deposition pathway is probably justified at this site. Within canopy aerodynamic resistance is a function of canopy height and density. The vegetation canopy at the Pitt Meadows field site was roughly 1.5 m high, significantly taller than typical for rangeland. Furthermore the ground surface was never exposed at the site, being covered by a dense mat of dead vegetation.

Stocker et al. (1993) measured ozone fluxes to shortgrass prairie. They calculated a resistance to ground surface deposition of 440 sm^{-1}, at a site more sparsely vegetated than the Pitt Meadows site. A somewhat higher value, 700 sm^{-1}, can be justified at this site.

Several other studies have compared the W89 parameterization to measurements of dry deposition. Padro et al. (1994) took measurements of ozone deposition over cotton and senescent grass in the Central Valley of California. Over cotton, stomatal resistances predicted using W89 were significantly higher than observed values through the middle and late afternoon. Separate measurements of stomatal resistance were not taken during the present study, however if a similar underestimate of stomatal resistance was present in this study it would account for the discrepancy between W89 and observations.

Padro et al. do not speculate on the cause of the discrepancy between observed and modelled stomatal resistance. Moisture stress is a possible cause; unfortunately they do not discuss moisture conditions at their site.

Over senescent grass site W89 reproduced the observed deposition velocities quite well if the "barren land" land-use category was chosen. If the "range-land" land use category was chosen the deposition velocity was greatly overestimated. This illustrates the importance of chosing the correct land-use category.

Padro (1993) compared W89 to observations over a deciduous forest in spring. W89 underestimated deposition velocities by about 25%. Padro attributed this to an inadequate parameterization for deposition to wet surfaces in W89.

If the discrepancy between modelled and observed surface resistances observed in the present study also holds true for significant portions of the LFV, then there are implications for modelling efforts currently underway. The afternoon underestimate of surface resistance by W89 would result in an overestimate of dry deposition by the UAM model. As a result the UAM might predict peak ozone earlier in the day than actually occurs, and might also underestimate the peak ozone concentrations.

4. COMPARISON OF FLUX MEASUREMENT TECHNIQUES

4.1 Cospectral similarity

Given two time series, sampled N times, at time intervals, Δt (i.e. for total sample length, $P = N\Delta t$); the cospectral intensity of the series is calculated as the product of the Fourier transforms of the two series in the following manner.

$$Co_{AB}(f) = 2[F_{Ar}(f)F_{Br}(f) + F_{Ai}(f)F_{Bi}(f)] \tag{4.1}$$

F_A and F_B are Fourier transforms of series A and B respectively. Subscripts r and i denote the real and imaginary parts of the Fourier coefficients. f is discrete frequency in cycles per second. The factor 2 accounts for folded energy from frequencies above the Nyquist frequency, $f_N = 1/(2\Delta t)$. The calculation of cospectra is explained in greater detail in Stull (1988).

Cospectral intensity is useful, since it represents the contribution to total covariance between A and B from a frequency band, df, centered on each frequency, f. Total covariance is equal to the sum of cospectral intensity over all frequencies between the fundamental frequency and the Nyquist frequency.

$$\overline{A'B'} = \sum_{f=\frac{1}{P}}^{\frac{1}{2\Delta t}} Co_{AB}(f) \tag{4.2}$$

Likewise, a sum of cospectral intensity over any band of frequencies produces a band-pass covariance, C_{AB}. The band-pass covariance is a measure of the fraction of total covariance contained within a given frequency band. For turbulent transport the

cospectral intensity is a measure of the proportion of flux carried by eddies within a given frequency (or size) range.

Hicks and McMillen (1988) suggest an approach for measurement of turbulent fluxes of trace quantities such as ozone or sulfur dioxide, that obviates the need for rapid-response eddy correlation sensors. They show that if a pollutant flux is transported in a similar manner to total (latent plus sensible) heat flux then the following relation can be derived:

$$F_C = 0.9R_n \frac{C_{wc}}{(\rho c_p C_{wT} + LC_{wq})} \tag{4.3}$$

where R_n is net radiation, and C_{wc}, C_{wT} and C_{wq} are band-pass covariances of vertical velocity with trace scalar concentration, temperature and humidity respectively. The factor 0.9 appears because they assume that 10% of available energy is partitioned into ground and canopy heat storage, while the remaining 90% of R_n is divided between latent and sensible heat.

Equation 4.3 is obviously true if the full frequency band, typically used for eddy correlation (roughly 10 Hz to 0.001 Hz), is used to compute the band-pass covariances. In that case Equation 4.3 simply reduces to Equation 2.1.

Assuming the shape of the cospectrum for scalar flux is identical to that for turbulent heat flux, then the ratio on the right side of Equation 4.3 is independent of the frequency band chosen for calculation of the band-pass covariances. In reality the cospectra are not identical but fairly similar. In particular the lowest frequency portions of the cospectra are inherently poorly sampled and thus prone to substantial errors. This portion of the cospectra may also be affected by variations unrelated to turbulent transfer.

Thus a wide enough frequency band must be chosen such that differences in the low frequency portion of the cospectra do not overly affect the ratio of the band-pass covariances.

The advantage of this method of flux measurement is that it allows more slowly responding instruments to be used than is the case for eddy correlation measurements. An instrument with a slow response time functions as a crude low-pass filter and can thus be used to measure band-pass covariances, as required in Equation 4.3. When using this method, care must be taken that the pass-band is the same for each covariance used in the calculation. Formally, this would mean that all the signals (w, T, q, C in Equation 4.3) would be filtered using the same low-pass filter before recording. The filter cut-off frequency would be chosen to be equal or slightly below the cut-off of the most slowly responding instrument.

Hicks and McMillen (1988) applied the method described above to a data set from a study of sulphur dioxide and particle deposition. Their results showed that the method would produce reasonable flux estimates, with simulated instrument response times as long as 30 seconds.

The exact method used by Hicks and McMillen could not be applied in this study, since the necessary energy budget terms (R_n and either the Bowen ratio, β, or $\overline{w'q'}$) were not measured. However, a similar method, also exploiting the method of cospectral similarity, was applied.

If one scalar flux can be measured with a high degree of reliability over the full range of transporting eddies, then the flux of another scalar, transported in a similar manner, can be inferred:

$$F_C = F_S \frac{C_{wc}}{C_{ws}} \tag{4.4}$$

by a method similar to Equation 2.8, except using band-pass covariances instead of variances. Examples of scalar fluxes that are relatively easy to measure, and could be used to infer other fluxes, are heat and moisture fluxes.

4.2 Comparison of fluxes from cospectral similarity and eddy-correlation

Using measured heat fluxes, Equation 4.4 was used to infer the ozone fluxes (this method will herein be referred to as the 'cospectral method'). Band-pass covariances of temperature and ozone with vertical velocity were generated from the original data, using band-pass filters to simulate different instrument response times. Data from 62 sampling periods were used in the analysis. These were all the samples that met the fetch requirements discussed in Appendix D.2, with the exception of seven samples that were rejected because of their short (<20 minute) sampling period.

Ozone fluxes, calculated in this manner, were compared to the uncorrected eddy correlation fluxes (sampled at 10.5 Hz). For this purpose, eddy correlation values were regarded as the 'true' values. Errors for the flux estimates from the cospectral method were calculated as percentage differences from the 10.5 Hz eddy correlation values.

Uncorrected eddy correlation measurements were used as the standard of comparison because the ozone fluxes presented in Chapter 3 already have a slight frequency correction applied to compensate for the 1 second response time of the ozone sensor (as described in Appendix A).

The comparison was made using simulated response times of 0.1, 0.25, 0.5, 1, 2.5, 5, 15, 30, 60 and 150 seconds.

Cospectra of temperature and ozone with vertical velocity were calculated according to Equation 4.1 (see Appendix C.3 for the S-Plus code). To generate band-pass covariances, Fourier coefficients for frequencies above each simulated Nyquist frequency were set to zero, those below were multiplied by one.

The type of filter described above is an ideal band-pass filter since it has a sharp cut-off frequency. However, this type of filter does not have optimum characteristics, in the sense that its impulse response has ringing at frequencies associated with the sharp edges of the filter (Press et al., 1992).

The ideal cut-off filter can be approximated by a series of cosine terms (Voogt, 1989). Forty terms of the series were used to produce a close approximation of the ideal filter. The resulting filter has a less sharp cut-off than the ideal filter but a superior impulse response.

To determine whether the method of filtering had any effect on the performance of the cospectral method, a comparison was made using three types of filter. Band-pass covariances were calculated for 20 sampling periods using: (1) the ideal band pass filter,

(2) the 40 term approximation to the ideal filter and (3) block averaging in the time domain. The frequency response of the three types of filter is shown in Appendix E.

Table 4.1 lists the relative error of the cospectral method for each filter type for three typical cases. Depending which of the three filter types was used for calculating band-pass covariances, error associated with the cospectral method varied slightly for each specific sampling period and simulated response time. However, it did not vary significantly enough to alter conclusions about the method. The only systematic difference between the three methods was the tendency for the block averaging to produce smaller relative errors at relatively rapid response times. For this reason it was decided to use the ideal frequency domain cut-off filter.

Figures 4.1 (a) - (d) show average relative error of flux measurements using the cospectral method for all simulated instrument response times. For comparison, relative errors that would be obtained with uncorrected eddy correlation, using instruments of the same (increasingly long) response time are shown. The uncorrected, eddy correlation ozone flux for a given instrument response time is simply equal to the corresponding band-pass covariance of vertical velocity and ozone.

Table 4.1: Relative errors (%) of the cospectral method for three types of filter for three unstable atmosphere cases.

	Relative Error								
Simulated Response Time	Ideal Cut-off Filter			Approximation to Cut-off Filter			Block Averaging		
1	6.0	5.1	6.3	5.8	5.0	5.9	1.7	0.7	2.3
5	0.2	5.7	5.6	1.1	5.4	5.5	2.7	3.1	5.3
30	17	11	2.8	17	11	3.0	18	16	1.9
60	53	21	7.2	50	22	7.6	45	41	0.7

Figure 4.1: Mean magnitude of relative error for cospectral method and eddy correlation over a range of simulated response times. The errors are calculated relative to the 10.5 Hz eddy correlation measurements: (a) highly unstable atmosphere; (b) moderately unstable atmosphere; (c) stable atmosphere and; (d) near neutral atmosphere.

(a) Highly unstable atmosphere ($z/L < -0.25$) - 18 cases

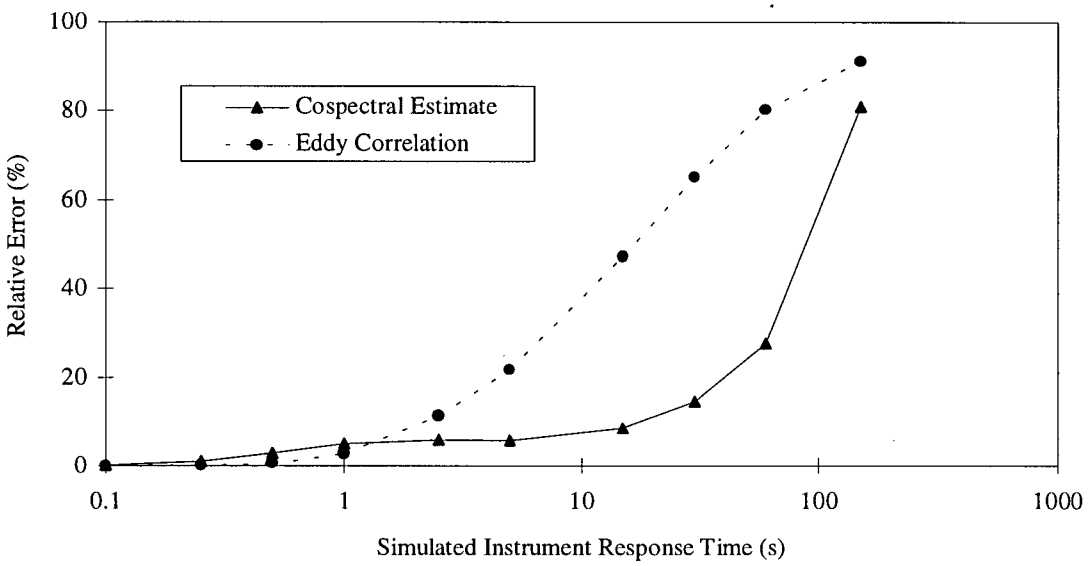

(b) Moderately unstable atmosphere ($-0.25 < z/L < -0.05$) - 34 cases

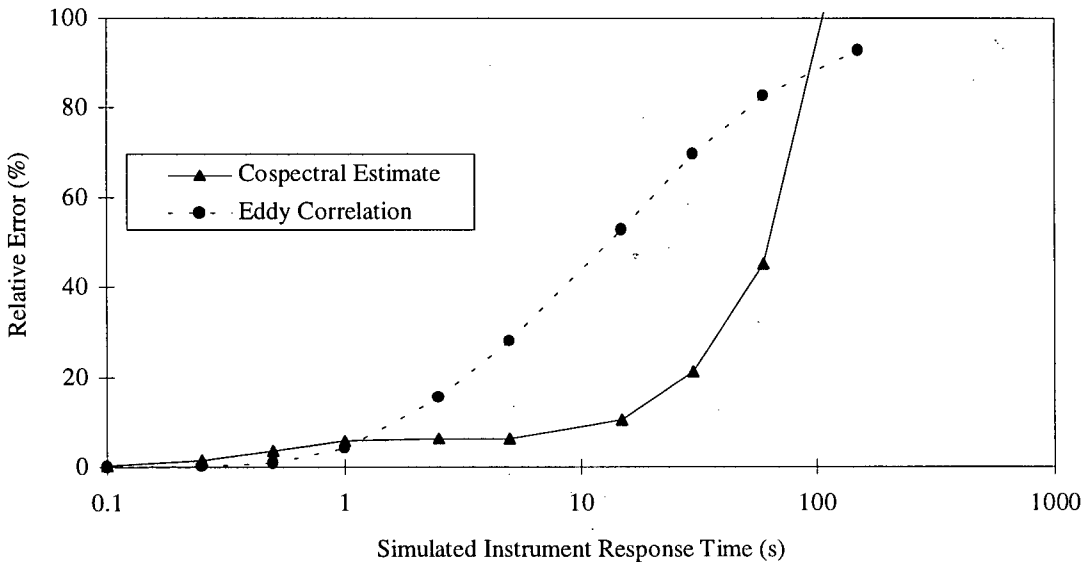

(c) Stable atmosphere (z/L > 0.05) - 5 cases

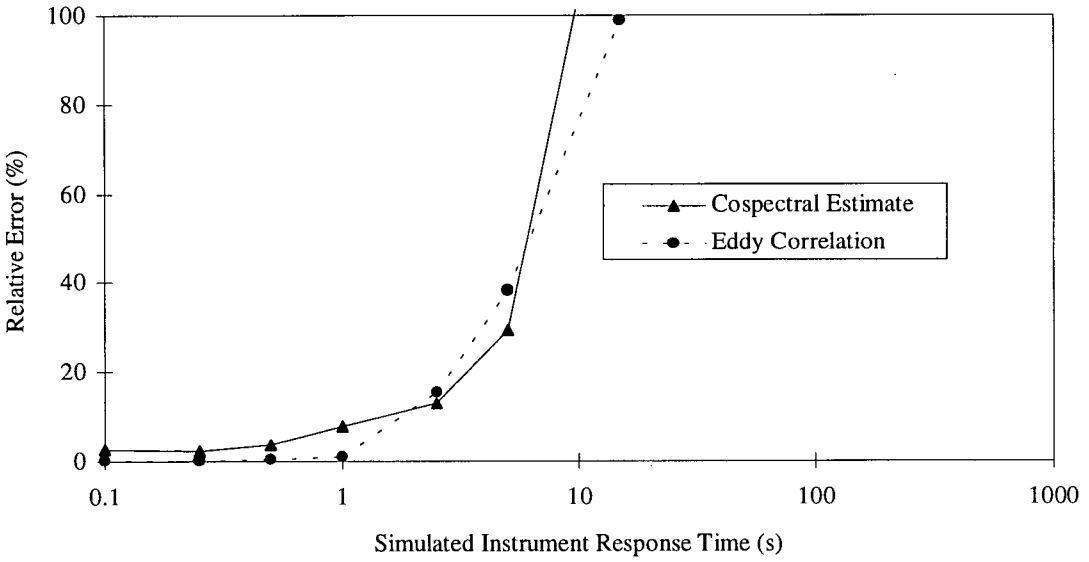

(d) Near neutral atmosphere (-0.05 < z/L < 0.05) - 5 cases

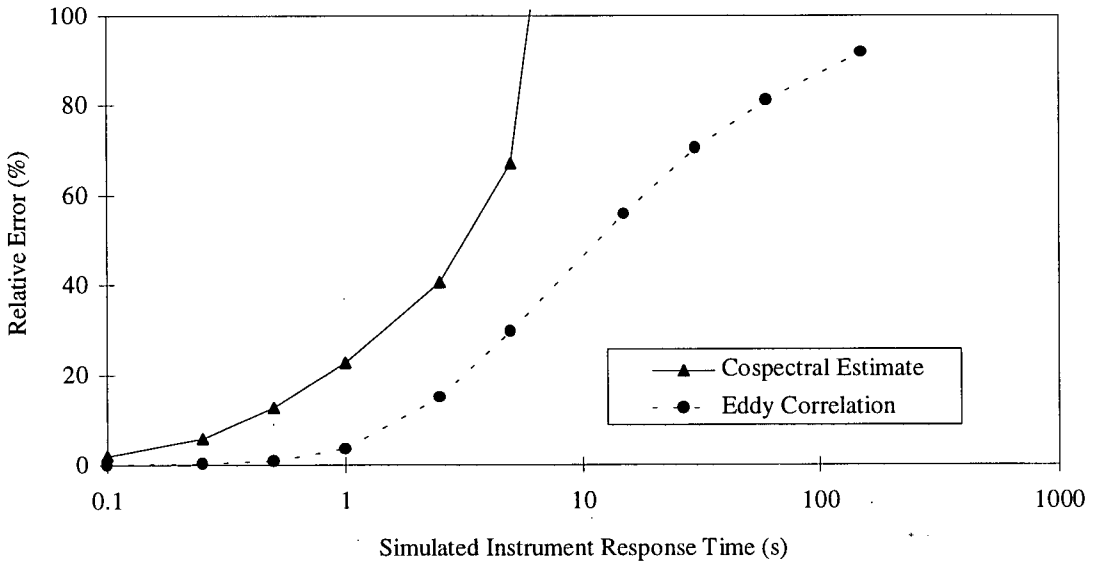

The cospectral method worked best in unstable cases (Figure 4.1 (a) and (b)), where it offered a significant advantage over uncorrected eddy correlation for a range of instrument response times from 2 to 30 seconds. In stable atmosphere cases the cospectral method performed fairly similarly to uncorrected eddy correlation, both having a fairly rapid increase in relative error with longer instrument response times. The cospectral method performed poorly in the near neutral case, having greater errors than eddy correlation across the entire range of simulated instrument response times.

There are several reasons why the cospectral method worked better in the unstable surface layer. First, it appears that during unstable conditions, similarity between ozone and heat transport is greatest. This is borne out by values of r_{cT} (Table 3.2) which are generally highest for the most unstable cases. Second, during daytime, unstable atmosphere cases, the data were most closely stationary which means the cospectra more accurately represented actual transport processes, rather than low frequency noise from nonstationarities. Third, and probably most important, dominant eddy scale increases with increasingly negative values of the stability parameter. As dominant eddy scale increases a greater fraction of flux is carried by larger eddies and thus the low frequency part of the cospectra is relatively more important for flux transport.

For near neutral atmospheres the cospectral method worked poorly. In these cases there was little, if any, heat transport. Under these conditions heat and ozone transport were poorly correlated (Table 3.1), so the assumption of cospectral similarity between heat and ozone was not even approximately true. In addition, since near neutral cases were sampled around sunset, both the temperature and ozone series showed significant

nonstationarities. These nonstationarities would tend to add low frequency noise to the cospectra and thereby increase error for the cospectral method.

In stable conditions, temperature and ozone signals were correlated, though less highly than in unstable cases (e.g. Figure 3.2, Table 3.1). However, transport of heat and ozone occurred at relatively smaller scales (higher frequencies) compared to the unstable cases. In these cases low-pass filtered cospectra of heat and ozone bore little similarity to each other since the filtering removed many of the important flux carrying events. Stable cases were generally less strictly stationary than the unstable cases, which may also have contributed to poor performance in this stability class.

The numbers of samples in each stability class in Figure 4.1 are: 18 in the highly unstable class, 34 in the moderately unstable class, and 5 each in the stable and near neutral classes. Because of the small number of flux measurements taken in neutral and stable atmospheres, as well as the much higher uncertainty in those measurements, results for those cases can not be considered conclusive.

For small instrument response times, error using the cospectral method was greater than using eddy correlation (at the same response time) for all stability classes. This was due to high frequency attenuation of the ozone signal, due to slower than expected (i.e. slower than claimed in the accompanying literature) actual response time for the ozone sensor (see Section 4.3). Since the ozone sensor was not fully responding to concentration fluctuations at frequencies between 5 and 0.5 Hz, results for the cospectral method over the corresponding range of instrument response times (0.1 to 1 second) are biased.

Table 4.2 lists, for each simulated response time, mean magnitude of (relative) error, and mean (relative) bias error of the cospectral estimates relative to the eddy correlation (sampled at 10.5 Hz) measurements.

Mean magnitude of (relative) error (MME) measures the spread of the cospectral flux estimates around the expected (eddy correlation) values. It is given by:

$$MME = \frac{1}{N}\sum_{i=1}^{N}\left|\frac{F_{EC} - F_{CO}}{F_{EC}}\right|_i \times 100\% \qquad (4.5)$$

where N is the number of cases and F_{EC} and F_{CO} are the eddy correlation and cospectral fluxes respectively.

Mean (relative) bias error (MBE) measures systematic bias of the cospectral estimates. It is given by:

$$MBE = \frac{1}{N}\sum_{i=1}^{N}\left(\frac{F_{EC} - F_{CO}}{F_{EC}}\right)_i \times 100\% \qquad (4.6)$$

MBE is perhaps the more relevant error estimate for studies of surface resistance, since typically results from several sampling periods will be averaged together.

MME (essentially the scatter of the estimates) increases almost monotonically with increased simulated response time. Sensors with longer response time sample the flux over a smaller bandwidth (assuming a fixed sampling period, P). This is simulated in the present study by multiplying an increased proportion of the high frequency side of the cospectra by zero for longer response times. Since they use a smaller portion of the cospectra, the measurements at slower response times are more prone to random variations in the low frequency portion of the cospectra.

Table 4.2: Mean magnitude and mean bias errors of the cospectral flux estimates, for all unstable cases (z/L < -.05, N = 52).

Simulated response time (s)	Mean magnitude error (%)	Mean bias error (%)
0.1	0.2	-0.1
0.2	1.2	-1.2
0.5	3.3	-3.3
1	5.1	-5.1
2.5	6.2	-6.0
5	6.0	-4.3
15	9.8	1.0
30	19	7.8
60	39	10.8
150	120	45.5

MBE on the other hand is negative (corresponding to an overestimate of the always-negative ozone flux) for smaller response times; near zero around 15 second response time; and increasingly positive over longer response times. An inspection of the cospectra presented in the next section will explain this behaviour.

The main conclusion to be drawn from Table 4.2 is that the cospectral method worked very well for response times of up to 15 seconds. For response times of 30 - 60 seconds, accuracy of the method is still acceptable though precision of individual measurements is poor.

In Figure 4.2 (a) and (b) the cospectral flux estimates for 30 second and 5 second simulated response times are plotted against the 10.5 Hz eddy correlation flux measurements for all sampling periods with z/L less than -0.05. A total of 52 sampling periods were in this category. Neutral and stable atmosphere measurements were not plotted in this manner since the cospectral method was shown to have little utility in these

Figure 4.2: Cospectral estimates versus the eddy correlation measurements, during unstable conditions ($z/L < -0.05$), for simulated instrument response times of (a) 30 seconds; and (b) 5 seconds. Diagonal lines are the 1:1 line along which estimates should lie.

(a)

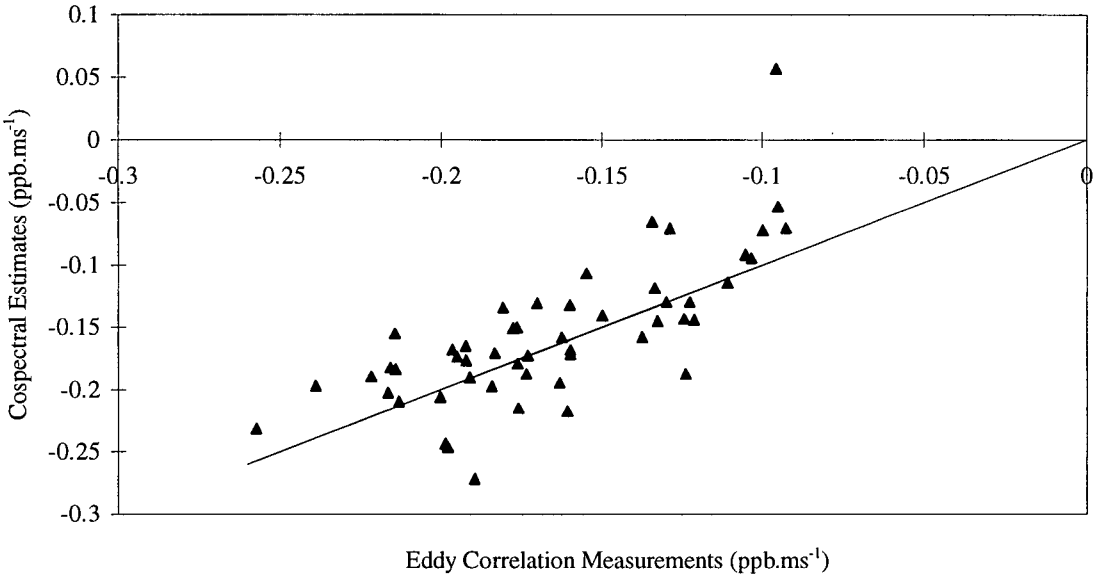

(b)

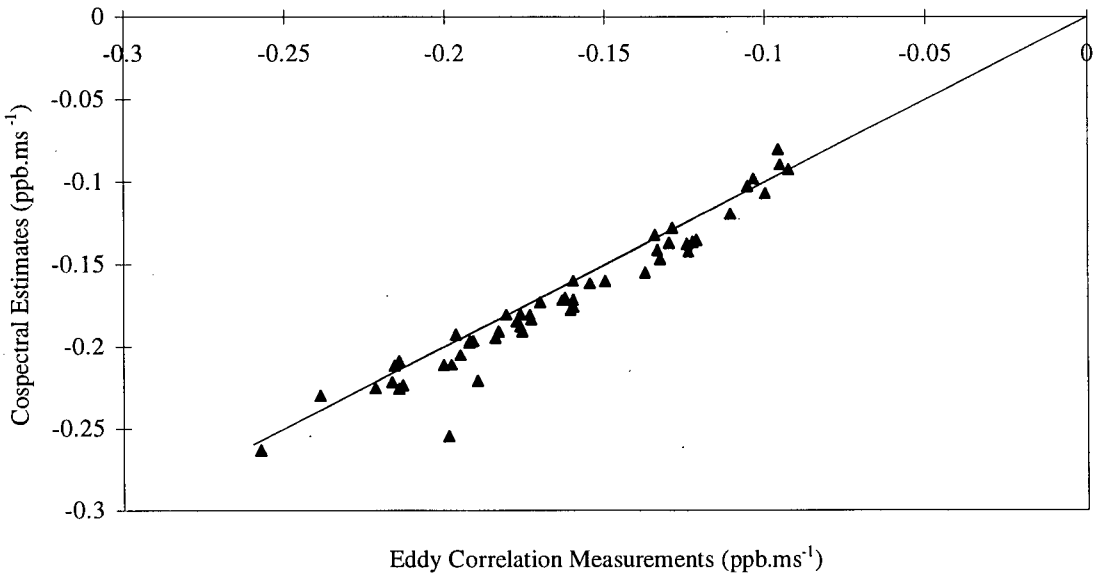

cases. Response times of 5 and 30 seconds were chosen to demonstrate the performance of the method across a range of simulated response times.

Figures 4.2 (a) and (b) together demonstrate increased error for longer response times. MME was 6% and 19% for the 5 and 30 second response times, respectively. MBE, on the other hand, was -4% for the 5 second response time and 7% for the 30 second response time.

To determine whether the differences between the cospectral estimates and the eddy correlation measurements were statistically significant, the difference between the 1:1 line and the least squares line through the estimates was evaluated. Using the Student t-test at 95% significance level, the difference was found to be statistically significant for 5 second response time and not significant for 30 second response time.

A substantial amount of the observed bias error may be due to shortcomings in the original uncorrected flux measurements (due to the frequency response of the ozone sensor) which are used as the standard. Even with these shortcomings the amount of bias is small, when compared to inherent uncertainty in the eddy correlation measurements.

4.3 Cospectra of temperature and ozone with vertical velocity

Figure 4.3 shows cospectra of temperature and ozone with vertical velocity during unstable conditions ($z/L < -0.05$). The cospectra presented are composites derived from averaging the individual cospectra for 35 sampling periods. The cospectra are presented on logarithmic axes. On logarithmic axes any power law relationship in the cospectra will appear as straight line segments.

The abscissa in Figure 4.3 is nondimensional, natural frequency, $f' = fz / \overline{u}$ (where $\overline{u}$ is the mean horizontal wind speed). Measurements of spectra or cospectra using a single, stationary sensor rely on mean wind to advect eddies past the sensor. Use of natural frequency normalizes for the effect of different mean wind speeds and allows the cospectra to be averaged together in a meaningful way.

The ordinate in Figure 4.3 is cospectral intensity as defined in Equation 4.1, divided by frequency interval, $\Delta f = 1 / P$, multiplied by frequency and normalized by the respective covariances. Dividing the cospectral intensity by frequency interval converts the units of Equation 4.1 from covariance to covariance per unit frequency. Multiplication by frequency shifts the apparent spectral peak to higher frequencies. This is the form most often presented in the literature because it is more easily normalized (Stull, 1988). Normalizing the cospectra by their respective, total covariances, again allows individual cospectra to be averaged together and also enables the ozone and heat flux cospectra to be compared directly. The ozone cospectrum is, in addition, multiplied by -1 so that it is positive (assuming a purely downward flux).

The ozone and temperature cospectra show very good agreement over a range of nondimensional frequencies from 0.01 to 1. For values of f' greater than 1 the ozone cospectrum drops off more rapidly than the temperature cospectrum. For f' less than approximately 0.01 the ozone cospectrum diverges significantly from the temperature cospectrum. In this low frequency range the ozone cospectrum has mainly negative values which cannot be depicted on the logarithmic axis.

Figure 4.3: Composite cospectra of sensible heat flux and ozone flux. The cospectra are normalized by their respective covariances. Triangles are heat flux, squares are ozone flux. The -4/3 line is shown for comparison.

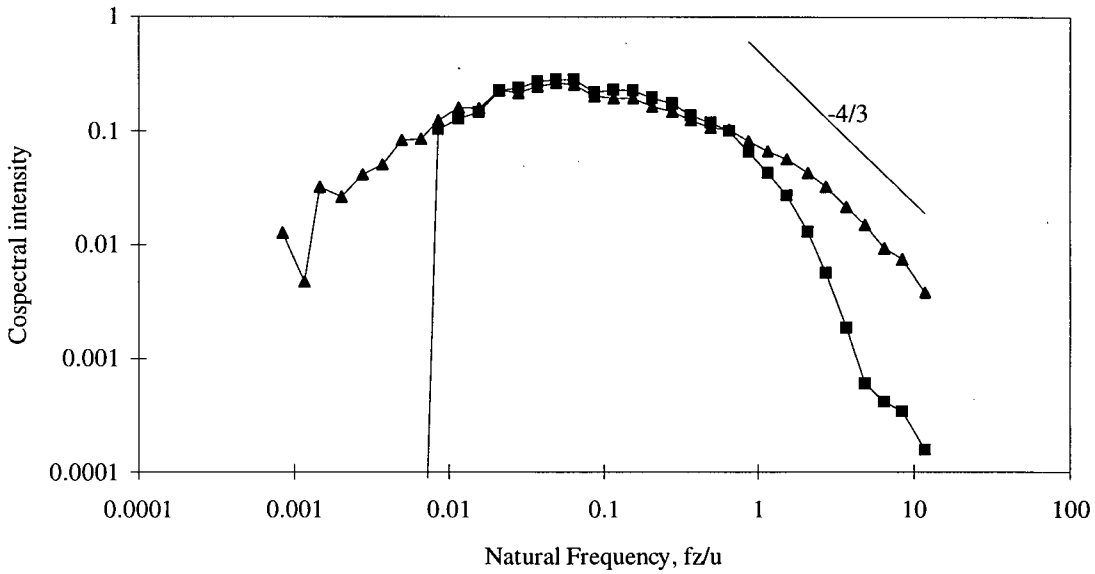

Dimensional analysis (Kaimal and Finnigan, 1994) shows that cospectra of heat flux or other scalar fluxes should decrease proportional to -4/3 power of frequency in the inertial subrange of the cospectra. Many studies have verified this prediction for heat flux cospectra (e.g. Wyngaard and Cote, 1972, Roth, 1988). Less is known about the cospectra of other scalar fluxes, but indications are that they have cospectra similar to heat flux (Kaimal and Finnigan, 1994). A cospectrum of ozone and vertical velocity presented by Godowich (1990) shows reasonable agreement with the -4/3 relationship.

The composite heat flux cospectrum shown in Figure 4.3 matches the -4/3 slope very well over nearly a full decade of frequency. Over that same decade of frequency the ozone cospectrum decreases much more quickly.

The more rapid than predicted falloff of ozone-vertical velocity covariance at high frequencies is most likely due to attenuation of the ozone signal at high frequencies. This high frequency attenuation was present in all individual cospectra examined as well as in the composite cospectra shown in Figure 4.3. It appears that the OSB-2 ozone sensor used in this study had a 90 % response time of roughly 1 second, rather than 0.1 second as reported by Gusten et al. (1992).

Attenuation of the ozone signal at high frequencies explains the bias in the cospectral estimates that is seen at relatively short simulated response times (Table 4.2 and Figure 4.2(a)).

A definitive explanation for the near zero to apparent upward flux of ozone observed at the lower frequencies (the missing points of the ozone cospectra in Figure 4.3) is not possible from the results of this study. It is hypothesized that it may have resulted from slow changes in the sensitivity of the sensor due to humidity variations (Gusten et al., 1992; GFAS, 1994). Since humidity fluctuations are highly correlated with both vertical velocity and ozone fluctuations during daytime unstable conditions (Wesely, 1988) this could cause a spurious positive correlation between vertical velocity and ozone that might overwhelm the actual negative correlation.

Since differences between the temperature and ozone cospectra in Figure 4.3 seem to result from shortcomings of the ozone sensor and not fundamental differences in the transport processes, the measured ozone fluxes should be reevaluated in this light.

This was done in Appendix A. The ozone fluxes were re-evaluated using Equation 4.4 and assuming exact similarity between heat and ozone fluxes. A filter with pass band

from 0.005 to 0.5 Hz, corresponding to the observed region of cospectral similarity, was used to calculate C_{wT} and C_{wc}. The ratio of C_{wc} and C_{wT} was used to correct the ozone fluxes presented in Chapter 3 for the observed high frequency attenuation. The corrections resulted in an increase of the fluxes by an average of 5%.

4.4 Variance method

The variance method, as described in Chapter 2.1, was also used to estimate the ozone fluxes. Standard deviations were calculated for the detrended ozone and temperature series (Table 3.1). The ratio of these were used to calculate the ozone flux (Equation 2.8).

Ozone fluxes estimated using Equation 2.8 are plotted against the eddy correlation measurements in Figure 4.4 for all unstable atmosphere cases. The method worked somewhat poorly for unstable cases. Flux estimates from the variance method are almost always greater than the measured ozone fluxes. Relative errors for the variance method estimates range from less than 1% to 280%. The mean bias error for the estimates is 37% corresponding to an overestimate of the true fluxes by that amount.

For the stable and neutral cases the variance method worked very poorly. Relative errors in these cases ranged from 7% to over 500%.

Figure 4.5 shows the composite spectra of temperature and ozone fluctuations for the nine daytime sampling periods on August 13th. The temperature spectrum falls off proportional to -2/3 power of frequency in the inertial subrange as expected from theoretical considerations (Kaimal and Finnigan, 1994). The ozone spectrum falls off

Figure 4.4: Comparison of ozone fluxes measured using eddy correlation method and estimated using the variance method. Measurements for all unstable periods (z/L < -.05) are shown. The straight line is the 1:1 line.

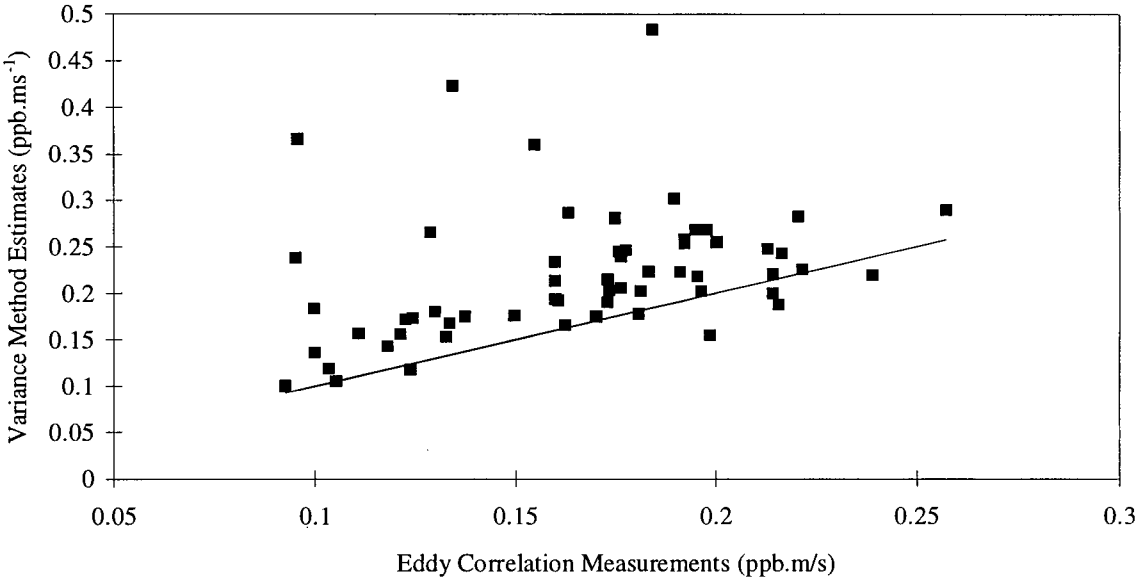

Figure 4.5: Composite spectra of temperature and ozone fluctuations for the nine sampling periods on August 13th 1230-1700. The spectra are multiplied by frequency and normalized by the total variances. A -2/3 slope line is shown for comparison. Triangles are temperature and squares are ozone.

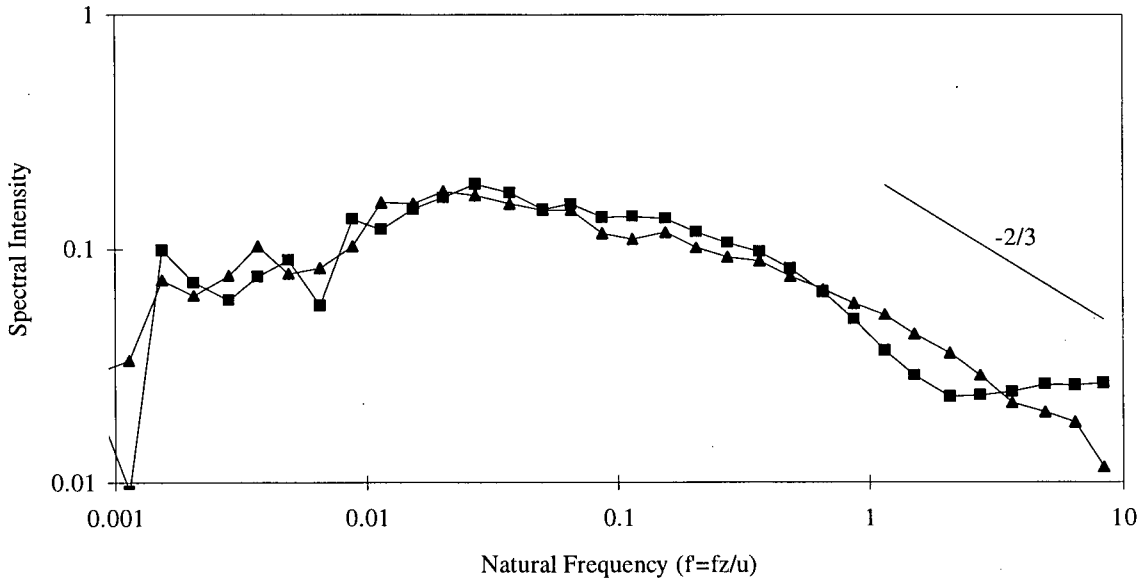

more rapidly initially before rising to a peak at the highest frequencies. The ozone spectrum is also more noisy than the temperature spectrum at low frequencies.

Differences between the two spectra are accounted for by the combined effects of attenuation of the ozone signal at frequencies above roughly 1 Hz. and high frequency noise aliased into the signal.

There are three main reasons that the variance method worked poorly:

1) The ozone sensor used in this study produced a substantial amount of high frequency noise. Instrumental noise at frequencies greater than the Nyquist frequency of 5.25 Hz was aliased into the data during the recording process (Figure 4.5). This high frequency noise caused the measured variance of ozone concentration to always exceed the actual variance. This high frequency noise was uncorrelated with the vertical velocity, so did not affect the eddy correlation measurements or the cospectral estimates.

2) Mean ozone concentration frequently varied over the course of the half hour measurement periods. Although ozone measurements were detrended with a least-squares line, other variations remained (i.e. Figure 3.2c). These variations often occurred over 10 to 30 minute time periods. Such variations are not thought to have resulted from turbulent mixing, especially since they were not present in the temperature signal. The effect of these nonstationarities was to increase the measured ozone variance above that due to turbulent fluctuations. Nonstationarities in the ozone signal were also most prevalent in the late afternoon and early evening hours.

3) Ozone concentrations throughout this experiment were quite low (20 - 60 ppb). Low ozone concentrations also contributed to the prevalence of instrumental noise. All other things equal, higher ozone concentrations will lead to greater variance due to turbulent mixing of the ozone. If ozone concentrations are low, variance contributed by instrumental noise will be a greater proportion of total variance.

High frequency instrumental noise had greatest effect on estimates of variance during late afternoon and early evening periods when turbulent mixing was weak and ozone concentrations low, so that the 'actual' variance was quite small. The proportion of variance contributed by instrumental noise also increased through the day as the sensitivity of the ozone sensor decreased. Decreasing instrument sensitivity meant that an increasing proportion of the signal from the ozone sensor was noise. The decrease in sensitivity was most rapid in the evening hours when ozone concentrations fell rapidly.

The above discussion explains why the variance method failed most badly for stable and neutral cases during evening hours, and performed much better for daytime unstable cases. It also explains why ozone standard deviations, shown in Table 3.1, actually increased in the evening hours, rather than decreased due to less intense turbulent mixing.

In summary the variance method proved to have limited utility for the measurement of ozone fluxes with the type of sensor used in this study. Estimates of ozone variance are biased by high frequency noise from the ozone sensor. Analog filtering of the ozone signal prior to recording would have improved the performance of the variance method somewhat, although the noise contributed by the ozone sensor appeared

at a wide range of frequencies. Previous studies (Wesely, 1988; Padro et. al., 1992) that reported some success with the variance method for measuring ozone fluxes used less noisy ozone sensors.

4.5 Gradient method

Ozone fluxes were also measured using the flux-gradient method. The vertical gradient of ozone was measured using one sensor, sampling alternately at two levels (as discussed in Chapter 2.5).

Fluxes were calculated using a form of the gradient method expressed by Berkowicz and Prahm (1982):

$$\overline{w'O_3'} = -ku_*\Delta C\left[\ln\left(\frac{z_2}{z_1}\right) - \Psi_h\left(\frac{z_2}{L}\right) + \Psi_h\left(\frac{z_1}{L}\right)\right] \qquad (4.7)$$

where z_1 and z_2 are lower and upper measurement heights and ΔC is the concentration difference between the two heights. Ψ_h is the integrated form of the diabatic correction function for heat transfer. Measured (eddy correlation) values of u_* and L were used in the calculations.

Gradient and eddy correlation fluxes are compared in Figure 4.6. The flux-gradient measurements are scattered widely around the eddy correlation measurements. There are both large overestimates and underestimates of the flux, relative to the eddy correlation measurements. Overall the flux-gradient method tends to overestimate ozone fluxes.

The chief sources of error for flux-gradient calculations are uncertainty in measurements of the ozone gradient, uncertainties in eddy correlation measurements of u_*, $\overline{w'T'}$ and hence L, uncertainty in the aerodynamic displacement height, and uncertainty in the similarity formulas themselves.

Figure 4.6: Comparison of gradient and eddy correlation measurements of ozone fluxes. The straight line is the 1:1 line. Triangles are late evening (stable atmosphere) measurements.

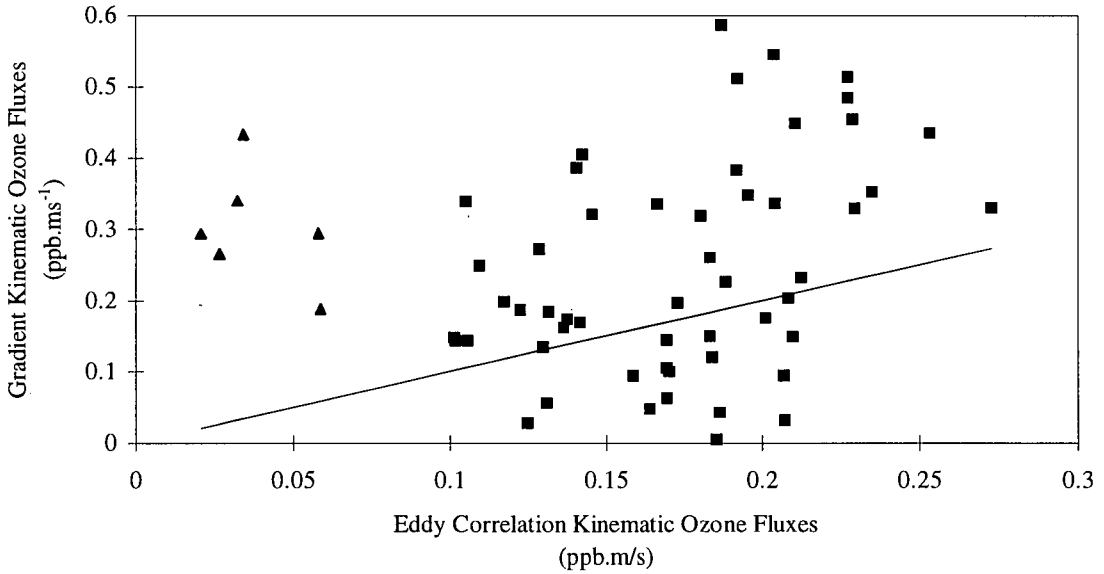

Additional uncertainty arises from the use of similarity functions for heat transfer for ozone transfer. This seems to be the explanation for the especially poor performance of the gradient measurements in late evening. In these conditions the assumption of similarity of heat and ozone transport does not hold well.

The method used to measure ozone gradients was susceptible to fairly large errors, and was probably responsible for some of the scatter of the flux-gradient measurements.

In Appendix B.2 the expected uncertainties in the gradient measurements due solely to the method of alternate sampling at 10 minute intervals is estimated to be about 25%, independent of any inaccuracy of the ozone monitor.

It seems probable that upwind fetch at the field site may not have been adequate for the upper gradient intake. This supposition is supported by the fact that systematic differences between the flux-gradient and eddy correlation measurements are apparent on different days of measurement. These differences may have been related to differences in wind direction and wind speed between days.

Although the instrumental setup used to measure ozone gradients did not produce precise measurements of ozone deposition, a similar setup may have some utility for longer term monitoring of deposition, where low maintenance ozone sensors with stable characteristics would be needed. The use of only one sensor to measure ozone gradients allows a less exact calibration of the instrument than would be required if two or more sensors were used. If the sampling interval at each height could be reduced, then the error contributed by the method of alternate sampling could be greatly reduced.

5. SUMMARY, CONCLUSIONS AND RECOMMENDATIONS

5.1 Summary and conclusions

Eddy correlation measurements of surface-layer ozone fluxes were taken on eight days during August, 1994. The field site was a grassland area at Pitt Meadows Airport, located in the Lower Fraser Valley, British Columbia. Measurements were taken through the afternoon and early evening hours.

The OSB-2 rapid-response ozone sensor used for these measurements was a modified version of the sensor described by Gusten et al. (1992). The sensor was estimated to have a 90% response time of roughly 1 second on the basis of attenuation observed in the spectrum of ozone concentration variations and in the ozone flux cospectrum. This response time is somewhat slower than that normally recommended for scalar flux measurement (Kaimal and Finnigan, 1994). To compensate for the loss of high frequency covariance, a correction was applied to the measured fluxes based on an assumption of cospectral similarity with sensible heat flux. The magnitude of this correction ranged up to 12%, with an average value of 5%.

The sensitivity of the ozone sensor was found to decrease somewhat with time, particularly during sampling periods with low ozone concentration. For this reason continuous calibration of the rapid response sensor with an accurate ozone monitor was required.

Surface resistances to ozone deposition were calculated using measured values of $\overline{w'O_3'}$, u_* and H. Uncertainty in the resulting values of surface resistance was estimated to

range between 15 and 25% except for a few evening periods which had greater uncertainty. The mean afternoon value of surface resistance was 175 sm^{-1}, slightly higher than values of surface resistance over grassland presented by Colbeck and Harrison (1985) and Galbally and Roy (1980).

Surface resistance generally increased slowly throughout the afternoon hours, then increased sharply in the evening. The afternoon rise in surface resistance was attributed to the effect of water stress and declining light levels on stomatal resistance. The sharp evening rise was attributed to stomatal closure due to falling light levels. Similar, though less marked diurnal patterns of surface resistance were found over vegetated surfaces by Stocker et al. (1993) and Wesely et al. (1978).

Some of the variability of surface resistance between measurement days was attributed to the effect, on stomatal resistance, of changes in atmospheric humidity and soil moisture.

Surface resistances calculated from the measurements were compared to surface resistances calculated using the parameterization described by Wesely (1989). W89 underestimated surface resistance throughout the day. The greatest underestimate was during mid-afternoon and evening, when W89 underestimated surface resistance by as much as 55%. One other test of W89 (Padro et al., 1994) also found a substantial underestimate of surface resistance during the late afternoon hours.

Two probable causes were identified for the underestimate of surface resistance by W89:

1) It is likely that resistance to ground surface deposition for the rangeland category was too low for the relatively tall (1.5 m) grass found at the field site. When resistance along the ground deposition pathway was increased from 300 sm^{-1} to 700 sm^{-1}, the agreement between model and measurements improved significantly, especially during early afternoon and late evening.
2) W89 does not include the effect of moisture stress and atmospheric humidity on stomatal resistance. This lack may account for some of the remaining underestimate during mid afternoon when both moisture stress and vapour density deficit are typically greatest.

The underestimate of surface resistance by W89 has implications for photochemical modelling efforts underway in the Lower Fraser Valley. If this situation is prevalent throughout the valley, then the model will overestimate deposition by a factor of 15 - 60% through the afternoon hours. This could result in the maximum predicted concentrations being underestimated by 4 - 8 ppb. The timing of maximum ozone concentration predicted by the model could also be in error. A smaller than predicted depositional sink for ozone could result in ozone build-up continuing later into the day. Finally the overestimate of deposition could also affect the location of maximum ozone build-up predicted by the model. Ozone may be advected further, in higher concentrations, if losses to surface deposition are less than predicted by the model.

Eddy correlation measurements of ozone fluxes were compared to fluxes derived using a method of cospectral similarity, similar to that described by Hicks and McMillen (1988). This method relies on an assumption of similarity between the vertical transport

of heat and ozone in the surface layer. The cospectral method allows flux measurements to be taken with more slowly responding sensors than is possible using the eddy correlation method. The cospectral method worked very well during unstable daytime conditions, producing accurate estimates of ozone flux with simulated instrument response times as long as 30 - 60 seconds. Precision of the method decreased for increased instrument response times. The method performed poorly in stable and unstable conditions.

For many trace gases, sensors, with sufficiently rapid response times for traditional eddy correlation techniques, do not exist. The cospectral method shows promise as a tool for measurement of these fluxes.

Cospectra of ozone and sensible heat flux presented in Chapter 4.3 tend to support the assumption of similarity of transport between ozone and sensible heat during unstable conditions. Differences between the two cospectra at high and low frequencies are due to the characteristics of the ozone sensor, rather than systematic differences in transport.

Ozone fluxes were calculated using a form of the variance method. Fluxes estimated using this method tended to overestimate the true fluxes due to extra variance contributed by high frequency instrumental noise and unexplained low frequency variations in ozone concentration. In contrast, the eddy correlation and cospectral methods are both relatively immune to this source of bias since high frequency noise and low frequency concentration variations are in general uncorrelated with vertical velocity. The type of ozone sensor used in this experiment produces too great a proportion of

instrumental noise, particularly at the low ozone concentrations seen in this study, for the variance method to be a reliable technique of flux measurement.

Measurements of ozone fluxes were also taken using the flux gradient method. Ozone gradients were measured using an ultraviolet absorption ozone monitor, sampling sequentially at two levels. Results from this technique showed a great deal of scatter relative to eddy correlation measurements. In particular, gradient measurements taken during stable or neutral conditions when heat and ozone transport are poorly correlated greatly overestimated the ozone fluxes. However even measurements taken during unstable conditions were widely scattered around the eddy correlation measurements.

The method of measuring the gradients introduced a substantial uncertainty into the calculations, accounting for some of the scatter in the results. It is also thought that the upper sampling intake may have had inadequate fetch during some sampling periods. This hypothesis is supported by the fact that gradient measurements on each given day tend to be clustered together, possibly due to different fetch on different days.

Although the gradient measurements were not particularly successful in this study the sampling technique used could have some promise for long term monitoring of ozone deposition since it requires only one highly precise (but not necessarily accurate) ozone monitor. The method is not particularly sensitive to a moderate amount of calibration drift of the ozone sensor since the difference in concentration could still be measured with a high degree of accuracy. As discussed in Appendix B.2, determination of the gradient becomes more accurate if switching between levels is made more rapid, assuming the sensor is capable of the more rapid sampling rate.

5.2 Recommendations

On the basis of the results of this study some recommendations and suggestions for further study may be made:

- The results of UAM runs should be carefully interpreted in light of the results from this study. Potential exists for significant underestimation of ozone levels by the model as well as in the timing .and location of maximum ozone concentrations.
- Further measurements of ozone deposition combined with detailed measurement of moisture parameters such as humidity, soil moisture and water vapour flux could better define the effect of water stress on surface resistance.
- A method for incorporating the effects of water stress and humidity into the deposition module of the UAM should be investigated. Soil moisture and humidity are both variables included in the RAMS model so these variables are available across the modelling domain.
- A prevalent surface type in the LFV is second growth forest of predominantly Douglas Fir and Western Hemlock. No measurements of ozone deposition have been taken to this surface type before. It would be useful to measure surface resistance over this surface type and compare it to model predictions.

BIBLIOGRAPHY

Adams, R. M., Glyer, J. D., Johnson, S. L., & McCarl, B. A., (1989). A reassessment of the economic effects of ozone on U.S. agriculture. *Journal of the Air and Waste Management Association*, **39**(7), 960-968.

Baldocchi, D. D., Hicks, B. B., & Camara, P., (1987). A canopy stomatal resistance model for gaseous deposition to vegetated surfaces. *Atmospheric Environment*, **21**(1), 91-101.

Banta, R. M., Olivier, L. D., Zhu, C. -J., Anlauf, K. J., Wiebe, H. A., Bottenheim, J. W., Steyn, D. G., McKendry, I. G., Biesenthal, T. & Shepson, P. B., (1996). Nocturnal cleansing in a tributary valley. *Atmospheric Environment* (in press).

Bates, D. V., (1994). The effect of photochemical air pollution on people. In D. J. McKee (Ed.), Tropospheric Ozone: Human Health and Agricultural Impacts (pp. 225-238). *CRC Press*, Boca Raton.

Bates, D.V., (1995a). Ozone: A review of recent experimental, clinical and epidemiological evidence, with notes on causation, Part 1. *Can. Respiratory Journal*, **2**(1), 1995, 25-31.

Bates, D.V., (1995b). Ozone: A review of recent experimental, clinical and epidemiological evidence, with notes on causation, Part 2. *Can. Respiratory Journal*, **2**(3), 1995, 161-171.

Bendat, J. S. & Piersol, A. G., (1986). Random Data - Analysis And Measurement Procedures. *Wiley Interscience*, New York, 566 pp.

Berkowicz, R., & Prahm, L. P., (1982). Evaluation of the profile method for estimation of surface fluxes of momentum and heat. *Atmospheric Environment*, **16**(12), 2809-2819.

Brauer, M. & Brook, J. R., (1996). Ozone personal exposures and health effects for selected groups residing in the Lower Fraser Valley, B.C. *Atmospheric Environment* (in press).

Broder, B., Dutsch, H. U., & Graber, W., (1981). Ozone fluxes in the nocturnal planetary boundary layer over hilly terrain. *Atmospheric Environment*, **15**(7), 1195-1199.

Broder, B., & Gygax, H. A., (1985). The influence of locally induced wind systems on the effectiveness of nocturnal dry deposition of ozone. *Atmospheric Environment*, **19**(10), 1627-1637.

Businger, J. A., (1986). Evaluation of the accuracy with which dry deposition can be measured with current micrometeorological techniques. *Journal of Climate and Applied Meteorology*, **25**, 1100-1124.

Colbeck, I., & Harrison, R. M., (1985). Dry deposition of ozone: Some measurements of deposition velocity and of vertical profiles to 100 metres. *Atmospheric Environment*, **19**(11), 1807-1818.

Comrie, A. C., (1990). The climatology of surface ozone in rural areas: A conceptual model. *Progress in Physical Geography*, **14**(3), 295-316.

Crutzen, P. J., (1987). Tropospheric ozone: An overview. In I. S. A. Isaksen (Ed.), Tropospheric Ozone: Regional and Global Scale Interactions (pp. 3-32). *D. Reidel*, Dordrecht.

Dabberdt, W. F., Lenschow, D. H., Horst, T. W., Zimmerman, P. R., Oncley, S. P., & Delany, A. C., (1993). Atmosphere-surface exchange measurements. *Science*, **260**, 1472-1480.

Delany, A. C., Fitzjarrald, D. R., Lenschow, D. H., Pearson Jr., R., Wendel, G. J., & Woodruff, B., (1986). Direct measurements of nitrogen oxides and ozone fluxes over grassland. *Journal of Atmospheric Chemistry*, **4**, 429-444.

Droppo Jr., J. G., (1985). Concurrent measurements of ozone dry deposition using eddy correlation and profile flux methods. *Journal of Geophysical Research*, **90**(D1), 2111-2118.

Dyer, A. J., (1974). A review of flux profile relationships. *Boundary-Layer Meteorology*, **7**, 363-372.

Environment Canada, (1994). National urban air quality trends 1981-1990. Report EPS 7/UP/4, *Environment Canada*, Ottawa

Finlayson-Pitts, B. J., & Pitts, J. N., (1993). Atmospheric chemistry of tropospheric ozone formation: Scientific and regulatory implications. *Journal of Air and Waste Management Association*, **43**(August), 1091-1100.

Fitzjarrald, D.R., & Lenschow, D.H., (1983). Concentrations and mean flux profiles for chemically reactive trace species in the atmospheric surface layer. *Atmospheric Environment*, **17**(12), 2505-2512.

Galbally, I. E., (1971). Ozone profiles and ozone fluxes in the atmospheric surface layer. *Quarterly Journal of the Royal Meteorological Society*, **97**, 18-29.

Galbally, I. E., & Roy, C. R., (1980). Destruction of ozone at the earth's surface. *Quarterly Journal of the Royal Meteorological Society, Soc.*, **106**, 599-620.

Garland, J. A., & Derwent, R. G., (1979). Destruction at the ground and the diurnal cycle of concentration of ozone and other gases. *Quarterly Journal of the Royal Meteorological Society*, **105**, 169-183.

Garland, J. A., & Penkett, S. A., (1976). Absorption of peroxy acetyl nitrate and ozone by natural surfaces. *Atmospheric Environment*, **10**, 1127-1131.

Gesellschaft für angewandte Systemtechnik (GFAS), (1994). Ozone sonde - OSB-2: Operation manual. Version 1.0.

GFAS, (1994). Personal communication.

Godowitch, J. M., (1990). Vertical ozone fluxes and related deposition parameters over agricultural and forested landscapes. *Boundary-Layer Meteorology*, **50**, 375-404.

Greater Vancouver Regional District, (1994). GVRD air quality management plan. *GVRD*, Burnaby.

Greenhut, G. K., (1983). Resistance of a pine forest to ozone uptake. *Boundary-Layer Meteorology*, **27**, 387-391.

Guicherit, R., (1987). Ozone on the urban and regional scale with special reference to the situation in the Netherlands. In I. S. A. Isaksen (Eds.), Tropospheric Ozone: Regional and Global Scale Interactions (pp. 49-62). *D. Reidel*, Dordrecht.

Gusten, H., Heinrich, G., Schmidt, R. W. H., & Schurath, U., (1992). A novel ozone sensor for direct eddy flux measurements. *Journal of Atmospheric Chemistry*, **14**, 73-84.

Heck, W. W., (1982). Assessment of crop loss from ozone. *Journal of the Air Pollution Control Association*, **32**(4), 353-361.

Hicks, B. B., Baldocchi, D. D., Hosker, R. P., Hutchinson, B. A., Matt, D. R., McMillen, R. T., & Satterfield, L. C., (1985). On the use of measured concentrations to infer dry deposition (*NOAA Technical Memorandum No. ERL ARL-141*). NOAA.

Hicks, B. B., & McMillen, R. T., (1988). On the measurement of dry deposition using imperfect sensors and in non-ideal terrain. *Boundary-Layer Meteorology*, **42**, 79-94.

Jacob, D. J., Fan, S. M., Wofsy, S. C., Spiro, P. A., Bakwin, P. S., Ritter, J. A., Browell, E. V., Gregory, G. L., Fitzjarrald, D. R., & Moore, K. E., (1992). Deposition of ozone to tundra. *Journal of Geophysical Research*, **97**(D15), 16473-16479.

Jarvis, P.G., & Morrison, J.I.L., (1981). The control of transpiration and photosynthesis by the stomata. in P.G. Jarvis and T.A. Mansfield (Eds.), Stomatal Physiology (pp. 248-279), *Cambridge University Press*, Cambridge

Kaimal, J.C., (1972). Turbulence spectra, length scales and structure parameters in the stable surface layer. *Boundary-Layer Meteorology*, **4**, 289-309.

Kaimal, J. C., (1986). Flux and profile measurements from towers in the boundary layer. in D.H. Lenschow (Ed.), Probing the Atmospheric Boundary Layer (pp. 19-28). *American Meteorological Society*, Boston.

Kaimal, J. C., & Finnigan, J. J., (1994). Atmospheric Boundary Layer Flows - Their Structure and Measurement. *Oxford University Press*, Oxford.

Lee, X. & Black, T.A., (1994). Relating eddy correlation sensible heat flux to horizontal sensor separation in the unstable atmospheric surface layer. *Journal of Geophysical Research*, **99**(D9), 18545-18553.

Lenschow, D. H., & Delany A.C., (1987). An analytic formulation for NO and NO_2 flux profiles in the atmospheric surface layer. *Journal of Atmospheric Chemistry*, **5**, 301-309.

Lenschow, D. H., & Kristensen, L., (1985). Uncorrelated noise in turbulence measurements. *Journal of Atmospheric and Oceanic Technology*, **2**, 68-81.

Lenschow, D. H., Pearson Jr., R., & Stankov, B. B., (1982). Measurements of ozone vertical flux to ocean and forest. *Journal of Geophysical Research*, **87**(C11), 8833-8837.

Lippman, M., (1989). Health effects of ozone: A critical review. *Journal of the Air and Waste Management Association*, **39**, 672-695.

Losch, R & Tenhunen, J.D., (1981). Stomatal response to humidity - phenomenon and mechanism. in P.G. Jarvis and T.A. Mansfield (Eds.), Stomatal Physiology (pp. 248-279), *Cambridge University Press*, Cambridge

MacPherson, J. I., Schmidt, R. W. H., Jochum, A. M., Pearson Jr., R., Neumann, H. H., & den Hartog, G., (1993). Ozone flux measurement on the NRC Twin Otter during the 1991 California ozone deposition experiment. In Eighth Symposium on Meteorological Observations and Instrumentation, Preprint volume (pp. 490-495). *American Meteorological Society*, Boston.

Mahrt, L., MacPherson, J. I., & Desjardins, R., (1994). Observations of fluxes over heterogeneous surfaces. *Boundary-Layer Meteorology*, **67**, 345-367.

Mansfield, T.A., Travis, A.J., & Jarvis, R.G., (1981). Responses to light and carbon dioxide. in P.G. Jarvis and T.A. Mansfield (Eds.), Stomatal Physiology (pp. 248-279), *Cambridge University Press*, Cambridge

Massman, W. J., Pederson, J., Delany, A., Grantz, D., den Hartog, G., Neumann, H. H., Oncley, S. P., Pearson, R. & Shaw, R. H., (1994). An evaluation of the regional acid deposition model surface module for ozone uptake at three sites in the San Joaquim Valley of California. *Journal of Geophysical Research*, **99**(D4), 8281-8294.

McCurdy, T. R., (1994). Concentrations of ozone in the lower troposphere (ambient air). In D. J. McKee (Ed.), Tropospheric Ozone: Human Health and Agricultural Impacts (pp. 19-37). *CRC Press* Boca Raton.

McKendry, I. G., Steyn, D. G., Lundgren, J., Hoff, R. M., Strapp, W., Anlauf, K., Froude, F., Martin, B. A., Banta, R. M., & Olivier, L. D., (1996a). Elevated polluted layers and vertical down-mixing over the Lower Fraser Valley, B.C. *Atmospheric Environment* (in press).

McKendry, I. G., Steyn, D. G., Banta, R. M., Strapp, W. M., Anlauf, K., & Pottier, J., (1996b). Daytime air quality and local circulations in the Pitt Lake tributary valley, B.C. *Atmospheric Environment* (in press).

Monitor Labs, (1993). ML 9811 ozone analyzer with IZS: Operator manual.

Monteith, J. L. & Unsworth, M. H., (1990). Principles of Environmental Physics, 2nd ed. *Edward Arnold*, London, 291 pp.

National Research Council (1992). Rethinking The Ozone Problem In Urban And Regional Air Pollution. *National Academy Press*, Washington, 500 pp.

Neubert, A., Kley, D., Wildt, J., Segschneider, H.J., & Forstel, H., (1993). Uptake of NO, NO_2, O_3 by sunflower and tobacco plants: Dependence on stomatal conductivity. *Atmospheric Environment*, **27**(A), 2137-2145.

Oke, T. R., (1987). Boundary Layer Climates, 2nd ed. *Routledge*, London, 435 pp.

Oke, T. R. & Hay, J. E., (1994). The Climate Of Vancouver. B.C. Geographical Series, No. 50, *Department of Geography*, University of British Columbia, 84 pp.

Padro, J., (1993). Seasonal contrasts in modeled and observed dry deposition velocities O_3, SO_2 and NO_2 over three surfaces. *Atmospheric Environment*, **27**, 807-814.

Padro, J., den Hartog, G. & Neumann, H. H., (1991). An investigation of the ADOM dry deposition module using summertime O_3 measurements above a deciduous forest. *Atmospheric Environment*, **25**, 1689-1704.

Padro, J., den Hartog, G., Neumann, H. H., & Woolridge, D., (1992). Using measured variances to compute surface fluxes and dry deposition velocities: A comparison with measurements from three surface types. *Atmospheric-Ocean*, **30**(3), 363-382.

Padro, J., Massman, W. J., den Hartog, G., Neumann, H. H., (1994). Dry deposition velocity of O_3 over a vineyard obtained from models and observations: The California Ozone Deposition Experiment. *Water, Air and Soil Pollution*, **68**, 325-339.

Pearcy, R.W. (1989). Radiation and light measurements. In Pearcy, R.W. and Ehleringer, J., Mooney, H.A. & Rundel, P.W. (Eds.), Plant Physiological Ecology (pp. 97-116). *Chapman and Hall*, London.

Pielke, R. A., Cotton, W. R., Walko, R. L., Tremback, C. J., Lyons, W. A., Grasso, L. D., Nicholls, M. E., Moran, M. D., Wesley, D. A., Lee, T. J., & Copeland, J. H., (1992). A comprehensive meteorological modelling system - RAMS. *Meteorology and Atmospheric Physics*, **49**, 69-91.

Press, W.H., Teukolsky, S.A., Vetterling, W.T. & Flannery, B.P., (1992). Numerical Recipes in FORTRAN, Second Edition. *Cambridge University Press*, Cambridge, 963 pp.

Pryor, S. C., & Steyn, D. G., (1995). Hebdomadal and diurnal cycles in ozone time series from the Lower Fraser Valley, B.C. *Atmospheric Environment*, **29**(9), 1007-1019.

Regener, V. H., (1957). The vertical flux of atmospheric ozone. *Journal of Geophysical Research*, **62**(2), 221-228.

Robeson, S. M., (1990). Evaluation and comparison of statistical forecast models for daily maximum ozone concentrations. *Atmospheric Environment*, **24B**(2), 303-312.

Roth, M., (1988). Spectral analysis of turbulence in an unstable suburban atmosphere. *M.Sc. Thesis*, University of British Columbia.

Steyn, D. G., Bottenheim, J. W., & Thomson, R. B., (1996). Overview of tropospheric ozone in the Lower Fraser Valley, and the Pacific 93 Field Study. *Atmospheric Environment* (in press).

Steyn, D. G., & Faulkner, D. A., (1986). The climatology of sea-breezes in the Lower Fraser Valley, B.C. *Climatological Bulletin*, **20**(3), 21-39.

Steyn, D.G., & Oke T.R., (1982). The depth of the daytime mixed layer at two coastal sites: A model and its validation. *Boundary-Layer Meteorology*, **25**, 161-180.

Steyn, D. G., Roberge, A. C., & Jackson, C., (1990). Anatomy of an extended air pollution episode in British Columbia's Lower Fraser Valley. Final report prepared under contract to the B.C. Ministry of the Environment, March 1990.

Stocker, D. W., Stedman, D. H., Zeller, K.F., Massman, W.J., & Fox, D.G., (1993). Fluxes of nitrogen oxides and ozone measured by eddy correlation over a shortgrass prairie. *Journal of Geophysical Research*, **98**, 12619-12630.

Stocker, D. W., Zeller, K. F., & Stedman, D. H., (1995). O_3 and NO_2 Fluxes over snow by eddy correlation. *Atmospheric Environment*, **29**(11), 1299-1305.

Stull, Roland B., (1988). An Introduction to Boundary Layer Meteorology. *Kluwer*, Dordrecht, 666 pp.

Systems Application International, (1995). User's guide to the variable-grid urban airshed model (UAM-V). Report No. Sysapp-95/027

Voogt, J. A., (1989). Validation of an urban canyon radiation model for nocturnal long-wave radiative fluxes and the effects of surface geometry on cooling in urban canyons. *PhD. Thesis*, University of British Columbia.

Vukovich, F. M., & Fishman, J., (1986). The climatology of summertime O3 and SO2 (1977-1981). *Atmospheric Environment*, **20**(12), 2423-2433.

Wesely, M. L., (1981). Field measurement of small ozone fluxes to snow, wet bare soil, and lake water. *Boundary-Layer Meteorology*, **20**, 459-471.

Wesely, M. L., (1988). Use of variance techniques to measure dry air-surface exchange rates. *Boundary-Layer Meteorology*, **44**, 13-31.

Wesely, M. L., (1989). Parameterization of surface resistances to gaseous dry deposition in regional-scale numerical models. *Atmospheric Environment*, **23**(6), 1293-1304.

Wesely, M. L., Eastman, J. A., Cook, D. R., & Hicks, B. B., (1978). Daytime variations of ozone eddy fluxes to maize. *Boundary-Layer Meteorology*, **15**, 361-373.

Wright, E. F., (1988). The effect of ozone on horticultural crops important in the Fraser Valley, B.C. *M.Sc. Thesis*, University of British Columbia.

Wyngaard, J. C., (1990). Scalar fluxes in the planetary boundary layer - theory, modeling, and measurement. *Boundary-Layer Meteorology*, **50**, 49-75.

APPENDIX A : CORRECTION FOR OSB-2 FREQUENCY RESPONSE

The OSB-2 ozone sensor was claimed to have a 90% response time of 0.1 second (Gusten et al., 1992). However, inspection of the composite ozone - vertical velocity cospectrum (Figure 4.3) and the ozone spectrum (Figure 4.5) suggest the actual response time was closer to one second.

No other explanation for the rapid falloff ($> f^{-4/3}$) of the ozone - vertical velocity cospectrum seems feasible. Attenuation of the vertical velocity signal at high frequencies is not possible given the very rapid transit time of sound pulses across the measurement gap of the sonic anemometer. It seems unlikely, for a number of reasons, that the ozone flux cospectrum should decrease more rapidly than the (sensible) heat flux cospectrum in the inertial subrange. First, there is the striking similarity of the heat and ozone flux cospectra at lower frequencies. It seems reasonable that this similarity should extend into the inertial subrange. Second, isotropic turbulence in the inertial subrange should transport all scalar quantities equally, so there is no physical basis on which to explain a more rapid falloff of the ozone flux cospectrum. The heat flux cospectrum decreases proportional to 4/3 power of frequency as expected.

Because of its 1 second response time, ozone fluxes measured using the OSB-2 sensor systematically underestimated the true fluxes. The most rapid variations in ozone concentration were not fully recorded by the sensor.

A correction for this effect was applied to the measured ozone fluxes. The method of correction was the same as that described in Chapters 4.1 and 4.2. Assuming

cospectral similarity between heat and ozone flux, Equation 4.4 can be used to estimate the flux correction needed. Heat- and ozone-vertical velocity covariances were filtered with a band-pass of 0.5 Hz, as below that frequency the two cospectra were very similar. The ratio between band-pass covariances was assumed to equal the ratio between the heat flux and the true ozone flux. The resulting corrections to the ozone fluxes are shown in Table A.1.

For unstable atmosphere cases corrections for the sensor frequency response ranged from 1 to 12%, with an average of 5%.

For the stable and neutral atmosphere measurements, the assumption of cospectral similarity held rather poorly (as discussed in Chapters 4.2 and 4.3) so the above procedure was not used to correct these ozone fluxes. For these cases a correction of 10% was assumed. This is near the upper end of the range of corrections needed for the unstable cases. Frequency corrections for the neutral and stable cases should be at least as great as for the unstable cases, since a higher proportion of flux is carried by small eddies in stable atmospheres. Since measurements for stable and neutral cases had quite high uncertainty, a more exact correction was not felt necessary.

The ozone flux cospectrum also diverged from the heat flux cospectrum at low frequencies - possibly due to the effect of humidity on the sensitivity of the sensor. The same type of correction was calculated to account for this effect. This correction turned out to be very small and was not applied to the measured fluxes.

The individual cospectra were investigated to see whether there was any systematic change in sensor response time through the measurement periods. No such effect was found.

Table A.1: Corrections to measured ozone fluxes due to the OSB-2 frequency response.

Date	Time (PDT)	Correction Factor		Date	Time (PDT)	Correction Factor
10	1625	1.02		27	1424	1.04
10	1657	1.07		27	1446	1.04
11	1522	1.04		27	1515	1.01
11	1558	1.06		27	1545	1.04
11	1629	1.12		27	1645	1.04
11	1745	1.1		27	1715	1.07
11	1817	1.1		27	1745	1.1
11	1848	1.1		27	1815	1.1
12	1641	1.06		27	1846	1.1
12	1712	1.05		27	1902	1.1
12	1743	1.08		27	1934	1.1
12	1813	1.09		30	1151	1.05
13	1234	1.04		30	1221	1.05
13	1315	1.04		30	1301	1.03
13	1348	1.03		30	1332	1.01
13	1420	1.06		30	1408	1.06
13	1451	1.03		30	1449	1.07
13	1521	1.04		30	1519	1.06
13	1553	1.03		30	1550	1.06
13	1624	1.03		30	1620	1.05
13	1655	1.03		30	1651	1.06
13	1726	1.04		30	1721	1.05
13	1759	1.05		30	1751	1.07
14	1120	1.06		30	1821	1.1
14	1150	1.07		30	1853	1.1
14	1222	1.09		31	1150	1.03
14	1253	1.06		31	1220	1.05
14	1325	1.08		31	1250	1.04
14	1357	1.11		31	1320	1.06
14	1427	1.09		31	1350	1.04
14	1459	1.05		31	1351	1.04
14	1530	1.05		31	1421	1.06
14	1600	1.09		31	1453	1.04
14	1630	1.05		31	1523	1.07
27	1259	1.04				

APPENDIX B : OZONE SENSORS - CALIBRATION AND UNCERTAINTIES

B.1 OSB-2 ozone sensor

The OSB-2 sensor is pictured, mounted on the instrument tower, in Figure 2.5. The operating principle and characteristics of the sensor are described in detail by Gusten et al., 1992, and outlined briefly in Chapter 2.5 of this thesis.

Before each day of use, the OSB-2 required "ozonization" in order to activate the chemiluminescent dye that forms the basis for ozone detection. Ozonization was achieved by passing ozone rich air (around 100 ppb) from an ozone generator through the sensor for a period of 30 minutes (GFAS, 1994).

Following ozonization the OSB-2 was calibrated. Calibration was accomplished by measuring voltage output from the OSB-2 for three different settings of the ozone generator. At the same time ozone concentration output from the ozone generator was measured using the ML9811 ozone monitor. The calibration coefficient for the OSB-2 was then derived by linear regression between voltage output and measured ozone concentration. A linear response and zero intercept for the OSB-2 calibration curve was assumed. Calibration was done over a range of ozone concentrations, from ambient ozone at time of calibration to roughly 120 ppb.

The dye coated discs used in the instrument have a finite life span. With use, the discs gradually lose sensitivity. The useful life span is estimated as 40 hours (Gusten, 1994). The disc was not changed through the course of this study (roughly 40 hours of

measurement). Some decrease in sensitivity was noted from beginning to end of the field program.

Over the course of a day of measurements the OSB-2 sensor gradually lost sensitivity as depicted in Figure B.1. Loss of sensitivity was particularly marked when ozone concentrations dropped to 25 ppb or below.

The decrease in sensitivity was compensated for by adjusting the calibration coefficient for each sampling period on the basis of ozone concentration measured by the ML9811 monitor.

Figure B.1: Ratio of ozone concentrations measured by the OSB-2 and the ML9811 on August 30th, 1994.

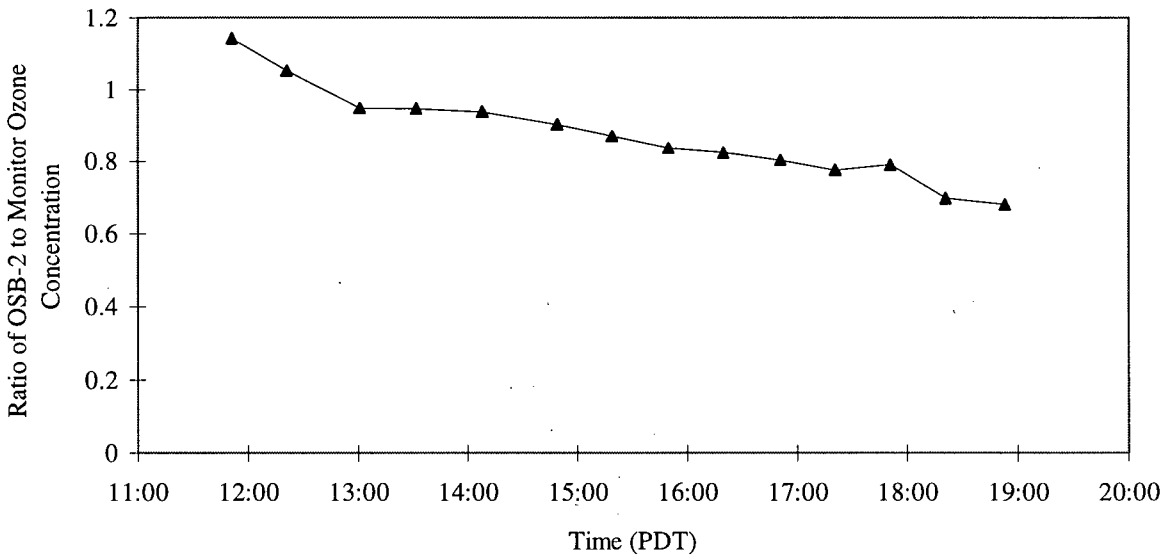

Accuracy of the OSB-2 sensor, after correction for sensitivity loss, was estimated to be roughly 5%. Some of this error arises from the different averaging periods used for the OSB-2 and ML9811 data collection. It was necessary to do some interpolation of the

ML9811 data in order to derive average ozone concentration over the OSB-2 sampling periods Another small source of error was the necessity to average between the two ML9811 measurement heights in order to estimate ozone concentration at the level of the OSB-2.

B.2 Gradient sampling system

Vertical gradients of ozone were measured using one sensor sampling alternately at two levels. This method of measurement introduces uncertainty into the gradient even if the sensor is perfectly accurate. Uncertainty arises because the ozone concentration is constantly varying at a wide variety of time scales. To derive the gradient from this method of measurement it is necessary to interpolate between successive measurement periods at each level to obtain a 'measurement' of ozone concentration at both levels for each time period.

In the present study the monitor sampled for 10 minutes at each level. The 10 minute time period was chosen to allow the slowly responding ($T_{90} \approx 1$ minute) ozone monitor to fully equilibrate.

Uncertainty in the gradient measurements due to the method of alternate sampling was estimated using time series from the rapid-response ozone sensor. Twenty sets of 10 minute samples, each shifted slightly in time were taken from each series. The standard deviation of these samples was assumed to represent the uncertainty in the gradient measurements.

Figure B.2 shows estimated uncertainty in the gradients for a range of sampling time from 1 to 10 minutes. Increased accuracy for more rapid sampling comes about because the greater number of samples at each level are more likely to be representative. Also, interpolation of concentration between samples at each level is more accurate over shorter time periods.

The 0.4 ppb average uncertainty corresponds to a 25% error in the gradient on average, though there is a fairly wide range of expected uncertainties, depending on the magnitude of the gradient.

Figure B.2: Expected uncertainty in gradient measurement versus sampling interval

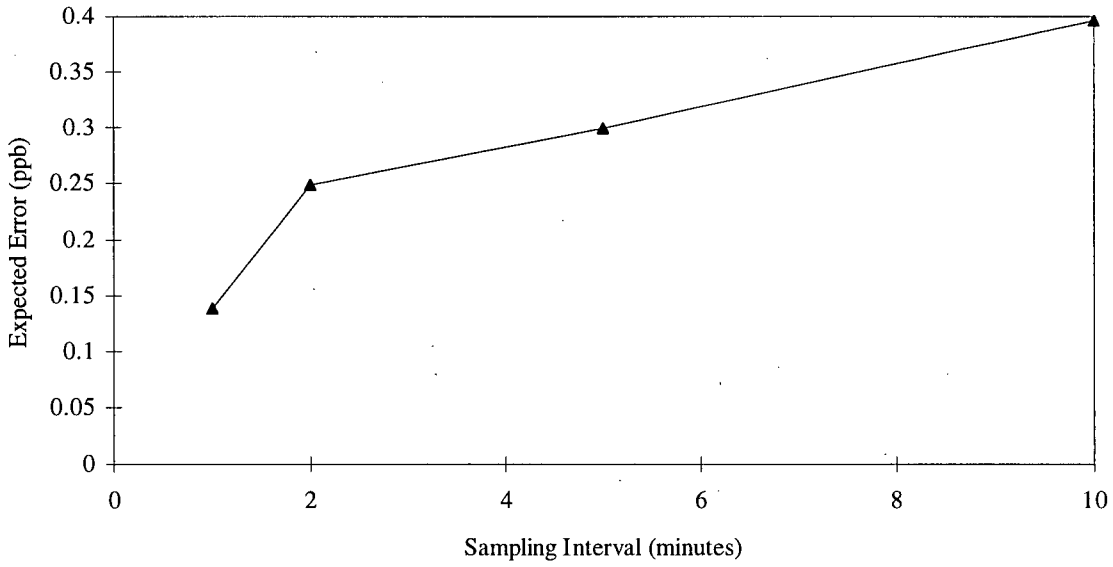

APPENDIX C : SPLUS ROUTINES USED IN ANALYSIS

Several of the routines used in the data analysis are provided here for reference. In S-plus code the # symbol opens comment lines, the + symbol is a command continuation symbol. The left and right braces, "{ "and "}" enclose loops or grouped statements.

C.1 ANALYSIS8.SP

```
# Imports data from all the sonic data files.
# Calculates basic summary statistics on the detrended,
# demeaned time series.
# Inputs atmospheric pressure and ozone calibration,
# lags to maximum correlation as well as mean [O3] from monitor.
# Outputs a summary file of the mean values, fluxes, resistances
# correlations etc.
#########################################################
# initialize constants
kk_0.4          # von Karman's
gg_9.82         # gravity
presr_101.3     # default pressure
RH_NA           # default RH
intercept_0     # default ozone calibration
stabil_0        # default ozone calibration
ht_1.5          # canopy height
dispht_0.7*ht   # displacement height
z0_.137         # roughness length
zmeas_4.85      # measurement height
month_8         # month number
stabilnam_c("stable","unstable")
fetchnam_c("good", "OK", "bad")
#########################################################
# read in file info from "datafiles"
ccc_scan("datafiles", list("",0,0,0,0,0,0,0,0,0))
# column 1 is filename
# column 2 is monitor O3
# column 4 is the lag to max wO3 correlation
# column 6 is the sonde calibration
# column 7 is the pressure
# column 8 is the Relative humidity
# column 9 is a sonde correction factor
# column 10 is a fetch quality descriptor ( 1=good, 2=soso, 3=bad)
cfn_ccc[[1]]
cmono3_ccc[[2]]
clagwo3_ccc[[4]]
cslope_ccc[[6]]
cpresr_ccc[[7]]
```

```
cRH_ccc[[8]]
ccorrectionfac_ccc[[9]]
cfetch_ccc[[10]]
nof_length(cfn)                          # number of files
############################################################
cat ("What output file name\n")
outfile_readline()
file1_paste(outfile,".part1",sep="")
sink(file1)
############################################################
# loop through all files
for (i in 1:nof)                         {
fn_cfn[i]                                # filename
fdate_substring(fn,1,2)                  # measurement date
starttime_substring(fn,5,8)              # measurement start time
fdate _ as.numeric(fdate); starttime _ as.numeric(starttime)
############################################################
# import u, v, w, T, O3
aaa_scan(fn, list(0,0,0,0,0))
uu_aaa[[1]]; vv_aaa[[2]]; ww_aaa[[3]]; cc_aaa[[4]]; o3r_aaa[[5]]
############################################################
# set file specific info
slope_cslope[fn==cfn]                    # slope of ozone sonde calibration
o3lag_clagwo3[fn==cfn]                   # lag of ozonesonde
fetch_cfetch[fn==cfn]                    # fetch descriptor
mono3_cmono3[fn==cfn]                    # monitor ozone concentration
presr_cpresr[fn==cfn]                    # atmospheric pressure
RH_cRH[fn==cfn]                          # relative humidity
corfac_1
correcfac_ccorrectionfac[fn==cfn]
if (correcfac<0.99||correcfac>1.01) {corfac_1/correcfac}      # sonde calibration correction
############################################################
o3p_(intercept+(slope*o3r)*corfac)                  # convert raw ozone data to ppb
ct_(1/403)*(cc/50)^2                                # convert speed of sound to temperature
meanu_mean (uu)/100; meanv_mean (vv)/100; meanw_mean (ww)/100
meanws2_mean((((uu)/100)^2 + ((vv)/100)^2)^(.5))    # actual mean wind
meanws_(meanu^2 + meanv^2)^0.5                      # mean net wind
meano3_mean (o3p); meant_mean (ct)
N_ length (uu)                                      # file length
ltime_ (N/10.5)/60                                  # file length (minutes)
if (fdate==10) {ltime_ltime/2}
############################################################
# detrend series
indx2_seq(1,N)
a1ww_(residuals(lsfit(indx2,ww))/100)
a1uu_(residuals(lsfit(indx2,uu))/100)
a1vv_(residuals(lsfit(indx2,vv))/100)
a1ct_residuals(lsfit(indx2,ct))
if ((!is.na(o3p[1]))) a1o3p_residuals(lsfit(indx2,o3p))else a1o3p_NA
############################################################
# calculate fluxes
ustar_(((var(a1uu,a1ww))^2)+(var(a1vv,a1ww))^2)^0.25
khf_var(a1ww,a1ct)
if ((!is.na(o3p[1]))) o3flux_var (a1ww[1:(N-o3lag)],a1o3p[(o3lag+1):N])
```

```
+ else o3flux_NA
o3mconc_meano3*101300*48/(8.3143*meant)/1000          # ozone concentration
o3mflux_o3flux*101300*48/(8.3143*meant)/1000          # ozone mass flux
############################################################
# calculate correlation coefficients
ccwt_cor (a1ww,a1ct)
if ((!is.na(o3p[1]))) ccwo3_cor (a1ww[1:(N-o3lag)],a1o3p[(o3lag+1):N])
+ else ccwo3_NA
if ((!is.na(o3p[1])))  ccto3_cor(a1ct[1:(N-o3lag)],a1o3p[(o3lag+1):N])
+ else ccto3_NA
############################################################
rho_presr*100/(287*meant)                             # density
heatflux_rho*1004*khf                                 # heatflux
L_(-1.0)*(meant*ustar^3)/(kk*gg*khf)                  # Obukhov length
MOP_(zmeas-dispht)/L                                  # stability parameter
############################################################
# resistance calculations
stabil[MOP>0]_1
stabil[MOP<0]_2
if (stabil==1 ) phih_(1+5*MOP) else phih_((1-16*MOP)^(-.5))
if (stabil==1) intphih_(-5*MOP) else intphih_(2*log((1+phih^(-1))/2))
depvel_(o3flux/meano3)
rah1_(1/(meanws2*kk^2))*(log((zmeas-dispht)/z0)-intphim)*
+(log((zmeas-dispht)/z0)-intphih)
rah2_((ustar*kk)^(-1))*(log((zmeas-dispht)/z0)-intphih)
rb_10.2*ustar^(1/3)*ustar^(-1)
rtot_abs(1/depvel)
rs_rtot-rah2-rb
############################################################
# output to file
outvec1_signif(c(fdate,starttime,N,ltime,fetch,meanu,meanv,meanw
+,meanws2,meanws,meant,meano3,o3mconc,rho,presr,RH,ustar,khf
+,heatflux,o3flux,o3mflux,o3grad,tgrad1),4)
cat (outvec1, "\n")
outvec2_signif(c(fdate,starttime,depvel,rtot,rah1,rah2,rb,rs,MOP
+,Kh,Ko3,ccwt,ccwo3,ccto3,corfac,fetch),4)
cat  (outvec2, "\n")                                  }
```

C.2 W89.SP

```
# uses output from ANALYSIS8.SP and produces W89 results
# the following lines list the data that are scanned in from the output
# files of analysis8.sp
# fdate,starttime,N,ltime,fetch,meanu,meanv,meanw,meanws2,meanws
# meant,meano3,o3mconc,rho,presr,RH,ustar,khf,heatflux,o3flux
# o3mflux,o3grad,tgrad1
# fdate,starttime,depvel,rtot,rah1,rah2,rb,rs,MOP,Kh,Ko3,ccwt
# ccwo3,ccto3,corfac,fetch
##########################################
# reads in data from analysis8.sp
eee_scan("oct6.p1",list(0,0,0,0,0,0,0,0,0,0,0,0,0,0,0,0,0,0,0,0,0,0,0,0))
```

```
ggg_scan("oct6.p2",list(0,0,0,0,0,0,0,0,0,0,0,0,0,0,0,0))
wfdate_eee[[1]];wstarttime_eee[[2]];wfetch_eee[[5]]
wmeanw_eee[[8]];wmeanws2_eee[[9]];wmeanws_eee[[10]]
wmeant_eee[[11]];wmeano3_eee[[12]];wo3mconc_eee[[13]]
wRH_eee[[16]];wustar_eee[[17]];wkhf_eee[[18]]
wheatflux_eee[[19]];wo3flux_eee[[20]];wo3mflux_eee[[21]]
wo3grad_eee[[22]];wtgrad1_eee[[23]]
wdepvel_ggg[[3]];wrtot_ggg[[4]];wrah1_ggg[[5]];wrah2_ggg[[6]]
wrb_ggg[[7]];wrs_ggg[[8]];wMOP_ggg[[9]];wKh_ggg[[10]];wKo3_ggg[[11]]
wccwt_ggg[[12]];wccwo3_ggg[[13]];wccto3_ggg[[14]];corfac_ggg[[15]]
##########################################
# reads in more data including shortwave radiation
qqq_scan("w89data1.txt",list(0,0,0,0,0,0,0,0,0))
# date, time, depvel, rtot, ra, rb, rs, sw, tsurf
qfdate_qqq[[1]];qstarttime_qqq[[2]];qrs_qqq[[7]]
qsw_qqq[[8]];qsurft_qqq[[9]]
# set W89 parameters
ri_120;rlu_2000;rac_c(100,500);rgs_200;rcl_1000
##########################################
# calculates w89 resistances
gooddata_c(1:39,41:60,63:72)
rw892_seq(1:(length(gooddata)))
rw893_seq(1:(length(gooddata)))
for (i in gooddata)                                    {
rstom_1.6*ri*(1+(200*(qsw[i]+.1)^(-1))^(2))*
+(400*(qsurft[i]*(40-qsurft[i]))^(-1))
rdc_100*(1+1000*(qsw[i]+10)^(-1))
rw89_((1/rstom)+(1/rlu)+(1/(rdc+rcl))+(1/(rac+rgs)))^(-1)
cat(qfdate[i],qstarttime[i],qrs[i],round(rw89,2),rstom,"\n")
rw892[i]_round(rw89[1],2)
rw893[i]_round(rw89[2],2)
                                                       }
```

C.3 COSPEC3.SP

```
# calculates wo and wt cospectra
# averages in exponential frequency bins and the averages between runs
# data import and flux calculation is the same as ANALYSIS8.SP
########################################
# initialize variables
gg_9.82; kk_0.4; stabil_0; intercept_0; N_18170; m_1
avercwt_array(0,dim=c(39,20)); avercwo_array(0,dim=c(39,20))
avernatfreq_array(0,dim=c(39,20)); averfreq_array(0,dim=c(39,20))
indx2_seq(1,N); indx_(seq(1,(N/2-1)))
freq_10.5*(1:(N/2-1))/N                                # all frequencies
freqint_freq[1]                                        # frequency interval
########################################
# loop through files and import data
for (i in c(21,23,24,32:36,43,46,56:58,60:62,72:75))           {
fn_cfn[i]
starttime _ substring(fn,5,8)
```

```
fdate _ as.numeric(fdate); starttime _ as.numeric(starttime)
aaa_scan(fn, list(0,0,0,0,0))
# truncate series to 29 minute length
uu_aaa[[1]][1:N]; vv_aaa[[2]][1:N]; ww_aaa[[3]][1:N]
cc_aaa[[4]][1:N]; o3r_aaa[[5]][1:N]
meanws_sqrt((mean(uu/100))^(2) + (mean(vv/100))^(2))
slope _cslope[fn==cfn]
o3lag _clagwo3[fn==cfn]
correcfac _ccorrectionfac[fn==cfn]
if (correcfac<.99){ corfac _1/correcfac}
o3p_(intercept+(slope*o3r)*corfac)
ct_(1/403)*(cc/50)^2
#####################################
# detrend and calculate fluxes
a1ww_(residuals(lsfit(indx2,ww))/100)
a1ct_residuals(lsfit(indx2,ct))
a1o3p_residuals(lsfit(indx2,o3p))
khf_var(a1ww,a1ct)
o3flux_var (a1ww[1:(N-o3lag)],a1o3p[(o3lag+1):N])
# adjusts the series for o3 lag
a1ww_(c(rep(0,o3lag),a1ww))[1:N]
a1ct_(c(rep(0,o3lag),a1ct))[1:N]
#####################################
# calculate spectral and cospectral components
fww_(fft(a1ww)[2:(N/2)]/N)
fct_(fft(a1ct)[2:(N/2)]/N)
fo3_(fft(a1o3p)[2:(N/2)]/N)
cwt_ ((Re(fww)) * (Re(fct)) + (Im(fww)) * (Im(fct)))
cwo_ ((Re(fww)) * (Re(fo3)) + (Im(fww)) * (Im(fo3)))
cot_ ((Re(fo3)) * (Re(fct)) + (Im(fo3)) * (Im(fct)))
natfreq_freq*(zmeas-dispht)/meanws                    # natural frequency
#####################################
# scatterplot of cospectra
# plot (natfreq,((cwt)*freq*2/(freqint*khf)),log="xy",pch=".",xlab="f = nz/U")
# plot (natfreq,(-(cwo)*freq*2/(freqint*o3flux)),log="xy",pch=".",xlab="f = nz/U")
#####################################
# do not average first five (lowest frequency components)
avercwt[1:5,m]_cwt[1:5]/khf; avercwo[1:5,m]_cwt[1:5]/o3flux
avernatfreq[1:5,m]_natfreq[1:5]
averfreq[1:5,m]_freq[1:5]
j1_6; j2_9
#####################################
# average remaining components in exponential bins
for(i in 1:34)                                        {
        avercwt[5+i,m]_mean(cwt[(trunc(j1)):(min(trunc(j2),9084))])/khf
        avercwo[5+i,m]_mean(cwo[(trunc(j1)):(min(trunc(j2),9084))])/o3flux
        avernatfreq[5+i,m]_mean(c(natfreq[trunc(j1)],natfreq[trunc(j2)]))
        averfreq[5+i,m]_mean(c(freq[trunc(j1)],freq[trunc(j2)]))
        cat(signif(c(avercwt[5+i,m], avercwo[5+i,m], averfreq[5+i], avernatfreq[5+i,m],
        +j1, j2),4),"\n")
        j1_j2
        2_j1+4*((1.2)^(i-1))
        j1_j1+1
                                              }
```

```
#####################################
# individual plots of averaged cospectra
# plot (avernatfreq[,m],((avercwt[,m])*(averfreq[,m])*2/(freqint)),
# +log="xy",pch=7,xlab="f = nz/U",ylab="spectral density (T)")
# plot (avernatfreq[,m],((avercwo[,m])*(averfreq[,m])*2/(freqint)),
# +log="xy",pch=7,xlab="f = nz/U",ylab="spectral density (O3)")
m_m+1
                                                    }
#####################################
# summed individual average plots
par(ask=T)
plot (avernatfreq,(avercwt*(averfreq)*2/(freqint)),log="xy",pch=7,xlab="f = nz/U" ,ylab
+="cospectral density (wT)")
plot (avernatfreq,(avercwo*(averfreq)*2/(freqint)),log="xy",pch=7,xlab="f = nz/U", ylab
+= "cospectral density (wO3)")
#####################################
# average between all runs
avercwt_avercwt*averfreq; avercwo_avercwo*averfreq
totavcwt_numeric(34); totavcwo_numeric(34); totavnatfreq_numeric(34)
# lowest freq component
totavcwt[1]_mean(avercwt[avernatfreq<.001])
totavcwo[1]_mean(avercwo[avernatfreq<.001])
totavnatfreq[1]_mean(avernatfreq[avernatfreq<.001])
cat(signif(c(1,totavcwt[1],totavcwo[1],totavnatfreq[1]),4), "\n")
# rest of components in eight bins per decade
for (p in 1:32)                                     {
        j1_1.3335215^(p-1); j2_1.3335215^(p)
        totavcwt[p+1]_mean(avercwt[avernatfreq>=(j1*.001) & avernatfreq<(j2*.001)])
        totavcwo[p+1]_mean(avercwo[avernatfreq>=(j1*.001) & avernatfreq<(j2*.001)])
        totavnatfreq[p+1] _ mean (avernatfreq[avernatfreq>=(j1*.001) & avernatfreq <
        +(j2*.001)])
        cat (signif(c(j1*.001,j2*.001),3), "\n")
        cat(signif(c((p+1), totavcwt[p+1], totavcwo[p+1], totavnatfreq[p+1]), 4), "\n")
                                                    }
# highest freq component
totavcwt[34]_ mean(avercwt[avernatfreq>10])
totavcwo[34]_ mean(avercwo[avernatfreq>10])
totavnatfreq[34]_ mean(avernatfreq[avernatfreq>10])
cat(signif(c(34,totavcwt[34],totavcwo[34],totavnatfreq[34]),4), "\n")
#####################################
# plot averaged cospectra
plot (totavnatfreq,(totavcwt*2/(freqint)),log="xy",pch=7,xlab="f = nz/U", ylab =
+"cospectral density (wT)")
plot (totavnatfreq,(totavcwo*2/(freqint)),log="xy",pch=7,xlab="f = nz/U", ylab =
+"cospectral density (wO3)")
```

C.4 COFLUX.SP

```
# calculates wo and wt cospectra
# calculates the o3 fluxes based on the heat flux and a ratio of band pass
# covariances.  Uses the same file info program as ANALYSIS8.SP
```

```
# built from SPEC2.SP uses many of the same things
#######################################
gg_9.82;kk_0.4;stabil_0;intercept_0
# loop through files
for (i in (c(3:8,17:21,23:30,32:43,45:52,54:58,60:75,77:80)))          {
fn_cfn[i]
starttime_substring(fn,5,8)
fdate _ as.numeric(fdate)  ;  starttime _ as.numeric(starttime)
aaa_scan(fn, list(0,0,0,0,0))
uu_aaa[[1]]; vv_aaa[[2]]; ww_aaa[[3]]; cc_aaa[[4]]; o3r_aaa[[5]]
meanws2_mean((((uu)/100)^2 + ((vv)/100)^2)^(.5))  # actual mean wind
slope _cslope[fn==cfn]
o3lag _clagwo3[fn==cfn]
fetch _cfetch[fn==cfn]
presr _cpresr[fn==cfn]
RH _c
correcfac _ccorrectionfac[fn==cfn]
if (correcfac<.99){ corfac _1/correcfac}
#######################################
o3p_(intercept+(slope*o3r)*corfac)
ct_(1/403)*(cc/50)^2
N_ length (uu)
indx2_seq(1,N)
a1ww_(residuals(lsfit(indx2,ww))/100)
a1uu_(residuals(lsfit(indx2,uu))/100)
a1vv_(residuals(lsfit(indx2,vv))/100)
a1ct_residuals(lsfit(indx2,ct))
a1o3p_residuals(lsfit(indx2,o3p))
#######################################
# calculate fluxes
ustar_(((var(a1uu,a1ww))^2)+(var(a1vv,a1ww))^2)^0.25
khf_var(a1ww,a1ct)
if ((!is.na(o3p[1]))) o3flux_var (a1ww[1:(N-o3lag)],a1o3p[(o3lag+1):N]) else o3flux_NA
#adjusts the series for o3 lag
a1ww_(c(rep(0,o3lag),a1ww))[1:N]
a1ct_(c(rep(0,o3lag),a1ct))[1:N]
rho_presr*100/(287*meant)
meant_mean (ct)
L_(-1.0)*(meant*ustar^3)/(kk*gg*khf)
MOP_(zmeas-dispht)/L
indx_(seq(1,(N/2-1)))
freq_10.5*(1:(N/2))/N                          # frequencies
#######################################
# calculate spectral and cospectral components
fww_(fft(a1ww)[2:(N/2)]/N)
fct_(fft(a1ct)[2:(N/2)]/N)
fo3_(fft(a1o3p)[2:(N/2)]/N)
cwt_ ((Re(fww)) * (Re(fct)) + (Im(fww)) * (Im(fct)))
cwo_ ((Re(fww)) * (Re(fo3)) + (Im(fww)) * (Im(fo3)))
cot_ ((Re(fo3)) * (Re(fct)) + (Im(fo3)) * (Im(fct)))
# define frequency cutoffs
freqs_c(5,2,1,.5,.2,.1,1/30,1/60,1/120,1/300)
cfreqs_round ((freqs*N/10.5),0)
for (j in 1:10)      {
```

```
        if (cfreqs[j]>spike) cfreqs[j]_cfreqs[j]-(2*wid + 2)
        # bandpass covariances
        bpcwt_2*sum(cwt[1:cfreqs[j]])
        bpcwo_2*sum(cwo[1:cfreqs[j]])
        # cospectral flux estimate
        esto3flux_khf*bpcwo/bpcwt
        fluxerr_abs((o3flux-esto3flux)/o3flux)*100
        cat (fdate, starttime, signif(c(meanws2, ustar, khf, o3flux, fetch, MOP, freqs[j],
        +bpcwt, bpcwo, esto3flux,fluxerr),4),"\n")
                                        }
                                        }
sink()
```

APPENDIX D : STATIONARITY AND FETCH REQUIREMENTS

D.1 Stationarity test

Time series from the rapid response measurements of w, T and O_3 were tested for nonstationarity of the variance using the non-parametric run test described in Bendat and Piersol (1986) and in Chapter 2.7.

Each half hour time series was subdivided into 20 blocks. The data in the respective blocks may be regarded as independent. Variance was calculated for each block and compared to the median variance for all blocks. The number of runs of one or more subdivision with greater or lesser variance was counted. The hypothesis of stationarity was accepted at the 95% level if there were 6 or more runs within the 20 subdivisions. If there were less runs, that time series was judged to have a significant nonstationarity of the variance.

Thirteen of the seventy-two sampling periods had nonstationarities in one or more of the series. Temperature variance was most frequently nonstationary. Nonstationarities in the temperature signal were associated with scattered clouds on the 14th and 31st of August and with evening cooling on the 11th. One period had non-stationary ozone variance, and two had non-stationary vertical velocity variance.

Twelve nonstationary samples were included in the final analysis as they showed no systematic differences from other samples. One was rejected as it also had poor fetch.

Nonstationarity of the mean was also present in many of the time series. This was largely dealt with by removing the linear, least squares trend from each variable, in each sampling period.

Table D.1: Results of the run test for stationarity of variance. Sampling periods with one or more nonstationary variables are flagged with arrows.

Date	Time	Number of Runs				Date	Time	Number of Runs		
		w	T	O_3				w	T	O_3
10	1625	13	10	10		27	1446	12	12	8
10	1657	14	12	14		27	1515	8	17	11
11	1522	8	11	14		27	1545	13	10	7
11	1558	14	9	8		27	1616	10	7	9
11	1629	13	8	14		27	1645	8	11	5
11	1745	7	4	11	<<	27	1715	6	6	9
11	1817	11	14	12		27	1745	11	7	8
11	1848	12	4	11	<< >>	27	1815	4	4	15
12	1641	6	10	12		27	1846	9	11	8
12	1712	10	10	8		27	1902	10	13	7
12	1743	9	10	8		27	1934	10	6	7
12	1813	15	6	9		30	1151	6	14	11
13	1234	7	8	11		30	1221	14	12	9
13	1315	11	10	14		30	1301	13	13	11
13	1348	9	11	16		30	1332	14	10	10
13	1420	12	13	12		30	1408	9	10	10
13	1451	13	15	11		30	1449	12	6	10
13	1521	14	11	9		30	1519	11	10	8
13	1553	10	5	8	<<	30	1550	11	9	10
13	1624	7	9	9		30	1620	8	12	12
13	1655	9	12	12		30	1651	12	9	12
13	1726	10	7	10		30	1721	8	8	12
13	1759	6	8	11		30	1751	8	6	14
14	1120	7	9	14		30	1821	11	9	11
14	1150	14	11	10	>>	30	1853	6	13	3
14	1222	10	8	10	>>	30	1923	5	10	7
14	1253	9	8	14		30	1953	7	11	12
14	1325	9	8	10		31	1150	8	10	11
14	1357	8	13	11		31	1220	14	8	7
14	1427	8	5	8	<<	31	1250	10	8	11
14	1459	14	11	13		31	1320	13	11	14
14	1530	11	2	10	<< >>	31	1350	9	4	8
14	1600	10	2	9	<< >>	31	1351	12	3	8
14	1630	12	5	10	<<	31	1421	13	10	10
27	1259	11	10	9		31	1453	8	6	9
27	1424	10	10	11	>>	31	1523	6	4	12

D.2 Fetch

Each sampling period was screened for fetch direction to ensure that the requirement for upwind homogeneity was met. Wind direction measurements from the Met-One wind vane were used to classify the fetch for each sampling period. Given the location of the measurement site (Figures 2.1, 2.2) near the northeast corner of a field, winds from the southwest quadrant were required for adequate upwind fetch.

Wind directions from 195° through 280° were considered good fetch directions. Wind directions from 175° to 195° and from 280° to 300° were considered acceptable fetch directions. Other wind directions were considered to provide poor fetch.

Three samples; August 27, 1616, and August 30, 1923 and 1953, were rejected from further analysis because of poor fetch direction. Of the remaining 69 samples, the large majority had good fetch direction.

APPENDIX E : TRANSFER FUNCTIONS OF THREE FILTER TYPES

Figure E.1 shows the frequency response of three filter types, all with a nominal cut-off frequency of $\pi/10$. The 'ideal' cutoff filter has the advantage of simplicity and ease of application. However, its impulse response has lobes corresponding to the sharp edges of the filter.

The 40-term approximation to the ideal filter is described in Voogt (1989). It has a superior impulse response, but is somewhat slower to apply. In the filter test described in Chapter 4.2 there was found to be very little difference between the performance of the ideal filter and the 40 term approximation.

Time domain averaging allows a great deal of leakage from higher frequencies, which may account for the differences in performance between this filter and the other two. Straightforward time domain averaging is useful for smoothing data, but is not the best filter type to use when frequency characteristics are important.

Figure E.1: Transfer functions of three filter types used in Chapter 4.

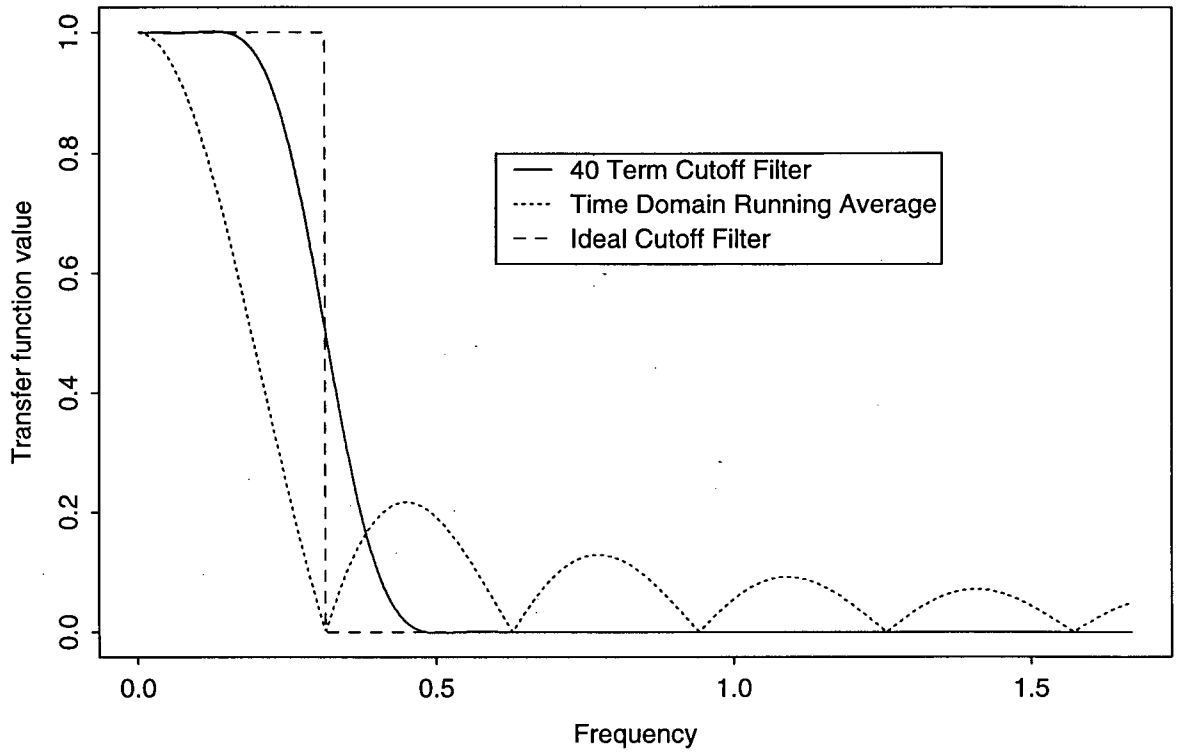

APPENDIX F : EDDY CORRELATION SAMPLING PERIODS

Table F.1: List of sampling periods - start time and duration.

Date	Time (PDT)	Duration (minutes)		Date	Time (PDT)	Duration (minutes)
10	1625	30		27	1424	17
10	1657	30		27	1446	29
11	1522	31		27	1515	29
11	1558	30		27	1545	29
11	1629	7		27	1645	30
11	1745	30		27	1715	29
11	1817	30		27	1745	29
11	1848	30		27	1815	29
12	1641	29		27	1846	15
12	1712	30		27	1902	30
12	1743	30		27	1934	30
12	1813	30		30	1151	30
13	1234	30		30	1221	30
13	1315	23		30	1301	30
13	1348	30		30	1332	20
13	1420	30		30	1408	32
13	1451	30		30	1449	30
13	1521	30		30	1519	30
13	1553	29		30	1550	30
13	1624	30		30	1620	30
13	1655	31		30	1651	30
13	1726	31		30	1721	30
13	1759	20		30	1751	30
14	1120	30		30	1821	30
14	1150	32		30	1853	30
14	1222	30		31	1150	30
14	1253	31		31	1220	30
14	1325	30		31	1250	30
14	1357	30		31	1320	30
14	1427	31		31	1350	9
14	1459	30		31	1351	30
14	1530	30		31	1421	30
14	1600	29		31	1453	30
14	1630	31		31	1523	30
27	1259	30				